Radiative heat transfer and thermal management in nano-scale

Jiebin Peng

A THESIS SUBMITTED FOR THE DEGREE OF

DOCTOR OF PHILOSOPHY IN SCIENCE

DEPARTMENT OF PHYSICS

SUPERVISORS: Prof. Wang Jian-sheng & Dr. Zhang Gang

EXAMINER: Prof. Gong Jiangbin

NATIONAL UNIVERSITY OF SINGAPORE

2017

Declaration

I hereby declare that this thesis is my original work and it has been written by me in its entirety. I have duly acknowledged all the sources of information which have been used in the thesis. This thesis has also not been submitted for any degree in any university previously.

Jiebin Peng

20 Nov. 2017

Dedicated to my family

Acknowledgements

At first, I would like to thank my supervisor, Prof Jian-sheng Wang. During my four years of Ph.D. life, he gave me with guidance, inspirations, and assistances. He also shared with his personal research experiences, taught rigorous ways to make a difference in the research area. During the early stage, his insightful suggestions placed the paths to the exciting projects. In the later stages, his emphasis on independent research has successfully produced a young research mind. It is a great honor and blessing to be his student. His knowledge, wisdom, and kindness have always been and will always be what I look up to.

Next, I would like to thank my co-supervisor, Dr Gang Zhang and Prof. Baowen Li. We collaborated for the past years, during which I picked up useful skills. I would like to express my deepest gratitude to them for their guidance.

I also would like to thank my collaborator, Han Hoe Yap. He is an energetic and smart student. I also learned a lot from him. I would like to express my heartfelt appreciation for his help.

Last but not least, I would like to thank my family and friends for their continuous support and encouragement throughout my Ph.D. study.

Contents

Summary

The investigation of radiative heat transfer (RHT), in nanoscale, has been an increasingly important area in both theoretical and experimental physics recently. With the decreasing of gap separation, radiative heat transfer between different bodies becomes complicated due to the quantum nature of the systems. In this thesis, we first focus on the applications of fluctuation electrodynamics (FE) to the investigation of radiative heat transfer between different 2-d materials. Fortunately, the near-field radiative heat transfer (NFRHT) between different 2-d materials can enhance the heat dissipation, even several times larger than the heat dissipation through conduction. Hence, the RHT can provide a new designing strategy for thermal management between different 2-d materials.

However, the question is till raised: how the quantum effects influence the RHT between small quantum systems. In the next part, we focus on contribution of the scalar-field photon for the RHT using non-equilibrium Green's functions (NEGF). With this pure quantum field approach, a $1/d^2$ distance dependence in large distance separation is found due to quantum capacitor physics. We also recover the FE results under the local equilibrium approximation when we change the reflection coefficients as the self-energy of the quantum system. Besides, when the system is located at the real nonequilibrium steady state, under self-consistent Born approximation, the RHT between different bodies will have different behaviours due to the contribution of strong field-system interaction.

Thanks to the interesting properties of capacitor physics, in the last part of this thesis, we focus on the construction of quantum thermal rectifiers and thermal transistors. Due to the different system-bath coupling, the double quantum dots model can exhibit very large rectification effects. In particular, it is shown that the rectification ratio can be tuned through the changing of chemical potential of heat bath, which could be of potential technological interest to build thermal radiative diodes. Then with the help of non-linear thermal bath, a quantum radiative thermal transistor is constructed through four quantum dots. We numerically demonstrate that thermal switch, thermal modulation and thermal amplification can be achieved. Our approach can open the door for the RHT applications through quantum controlling.

List of Publications

Jiebin Peng, Gang Zhang, Baowen Li, *Thermal management in MoS_2 based integrated device using near-field radiation*, App. Phys. Lett **13**, 107 (2015)

Jian-Sheng Wang, Jiebin Peng, *Capacitor physics in ultra-near-field heat transfer*, Eur. Phys. Lett. **118**, 24001 (2017)

Jiebin Peng, Han Hoe Yap, Gang Zhang, Jian-Sheng Wang, *A scalar photon theory for near-field radiative heat transfer*, (submitted)

Jiebin Peng, Gang Zhang, Jian-Sheng Wang, *Radiative quantum thermal transistor*, (in preparation)

List of Figures

Abbreviations

RHT	radiative heat transfer
FE	fluctuation electrodynamics
NFRHT	near-field radiative heat transfer
NEGF	non-equilibrium Green's function
GF	Green's functions
FDT	fluctuation-dissipation theorems
SPhPs	surface phonon polaritons
SPPs	surface plasmon-polaritons
STM	scanning tunneling microscope
AFM	atomic force microscope
GaN	gallium nitride
TMD	transition metal dichalcogenide
TSS	two-state system
DQW	double quantum well
TIM	thermal interface materials
TE	transverse electric
TM	transverse magnetic

Chapter 1

Introduction

"Learn from yesterday, live for today, hope for tomorrow.
The important thing is not stop questioning."

—Albert Einstein

In nature, there are three kinds of ways of heat transfer: conduction, convection, and radiation. Different from conduction and convection, the RHT is produced by the fluctuating electromagnetic field and existed in all objects at non-zero temperature. Based on the famous Planck's Black-body theory, which paves the way for quantum physics at the beginning of the twentieth century, the RHT between two bodies is limited by the Stefan-Boltzmann law in the far-field region, and we call this limit as "black-body limit"[1]. However, in the last several decades, both theories and experiments found that in the near-field region, where the gap between two bodies is smaller than the thermal wavelength, the heat can transfer through the evanescent modes[2–7]. In that near-field region, the RHT can be several orders larger than the value from Black-body limit calculation, and we name such near-field enhancement for heat transfer as NFRHT. Due to the no-contacting properties and the vast improvement of RHT through the NFRHT, there are broad applications for the NFRHT in different research areas, such as thermal management, thermal circuits and thermophotovoltaic[8].

At first, we focus on the roles of NFRHT among the various 2-d materials and provide theoretical support for designing strategy for thermal management through NFRHT. In

spite of broad applications of NFRHT, there is one still unsolved fundamental problem: the role of the RHT when the distance is extremely smaller than the thermal wavelength. Different from NFRHT, in the extreme near-field or ultra-near-field region, the nonlocal quantum effects play important roles, and the thermal equilibrium is hard to reach due to the strong interaction between different bodies. However, previous studies have always primarily concentrated on Rytov's fluctuation electrodynamics, which is a semi-classical approach. In the extreme near-field region and small quantum system, such method could be broken down due to its local equilibrium assumption. Recently, two experiments results show two different conclusions and the experimental data are rather controversial[7, 9, 10]. To the best of our knowledge, there is no general agreement on extreme near-field RHT. To obtain the quantum effects in RHT calculation, the NEGF, one of the useful tools for the quantum thermal transport calculation to electron and phonon, is used to calculate RHT between two bodies with minimal distance. Based on NEGF, we propose a microscopic approach for ultra-near-field radiative heat transfer. Our approach can be collaborated with first principle calculations and open the way for more rigorous predictions of RHT in the ultra-near-field region. Besides, thanks to the quantum effects of the RHT in the ultra-near-field region, the series of quantum radiative devices can be designed, such as the quantum radiative thermal rectifier[11, 12], thermal transistor[13, 14], thermal memory[15] and so on.

1.1 Radiative heat transfer

RHT is not only a fundamental question in thermal physics but also a significant challenge in thermal technology development from thermal management to energy conversion[16]. In this section, we give a brief review of the history of the RHT both theoretical and experimental developments. The very recent experimental developments of the RHT and unsolved questions in this research area are also discussed and listed.

Historically, the discussion of the RHT began by the discovery of the infrared in 1800, which is the primary energy carrier of the RHT[17–19]. The well-known Maxwell equations propose that the nature of radiation is one kind of electromagnetic phenomena.

When the radiation met the heat in the 20th century, Planck's thermodynamic treatment for the blackbody radiation played a significant role in the construction of advanced theory for thermal radiation and also opened the door for quantum physics[1]. Based on Planck's Blackbody theory, the RHT between two bodies is limited by the Stefan-Boltzmann law. This law gives the maximum RHT between two bodies in the far field region.

$$S = \frac{\pi^2 k_B^4}{60\hbar^3 c^2}(T_1^4 - T_2^4) \tag{1.1}$$

where S is the energy current density per surface area, T_1 and T_2 are the temperature of different bodies. In Planck's blackbody theory, the RHT has a very broadband emission spectrum, and it implies temporal incoherence. Besides, Wien's displacement law gives temperature dependent peak position of the blackbody emissive spectral. The above Stefan-Boltzmann law and Wien's displacement law are directly derived from Planck's blackbody theory, and they build the foundation for the theory of RHT in the far field region. However, the Planck's theory is not valid when the separation is comparable or smaller than the thermal wavelength. Until several fluctuation-dissipation theorems (FDT)[20–23] in the quantum region was investigated, in the 1950s, Sergei M. Rytov provided fluctuation electrodynamics to describe the relation between the thermal radiation and the fluctuation current by combining the Maxwell equation and the Langevin equation to investigate Casimir force[24, 25]. However, this important theory did not attract much researchers' attention at that time until the requirement arose to control RHT between two bodies with a distance similar to or shorter than the thermal wavelength. In 1961, A. G. Emslie showed that the RHT between metal foils could be increased with reduced distance between two bodies as a result of interference effects of propagating waves[26]. After that, researchers began to pay more attention to the RHT with small separation due to the needs and progresses in both theories and experiments. In 1970, Boehm and Tien demonstrated the RHT between two metals through the transparent dielectrics can be several orders larger than the far-field RHT[27]. In the following year 1971, Polder and Van Hove proposed their well-known theory of the

RHT between two closed bodies based on Rytov's fluctuation electrodynamics[28]. Using the isotropic, nonmagnetic and local equilibrium assumption, they put forward the semi-analytical formula for the RHT between two semi-infinity planes. In 1980, Levin and Rytov calculated the RHT between two conductor surfaces by the generalized Kirchhoff law when the normal and the anomalous skin effects were dominated[25]. In 1999, Pendry illustrated a brief derivation for the NFRHT between two semi-infinite planes due to evanescent waves and also calculated the NFRHT between metal particle and metal plane[29]. In the last decade, the non-local quantum effects were also obtained by the fluctuation electrodynamics[30]. The detailed information for the fluctuation electrodynamics will be presented in Chapter 2.

Different with the development of theoretical studies, experimental studies are limited by the developments of nanoscale measurements. Here, we first review the development of the experimental measurement for NFRHT with parallel plates configurations. In the previous theoretical studies, people always focused on the parallel plate configuration, and the near-field enhancement only occurs in the nano-scale gap. Such parallel plates configuration with the nanoscale gap is very hard to achieve in the experiments. In an AIAA conference, Cravalho, Domoto, and Tien first report the RHT measurements between two copper plates in very low-temperature region i.e. 4.2 K. In that experiment, the gap separation between two plates was changed from 2 mm to 10 μm and their experimental data showed that there is gap separation dependence of the RHT[27]. Later, Kutateladze, Rubtsov, and Baltsevich reported the similar experimental results where the separation between two copper disk was changed from 10 μm to 250 μm with a set of temperature differences. Their results verified the distance dependence of NFRHT and the threshold gap size is almost three times of thermal wavelength which is estimated by Wien's displacement law[31]. In 1969, Hargreaves took the first plate-plate experiment in room temperature region and this preliminary results indicated that there is also apparently distance dependence of the NFRHT in the room temperature[32]. After that, there are no new experiments for parallel plates configuration in the early 2000s. With the developments of micro- and nanotechnology, in 2008, Hu et al. measured the

NFRHT between parallel glass optical flats where the surface phonon polaritons (SPhPs) is excited in the mid-infrared frequency region[33]. They found that such SPhPs modes can enhance the NFRHT and such enhancements for NFRHT is much larger than the NFRHT between two parallel metal plates. However, Hu's experiment can not measure the gap size effects of NFRHT. Subsequently, two groups investigated the NFRHT with changed gap sizes[34, 35]. In their experiments, the magnitude of heat flux can be enhanced about three or four orders when the gap sizes are changed from large value to small value. Remarkably, their data agree well with the theoretical calculation in the large gap size region, but in the smallest gap size region, the measurements are lower than the theoretical prediction. Recently, several experiments focused on more accurate and convenient measurements for NFRHT in the hundreds of nanometer gap range.

As shown in above two paragraphs, the NFRHT measurements of parallel-plane configuration have very long history. In the meantime, some ingenious instruments and achievements were created and discovered. In that paragraph, we review the development of the experimental measurement for NFRHT with tip-plate configurations, which is beneficial for the better understanding of NFRHT with the nanometer gap separation. Different with the parallel plates configuration, the tip-plate configuration can be achieved easily in experiments. In the early 1980s, the creation of the scanning tunneling microscope (STM) and atomic force microscope (AFM) make it possible to measure the NFRHT between sharp tip and plate[36]. In the 1990s, several groups took the measurement of NFRHT with tip-plate configuration. But due to the uncertainty of experimental setup, these experimental results do not obtain a quantitative comparison with the theoretical prediction[37, 38]. In 2005, NFRHT between a scanning thermal microscope probe tip and planar surfaces of Au and gallium nitride (GaN) was studied with very small gap separation i.e. 1 nm to 200 nm[39]. Comparing with their theoretical dipole calculation, the authors proposed that the nonlocal effects become important for NFRHT when the gap distance is extremely small. After that, a set of experiments were focused on the measurement of NFRHT with different tip and plate materials in very small distance separation. In 2015, Kim K et al. use custom-

fabricated scanning probes and their new measuring tools to measure RHT down to gaps as small as two nanometers[40]. And they presented that the theoretical calculation based on fluctuation electrodynamics keeps an excellent agreement with their experimental results. However, in 2017, Konstantin K et al. demonstrated that the quantitative measurements of NFRHT between a gold-coated thermal microscope tip and a gold plate with nanometer gap separation are more than five orders of magnitude larger than Blackbody limit and four orders of magnitude larger than the fluctuation electrodynamics based calculation[9]. One remarkable difference between Kim's and Konstantin's measurement is that tip used in Konstantin's experiment is much smaller than Kim's experiments.

Different with nanoscale thermal conduction, nanoscale RHT provides new unique opportunities for the controlling of heat flow. With the development of theory, computational tools and nanoscale measurements for NFRHT, many predictions of nanoscale RHT are achieved by various groups. For future applications in thermal management and thermal circuits, the NFRHT can play important roles. As we shown in previous paragraphs, the challenges for the measurements of NFRHT in the extremely near-field region with parallel plate configuration still exists. The differences between Kim and Konstantin's results demonstrate that we need to go beyond the fluctuation electrodynamics theoretically.

1.2 Nonequilibrium Green's function

NEGF are the main component of quantum statistical mechanics and quantum kinetic equations[41]. To stimulate the system far from equilibrium, NEGF in real time is extended from the Matsubara's method of quantum many-body theory with nonzero temperature[42]. In general, the success of NEGF is because the foundation of equilibrium Green's functions theory, i.e. Feynman diagram expansion techniques, can be applied without major conceptual modifications to nonequilibrium systems.

Historically, the NEGF began at Schwinger's study for the Brownian motion of a quantum oscillator[43]. Then people realized that the forward and backward evolution

plays an important role in the calculation of nonequilibrium quantum expectation values at time t and defined the six different Green's functions. With the help of contour order, Keldysh indicated that Ferman diagrammatic expansion is still working for nonequilibrium steady states[44]. After that, Caroli et al. gave a formula for the transmission coefficient regarding the Green's functions at the first time[45]. Generally, the nonequilibrium Green's functions method can apply to arbitrary time evolutions of correlated systems and does not need any other statistical assumptions. When the system is located at the nonequilibrium steady states, the external driving force keeps balance with the heat bath dissipation. At that time, the Green's functions do not change with average-time and the boundary condition due to the heat bath can determine the actual Green's function(boundary-matching problem). In this case, the formulation for NEGF can be greatly simplified. Our NEGF calculations in this thesis are based on this important non-equilibrium steady state assumption. In the method part of this thesis, we will briefly review the Kadanoff-Baym formalism[46] in contour order and then discuss the Keldysh formalism for the nonequilibrium steady states in Keldysh contour order[44].

1.3 Thermal management in nanoscale

Typically, RHT is not an advantageous access for thermal management because the Stefan-Boltzmann law confines the maximum magnitude of radiative heat flux. Due to the substantial enhancement ,i.e., orders of magnitude exceeding the Black-body limitation, NFRHT provides a reasonable way for the radiative heat controlling in the nanoscale. Different with the historical studies of nanoscale thermal transport with phonon transport, the ability to modulate heat flux with NFRHT has promising uses in thermal management and thermal circuits[47].

Recently, some investigations have illustrated several ways to efficiently modulate the NFRHT between two bodies with nanometer vacuum separation. An optional method of thermal modulation can be accomplished by changing the relative movement between different systems[48–50]. The reason is that the relative movement can adjust the reflection coefficient due to a Doppler effect. Another straightforward way to modulate

the NFRHT is by changing the optical conductivity of materials because the reflection coefficient is strongly dependent on it[51]. Furthermore, systems with the remarkable nonlinear temperature dependence of the optical conductivity have numerous possible to control NFRHT. Also, the voltages could be applied to tune RHT between graphene and silica due to the voltage dependence of optical properties[52].

One possible application with high modulation of NFRHT is to create radiative thermal diodes or vacuum thermal rectifiers[53], which can control the heat flux in a preferred path as similar as electrical diodes. Phase-change materials, for example, VO_2, have been used to obtain substantial thermal rectification effect[54]. Besides, near-field thermal rectifiers through vacuum based on the thin films have also been well studied.

Except for the thermal rectifiers, NFRHT can be operated to build a radiative thermal transistor[13], which is the primary segment for thermal circuits and thermal computing. Similar to the electric transistor, a radiative thermal transistor is also made up of three components: a hot "source", a cold "drain", and a controllable "gate". The heat current between the source and the gate and that between the gate and the drain can be adjusted through modifying the gate temperature with a tiny gate heat current. Ben-Abdallah and Biehs showed a near-field thermal transistor design relied on a phase change of the VO_2 gate and the thermal switching, modulation, and amplification can be reached[13]. In 2016, Karl Joulain et.al presented a thermal transistor which is made with three two-level quantum subsystems coupled to a thermal bath[14].

Photon-based modulation of heat with nanoscale separation displays differences and benefits comparing with phonon transport, for instance, high transportation speed due to the intrinsic differences between phonon and photon. By modulating heat with the velocity of light, photon-based thermal devices could be perhaps better than the phononic devices[55] and even electrical devices, which perhaps can strongly motivate the developments of information processing and computing.

1.4 The arrangement and purposes of thesis

The arrangement of research topics is presented in the below thesis structure chart as shown in Fig. (1.1). The central focus of our research interests is RHT in nanoscale (phenomena). The final goal is finding and designing a new device for radiative thermal management and thermal circuits (application). FE is one of the powerful tools for semiclassical RHT calculation. The NEGF method for RHT can extend our insight into the quantum region. With the help of such two methods, a more interesting picture can be drawn for this research area.

In the first part of this thesis (Introduction part), we historically introduce the central objects, including the development of RHT, NEGF, thermal management and thermal circuits in nanoscale. The figure of thesis arrangement is also shown to provide a straightforward picture for the dissertation structure.

In the method part of this thesis (Chapter 2), we brief view the standard FE for RHT calculation. A longitudinal wave method for RHT is also presented to keep self-consistence with FE formalism and make a rigorous mathematical foundation for the NEGF formalism for the scalar-field photon in Chapter 4. In the last part of the method Chapter, a brief review for NEGF is also given.

In Chapter 3, we apply the advantages of NFRHT and provide a radiative cooling strategy for the MoS_2 based devices with the help of FE formalism. From previous research investigations, it is well known that the NFRHT can enhance the heat flux with orders of magnitude exceeding the Black-body limitation. However for MoS_2 based ICs, one of potential useful 2-d material, due to the larger number of transistors or higher functional density, heat dissipation will become a crucial issue. Using the formalism of fluctuation electrodynamics, we explored the NFRHT from a monolayer MoS_2 to graphene. We demonstrate that in resonance, the maximum heat transfer via near-field radiation between MoS_2 and graphene can be ten times higher than the in-plane lattice thermal conduction for MoS_2 sheet. Our work sheds light for developing a new cooling strategy for nanodevices constructing with low thermal conductivity materials.

However, in the extreme near-field or ultra-near-field region, the RHT between two

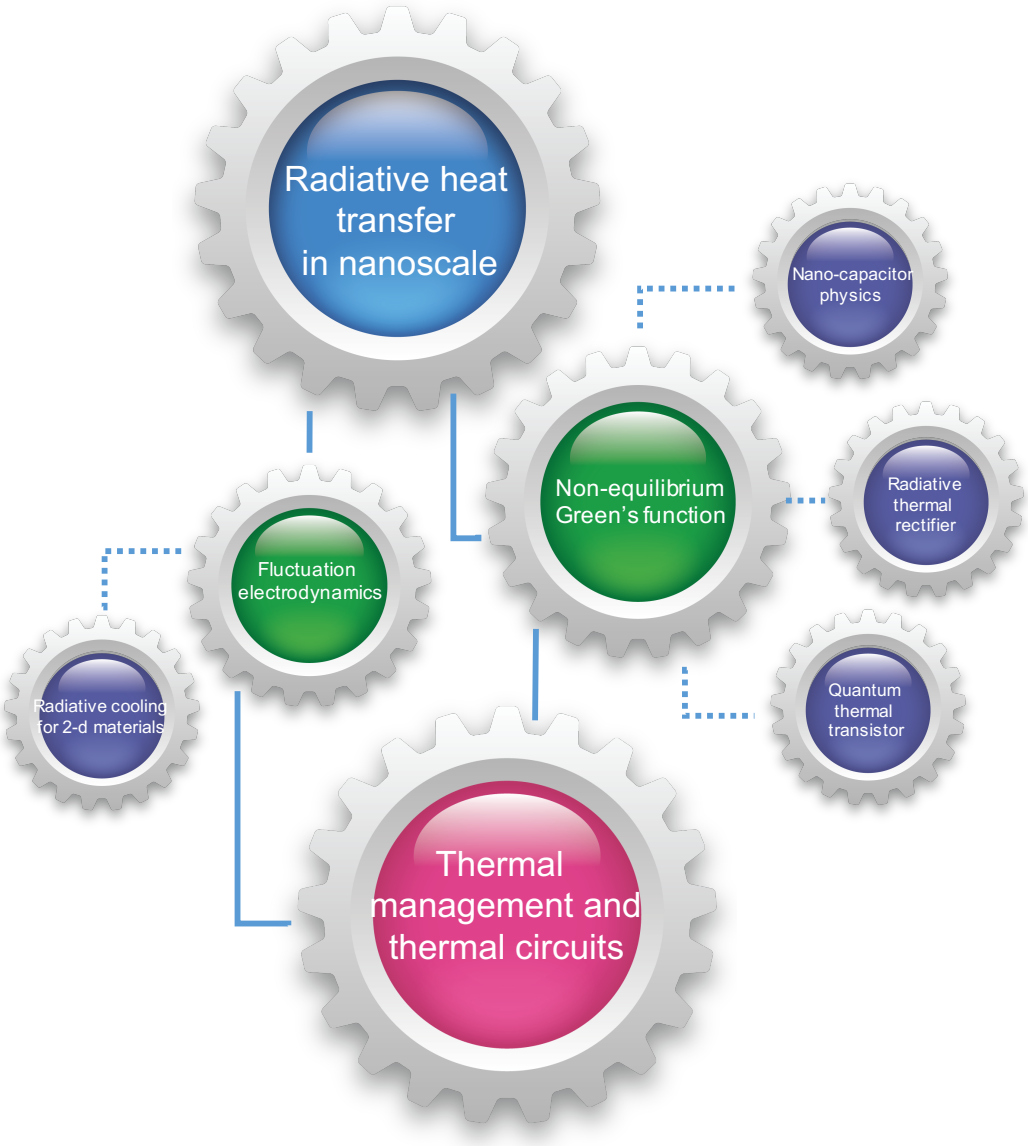

Fig. 1.1: The flowchart of the thesis arrangement

objects will become very complicated due to the contribution of different quantum effects. In Chapter 4, using the NEGF formalism, we propose a microscopic theory for NFRHT between charged metal plates focusing on the Coulomb interactions. Tight-binding models for the electrons are coupled to the electric field continuum through a scalar potential. For a two quantum-dot model a new length scale emerges below which the heat current exhibits great enhancement. This length scale is related to the physics of parallel plate capacitors. At long distances d, the energy flux decreases as $1/d^2$.

Chapter 5 shows the application for thermal management and thermal circuits based on the capacitor physics in the previous Chapter. Using the NEGF formalism, a quantum radiative thermal rectifier and thermal transistor are designed through several quantum dots and non-linear thermal baths. Our calculation can pave the way for the development of radiative thermal management and thermal circuits in quantum region.

Finally, in Chapter 6, we provide the conclusion of this thesis and discuss the future work.

THIS PAGE IS INTENTIONALLY LEFT BLANK

Chapter 2

Methods for radiative heat transfer

"Brevity is the soul of wit."

—William Shakespeare

2.1 Fluctuation electrodynamics

2.1.1 Brief review

The key picture for recent studies of thermal radiation is the fluctuating thermal currents and electromagnetic fields. Based on the FDT of Callen and Welton[20], the correlation between random electrical currents, which is produced by thermal fluctuation, is immediately connected to the dielectric constant of a medium. Once we determine the macroscopic Maxwell's equations with the random sources and match the boundary condition carefully, the ensemble-average of Poynting vector gives the radiative heat flux. The basic formalism of this process is called the fluctuation electrodynamics[24, 25]. A key assumption of fluctuation electrodynamics is that the fluctuating electrical currents only dependent on the temperature of the medium and the effects of interaction between medium and electromagnetic field are ignored.

The story of FE can go back to the undergraduate classes: Solid state physics, the theoretical development of van der Waals force. At early 1930, London realized the quantum fluctuation of electric dipole moments could produce a force between two objects with a macroscopic distance separation[56]. He showed that the force between

two neutral atoms separated by distance d is varied with d^{-7} with no retardation effects. And this conclusion is only valid when separation of two atoms is much smaller than the wavelength corresponding to a transition of atoms between the ground state and excited state. In 1948, Casimir and Polder showed that the force between two bodies is varied with d^{-8} if considering the retardation effects for long distance[57]. This is the well known Casimir's force and he thought this force comes from the variation of zero-point energy of electron magnetic field with distance changes. In 1954, Lifshitz derived the attraction between two bodies using a classical way: the fluctuation of electromagnetic field developed by Rytov[58]. It is a classical way and did not consider the non-local effect, such as anomalous skin effect. The whole process of FE in RHT calculation is similar with the derivation of Lifshitz for van der Waals forces, i.e. we focus on the calculation of Poynting vector instead of Maxwell stress tensor.

In the first section of this Chapter, we will provide a summary for the development of fluctuation electrodynamics with detailed formula.

2.1.2 Classical Green's functions description

The Green function (GF) formalism, which is one of the analytical methods, has distinct benefits and constraints. It has been used almost only for highly symmetric configurations, such as infinite planes, dipoles, spheres, and cylinders. Once applying to real calculation, the GF can give the semi-analytical or even exact solutions with several assumptions. A brief outline of this method is given below.

Assumptions

The derivation of fluctuation electrodynamics shown as below is based on some assumptions:

a. Continuum electromagnetic treatment (macroscopic Maxwell's equations);

b. Zero correlation radius for electric currents (locality);

c. Isotropic nonmagnetic properties of material;

d. Stationary in time with local thermodynamic equilibrium.

Maxwell's equation

The physical picture of fluctuation electrodynamics starts from macroscopic description with thermal fluctuating micro-electron currents which constitute as the random source[28, 59, 60].

$$\begin{aligned} \nabla \times \boldsymbol{E} &= -\frac{\partial \boldsymbol{B}}{\partial t} \\ \nabla \times \boldsymbol{H} &= \frac{\partial \boldsymbol{E}}{\partial t} + \boldsymbol{j}_{ind} + \boldsymbol{j}_{source} \end{aligned} \tag{2.1}$$

Where $\boldsymbol{j}_{source}$ is the thermal random current density source and $\boldsymbol{j}_{ind}$ is the induced current density in the presence of the EM field. If the material is isotropic and nonmagnetic, the local relation between $\boldsymbol{j}_{ind}(\boldsymbol{x}, t)$ and $\boldsymbol{E}(\boldsymbol{x}, t)$ can be written in each frequency component.

$$\frac{\partial \boldsymbol{E}(\boldsymbol{x}, \omega)}{\partial t} + \boldsymbol{j}_{ind}(\boldsymbol{x}, \omega) = i\omega\epsilon(\omega)\epsilon_0 \boldsymbol{E}(\boldsymbol{x}, \omega) = i\omega \boldsymbol{D}(\boldsymbol{x}, \omega) \tag{2.2}$$

Where $\boldsymbol{x}$ is the position vector. $\epsilon(\omega) = \epsilon'(\omega) + i\epsilon''(\omega)$ and the imaginary part of $\epsilon(\omega)$ contains the dissipative properties of the material. $\boldsymbol{D}(\boldsymbol{x}, \omega)$ is the electric displacement.

In frequency domain, Eq. (2.1) can be rewritten as below:

$$\begin{aligned} \nabla \times \boldsymbol{E}(\boldsymbol{x}, \omega) &= i\omega \boldsymbol{B}(\boldsymbol{x}, \omega) \\ \nabla \times \boldsymbol{H}(\boldsymbol{x}, \omega) &= -i\omega \boldsymbol{D}(\boldsymbol{x}, \omega) + \boldsymbol{j}_{source}(\boldsymbol{x}, \omega) \end{aligned} \tag{2.3}$$

Based on Eq. (2.3), the vector Helmholtz equations for the electromagnetic waves ($\boldsymbol{E}$, $\boldsymbol{H}$) can be derived as below:

$$\begin{aligned} \nabla \times \nabla \times \boldsymbol{E}(\boldsymbol{x}, \omega) - \epsilon(\omega) \left(\frac{\omega}{c}\right)^2 \boldsymbol{E}(\boldsymbol{x}, \omega) &= i\omega\mu_0 \boldsymbol{j}_{source}(\boldsymbol{x}, \omega) \\ \nabla \times \nabla \times \boldsymbol{H}(\boldsymbol{x}, \omega) - \epsilon(\omega) \left(\frac{\omega}{c}\right)^2 \boldsymbol{H}(\boldsymbol{x}, \omega) &= \nabla \times \boldsymbol{j}_{source}(\boldsymbol{x}, \omega) \end{aligned} \tag{2.4}$$

Fluctuation-dissipation theorem (FDT)

The thermal random current density source $\boldsymbol{j}_{source}$ satisfy the statistical correlation function which is given by the fluctuation-dissipation theorem[22]:

$$\langle \boldsymbol{j}_a(\boldsymbol{x},\omega)\boldsymbol{j}_b^*(\boldsymbol{x}',\omega')\rangle = \frac{4}{\pi}\epsilon''(\omega)\hbar\omega^2\left[\frac{1}{e^{\hbar\omega/kT}-1}+\frac{1}{2}\right]\delta(\omega-\omega')\delta(\boldsymbol{x}-\boldsymbol{x}')\delta_{ab} \tag{2.5}$$

Where the superscript $*$ is the complex conjugate. Factor 4 means that we only retain the positive frequency. $\hbar$ is the reduced Planck constant and T is the absolute temperature. $\frac{1}{2}$ is the zero point contribution of harmonic oscillator. δ_{ab} and $\delta(\boldsymbol{x}-\boldsymbol{x'})$ is the consequence of locality and isotropic assumption i.e. $\langle \boldsymbol{j},\boldsymbol{j}\rangle = \langle \boldsymbol{j}^*,\boldsymbol{j}^*\rangle = 0$. In above phenomenological approach, the final results dependent on the physics properties of involved materials. Materials for which the optical properties are affected by the nonlocal phenomena such as anomalous skin effect are not included.

Ensemble average the Poynting vector

In order to calculate RHT, we need ensemble average the Poynting vector.

$$\langle \boldsymbol{S}(\boldsymbol{x},t)\rangle = \frac{\mathrm{Re}\langle \boldsymbol{E}(\boldsymbol{x},t)\times\boldsymbol{H}^*(\boldsymbol{x},t)\rangle}{2} \tag{2.6}$$

Field at particular point $\boldsymbol{x}$ is proportional to current sources at all point $\boldsymbol{x}'$. So we have the dyadic Green functions tensor[61], i.e., $\overleftrightarrow{G}^{ee}(\boldsymbol{x},\boldsymbol{x}',\omega)$ and $\overleftrightarrow{G}^{he}(\boldsymbol{x},\boldsymbol{x}',\omega)$.

$$\begin{aligned}
\boldsymbol{E}(\boldsymbol{x},t) &= \frac{1}{2\pi}\int_0^\infty d\omega' \int d\boldsymbol{x}' e^{i\omega' t}\overleftrightarrow{G}^{ee}(\boldsymbol{x},\boldsymbol{x}',\omega')\boldsymbol{j}_{source}(\boldsymbol{x}',\omega') + c.c \\
\boldsymbol{H}(\boldsymbol{x},t) &= \frac{1}{2\pi}\int_0^\infty d\omega' \int d\boldsymbol{x}' e^{i\omega' t}\overleftrightarrow{G}^{he}(\boldsymbol{x},\boldsymbol{x}',\omega')\boldsymbol{j}_{source}(\boldsymbol{x}',\omega') + c.c
\end{aligned} \tag{2.7}$$

The expression for ensemble average the Poynting vector is then contains eight fold integral over $\omega,\omega',\boldsymbol{x},\boldsymbol{x}'$ and reduced to four fold due to j-j correlation. According to Eq. (2.5) and (2.7), the radiative heat flux i.e. Eq. (2.6) can be calculate in the general

form:

$$\langle \boldsymbol{S}(\boldsymbol{x}) \rangle = \frac{1}{2}\mathrm{Re}\left\{ \frac{1}{(2\pi)^3}\frac{4}{\pi}\sum_a \int_0^\infty d\omega \int_V d\boldsymbol{x}' \epsilon''(\omega)\hbar\omega^2 \left[\frac{1}{e^{\hbar\omega/kT(\vec{x}')}-1}+\frac{1}{2}\right]\times G_{il}^{ee}(\boldsymbol{x},\boldsymbol{x}',\omega)G_{jl}^{he*}(\boldsymbol{x},\boldsymbol{x}',\omega)\right\} \tag{2.8}$$

Where we can get that the spectral heat flux $\boldsymbol{S}(\boldsymbol{x},\omega)$ is a linear combination of the field correlations. The integration of $\boldsymbol{S}(\boldsymbol{x},\omega)$ with frequency can derive the total heat flux $\boldsymbol{S}(\boldsymbol{x})$. And integration of the displacement components of $\boldsymbol{S}(\boldsymbol{x})$ over the object surface can derive the net heat current (energy flow per unit time).

2.1.3 The RHT between parallel-plane systems

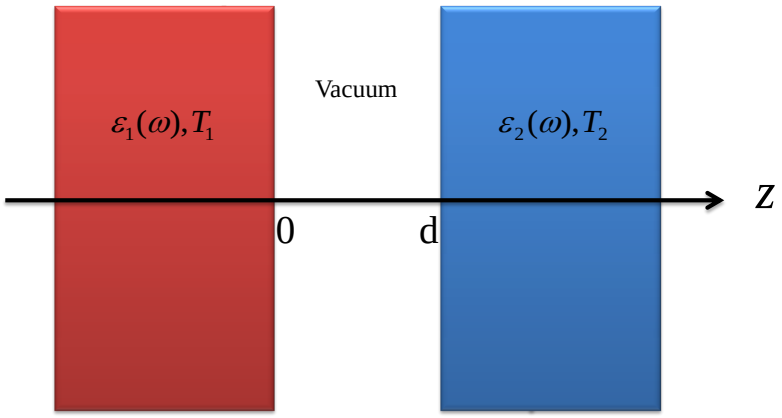

Fig. 2.1: Geometric situation for radiative heat transfer with semi-infinite planes configuration

Based on the theories and the general method sketched above, the RHT between different bodies can be defined. We presently offer a solution for the RHT between two parallel semi-infinite bodies separated by a vacuum gap (Fig. (2.1)), with the help of the well-known Green's function for this configuration[62]. Due to high symmetric, the

parallel-plane results became be analytically solved using Green's function. The various physical pictures can be obtained during the calculation. The total RHT over a vacuum gap d can be performed in a Landauer-type expression.

$$\langle \boldsymbol{S}(T_1, T_2, d)\rangle = \int_0^\infty \frac{d\omega}{4\pi^2}[\Theta(\omega, T_1) - \Theta(\omega, T_2)] \sum_\alpha \int_0^\infty dk k T_\alpha^{12}(\omega, k, d) \tag{2.9}$$

where $\Theta(\omega, T) = \frac{\hbar\omega}{e^{\hbar\omega/k_B T}-1}$ is the mean energy of a harmonic oscillator minus the zero point quantum fluctuation contribution with temperature T. $T_{1(2)}$ is the absolute temperatures of object 1(2). k is the wave vector component parallel to the planar surfaces, and T_α is the transmission probabilities for the TE and TM modes. They can be formulated regarding the Fresnel coefficients of the interfaces[63].

$$T^{12}_{\alpha=s,p}(\omega, k) = \begin{cases} \dfrac{(1-|r_\alpha^{01}|^2)(1-|r_\alpha^{02}|^2)}{|1-r_\alpha^{01}r_\alpha^{02}e^{2i\gamma_2 d}|^2}, & k < \dfrac{\omega}{c}. \\ \dfrac{4\mathrm{Im}(r_\alpha^{01})\mathrm{Im}(r_\alpha^{02})e^{-2\mathrm{Im}(\gamma_2)d}}{|1-r_\alpha^{01}r_\alpha^{02}e^{2i\gamma_2 d}|^2}, & k > \dfrac{\omega}{c}. \end{cases} \tag{2.10}$$

Where r_α^{ij} is the Fresnel reflection coefficients at the interfaces between vacuum and materials. And it is given by $r_s^{ij} = (\gamma_i - \gamma_j)/(\gamma_i + \gamma_j)$ or $r_p^{ij} = (\epsilon_j\gamma_i - \epsilon_i\gamma_j)/(\epsilon_j\gamma_i + \epsilon_i\gamma_j)$ and $\gamma_i = \sqrt{\epsilon_i(\omega)\omega^2/c^2 - k^2}$ is the transverse component of the wave vector in body i and $\epsilon_i(\omega)$ is the corresponding dielectric constant.

Eq. (2.9) and (2.11) have been derived only for calculation of RHT between two semi-infinite planes and are not sufficient to explain systems with thin films or layers. When the objects are not semi-infinite, a straightforward calculation of the RHT is hard to perform due to the shape effects and others complicated factors. However, when the emitter and receiver are not semi-infinite or the systems are multilayer systems, the calculation of RHT should properly account for the many emission sources or multiple reflections at interfaces. If we focus on the field in the vacuum gap, the same expression

can be obtained by replaced with modified reflection coefficient as below:

$$T^{12}_{\alpha=s,p}(\omega,k)=\begin{cases}\dfrac{(1-|R^{01}_{\alpha}|^2)(1-|R^{02}_{\alpha}|^2)}{|1-R^{01}_{\alpha}R^{02}_{\alpha}e^{2i\gamma_2 d}|^2}, & k<\dfrac{\omega}{c}.\\ \dfrac{4\mathrm{Im}(R^{01}_{\alpha})\mathrm{Im}(R^{02}_{\alpha})e^{-2\mathrm{Im}(\gamma_2)d}}{|1-R^{01}_{\alpha}R^{02}_{\alpha}e^{2i\gamma_2 d}|^2}, & k>\dfrac{\omega}{c}.\end{cases} \tag{2.11}$$

Where the R^i_α is the modified reflection coefficient, i.e. the total reflection coefficient for multilayer systems.

To give the results which can directly be compared with experimental measurements, the heat transfer coefficient at a mean temperature T can be defined as below:

$$h(T,d)=\lim_{T_1\to T_2}\left|\frac{\langle \boldsymbol{S}(T_1,T_2,d)\rangle}{T_1-T_2}\right|=\int_0^\infty\frac{d\omega}{4\pi^2}\frac{\partial\Theta(\omega,T)}{\partial T}\sum_\alpha\int_0^\infty dk k T^{12}_\alpha(\omega,k,d) \tag{2.12}$$

Based on the GF formalism, above equations for semi-infinite planes configuration can be used not only for the structured and composited systems with their dielectric constant but also for the novel new materials with unusual dielectric constant. Besides, except for the calculation for NFRHT between parallel planes, the GF formalism can also be used for other symmetric configurations such as dipole-plane, dipole-dipole, sphere-sphere, sphere-plane, and cylinder-cylinder.

2.2 Scalar wave method for radiative heat transfer between two semi-infinite planes

In above FE picture, Eq. (2.9) and (2.11) give the analytical formula for the RHT between two semi-infinite planes. In this section, we use the scalar wave method to rederive the similar formula for RHT between two semi-infinite planes based on fluctuation electrodynamics. One of the purposes of this section is to have a clear physical picture for fluctuation electrodynamic from the view of wave equation and then make a foundation for the quantum description in the below section. This section is the connection between FE and our below scalar wave quantum theory for the RHT.

2.2.1 Equation of motion and energy current density for scalar wave

Before the calculation of transmission for the RHT, we first indicate a brief description for the scalar wave. We start from the Lagrange action of scalar wave as the same as some textbook i.e. $S = \int \mathcal{L}dt = \int_V d^3\vec{r} \int_{t_0}^{t1} dt(\frac{1}{2}\dot{\phi}^2 - \frac{1}{2}v^2(\nabla\phi)^2)$ and apply variational principle of action to get the equation of motion for scalar wave[59]. The final standard wave equation of scalar wave are shown as below:

$$\nabla^2\phi - \frac{1}{v^2}\frac{\partial^2}{\partial t^2}\phi = 0 \tag{2.13}$$

Where v is the group velocity of scalar wave.

According to the expression of energy density and of scalar wave (or energy conservation law):

$$\begin{aligned} u &= \frac{1}{2}\left[\dot{\phi}^2 + v^2(\nabla\phi)^2\right], \\ \frac{\partial u}{\partial t} &+ \nabla\cdot\boldsymbol{j} = 0. \end{aligned} \tag{2.14}$$

Where u is the energy density of scalar wave. $\boldsymbol{j}$ is the energy current density for scalar wave. In different medium, the energy current density $\boldsymbol{j}$ can be derived obviously i.e.

$$\boldsymbol{j}_i = -v_i^2\dot{\phi}_i\nabla\phi_i \tag{2.15}$$

Where v_i and ϕ_i is the group velocity and scalar wave equation of medium i. Our calculations in this section focus on the computation of Eq. (2.15) from the view of scalar wave.

2.2.2 Boundary condition matching

The solution of Eq. (2.13) can be described by the standard plane wave i.e $Ae^{i(\boldsymbol{k}\cdot\boldsymbol{r}-\omega t)}$. As shown in Fig. (2.1), we assume that there is plane scalar wave incident from region 1 to region 2 through region 0 and reflect at two interfaces. Vice verse, the similar process is obtained when the scalar wave incoming from region 2 transmits to region

1. In Fig. (2.2), we show a sketch of the above process. Actually, the scalar wave should satisfy the previous wave equation $\ddot{\phi} - v_\alpha^2 \vec{\nabla}^2 \phi = 0$ in three regions. To solve the equation, we need carefully consider the boundary condition when the scalar wave across the interface. Obviously, the transverse component (perpendicular to z direction in Fig. (2.2)) of wave vector keep the same during the propagation and the dispersion relation in the different regions is different.

$$\begin{aligned} \boldsymbol{k}_1^\perp &= \boldsymbol{k}_0^\perp = \boldsymbol{k}_2^\perp = (k_x, k_y) \\ |\boldsymbol{k}_1|^2 &= \frac{\omega^2}{v_1^2}, |\boldsymbol{k}_0|^2 = \frac{\omega^2}{v_0^2}, |\boldsymbol{k}_2|^2 = \frac{\omega^2}{v_2^2} \end{aligned} \tag{2.16}$$

Where $|\boldsymbol{k}|^2 = k_x^2 + k_y^2 + k_z^2$.

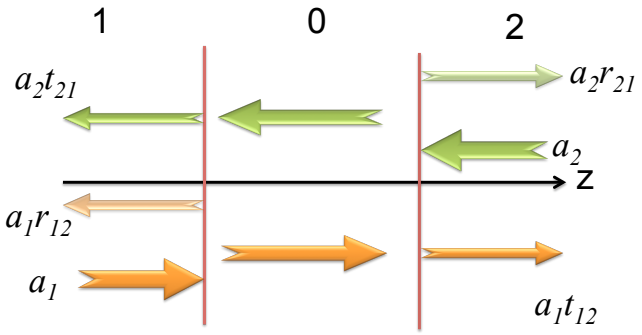

Fig. 2.2: Boundary scatter process of scalar wave betweeen two interfaces.

When the scalar wave incidents from region 1 and multiple reflects in region 0, the energy can transmit to region 2. In this physical picture, we can write the solution of wave equation in the three regions[64].

$$\phi(\boldsymbol{r}, t) = e^{i(\boldsymbol{k}^\perp \cdot \boldsymbol{r}^\perp - i\omega t)} \begin{cases} e^{ik_z^1 z} + r_{12} e^{-ik_z^1} & z < 0 \\ A e^{ik_z^0 z} + B e^{-ik_z^0 z} & 0 < z < d \\ t_{12} e^{k_z^2 z} & z > d \end{cases} \tag{2.17}$$

Where $\boldsymbol{r}^{\perp}$ is vector in $x-y$ plane, i.e. $\boldsymbol{r}^{\perp} = r(x,y)$. We assume that the amplitude of incident scalar wave is normalized to 1. r_{12} is the amplitude of the reflected wave and t_{12} is the amplitude of the transmitted wave. In the center region, it is a superposition of forwards and backwards moving waves. A and B are amplitude of those waves. If group velocity in region 0 (v_0) larger than v_1 or v_2, k_z^0 may be pure imaginary. In that condition, the wave in the region 0 is evanescent.

Boundary condition at $z = 0$:

$$\begin{aligned} &\phi \text{ is continuous} : 1 + r_{12} = A + B \\ &j_z \text{ is continuous} : v_1^2[1 - r_{12}]k_z^1 = v_0^2[Ak_z^0 - Bk_z^0] \end{aligned} \tag{2.18}$$

Boundary condition at $z = d$:

$$\begin{aligned} &Ae^{ik_z^0 d} + B^{-ik_z^0 d} = t_{12}e^{ik_z^2 d} \\ &v_0^2[Ae^{ik_z^0 d} + B^{-ik_z^0 d}]k_z^0 = v_2^2 t_{12} k_z^2 e^{ik_z^2 d} \end{aligned} \tag{2.19}$$

After solving above formula carefully, we can get the final expression of transmission:

$$t_{12} = \frac{1}{\varphi_2} \frac{\varphi_0 t_{10} t_{02}}{1 - r_{01} r_{02} \varphi_0^2} \tag{2.20}$$

Where, $t_{ij} = \frac{2\xi_i}{\xi_i + \xi_j}$, $r_{ij} = \frac{\xi_i - \xi_j}{\xi_i + \xi_j}$, $\xi_i = (v_i)^2 k_z^i, \varphi_i = e^{ik_z^i d}$.

2.2.3 Derivation for the Landauer formula

In previous section, we obtain the transmitted amplitude of scalar wave in region 2. The next procedure is to get a derivation for Landauer like formula from the view of scalar wave. In below calculation, we use quasi-one-dimensional geometry so that the energy is only transported in z direction. And quantum theory is needed to obtain the Bose-Einsein distribution for the scalar wave.

As showing in Fig. (2.3), the width of region 0 is finite with d. The widths of region 1 and region 2 are extended to semi-infinite in the opposite directions. The area of cross-section in (x, y) direction is set as $L^2 = A$. It is convenient to use periodic

boundary conditions in the transverse (x, y) direction.

$$\phi(x + L, y, z) = \phi(x, y + L, z) = \phi(x, y, z) \tag{2.21}$$

With standard quantization procedure, the wave function in transverse direction are quantized as below:

$$\phi(x, y, z, t) = \sum_{\boldsymbol{k}^\perp} c_{\boldsymbol{k}^\perp}(z, t) e^{i\boldsymbol{k}^\perp \cdot \boldsymbol{r}^\perp} \tag{2.22}$$

Where, we have $\boldsymbol{k}^\perp = (k_x, k_y) = (\frac{2\pi l_x}{L}, \frac{2\pi l y}{L})$. In continuous limit, we have:

$$\sum_{\boldsymbol{k}^\perp} \to \sum (\frac{L}{2\pi})^2 \Delta k_x \Delta k_y \to (\frac{L}{2\pi})^2 \int_{-\infty}^{+\infty} dk_x dk_y \tag{2.23}$$

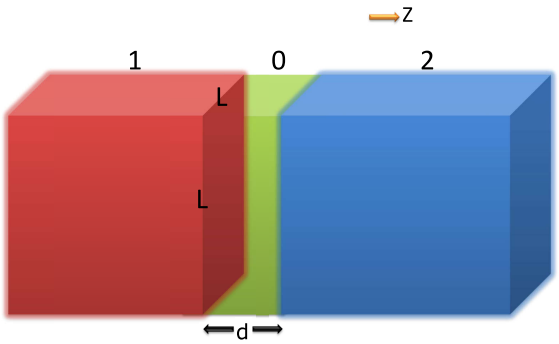

Fig. 2.3: A 3-d sketch for boundary matching condition of Laudauer Formula.

Then we quantize the wave function when the wave transmits from left side to right side as below:

$$\hat{\phi}_L(\boldsymbol{r}, t) = \sum_{\boldsymbol{k}^\perp, k_z^1 > 0} \sqrt{\frac{\hbar}{2\omega(\boldsymbol{k}) L^2 d}} \left[a_{\boldsymbol{k}}^L c_{\boldsymbol{k}}^L(z) e^{i(\boldsymbol{k}^\perp \cdot \boldsymbol{r}^\perp - \omega t)} + \text{H.c.} \right] \tag{2.24}$$

$$c_k^L(z) = \begin{cases} e^{ik_z^1 z} + r_{12} e^{-ik_z^1 z} \\ A e^{ik_z^0 z} + B e^{-ik_z^0 z} \\ t_{12} e^{ik_z^2 z} \end{cases} \tag{2.25}$$

Where L means the wave in the left side (region 1). Noted that when the wave vector of incoming wave is specified, i.e. $\boldsymbol{k}^{\perp}, k_z^1$ is given, k_z^0 and k_z^2 can be calculated from the dispersion relation and boundary condition. So we need to take a summation of k_z^1. We have

$$\begin{aligned}
&[a_{\boldsymbol{k}}^L a_{\boldsymbol{k}}^{L\prime}] = \delta_{\boldsymbol{k}\boldsymbol{k}'} \\
&\langle a_{\boldsymbol{k}}^L a_{\boldsymbol{k}}^{L\prime}\rangle = 0\ ,\ \langle a_{\boldsymbol{k}}^{\dagger L} a_{\boldsymbol{k}}^{\dagger L\prime}\rangle = 0\ ,\ \langle a_{\boldsymbol{k}}^L a_{\boldsymbol{k}}^{R\prime}\rangle = 0 \\
&\langle a_{\boldsymbol{k}}^{\dagger L} a_{\boldsymbol{k}}^{L\prime}\rangle = \delta_{\boldsymbol{k}\boldsymbol{k}'} n_{\boldsymbol{k}} = \delta_{\boldsymbol{k}\boldsymbol{k}'} \frac{1}{e^{\beta_L \hbar\omega_{\boldsymbol{k}}} - 1}
\end{aligned} \tag{2.26}$$

Where $a_{\boldsymbol{k}}^L$ and $a_{\boldsymbol{k}^{L\dagger}}$ are the annihilation and creation operators for the scalar wave on the left side. $n_{\boldsymbol{k}}$ is the Boson distribution.

Next we give a detailed calculation for the Landaur form of the energy current density. At first, we assume that the incident wave, the refracted wave and the transmitted wave are independent with each other i.e. $\phi_{tot} = \phi_i + \phi_r + \phi_t$. If the wave incidents from region 1, the energy transmitted to region 2 can be calculated from the transmitted wave i.e. $\hat{\phi}_t^R(\boldsymbol{r}, t)$. According to Eq. (2.24) and (2.25), the transmitted wave can be written as below:

$$\hat{\phi}_t^R(\boldsymbol{r}, t) = \sum_{\boldsymbol{k}^{\perp}, k_z^1 > 0} \sqrt{\frac{\hbar}{2\omega(\boldsymbol{k}) L^2 d}} \left[a_{\boldsymbol{k}}^L t_{12} e^{ik_z^2} e^{i(\boldsymbol{k}^{\perp}\cdot\boldsymbol{r}^{\perp} - \omega t)} + \text{H.c.} \right] \tag{2.27}$$

Where the summation is over the wave vector on the region. The energy current transmitted from the region 1 to the region 2 can be calculated from the equantion (2.33):

$$\begin{aligned}
j_t^R = &- v_2^2 \sum_{\boldsymbol{k}^{\perp}, k_z^1 > 0} \sqrt{\frac{\hbar}{2\omega(\boldsymbol{k}) L^2 d}} \left[(-i\omega) a_{\boldsymbol{k}}^L t_{12} e^{ik_z^2 z} e^{i(\boldsymbol{k}^{\perp}\cdot\boldsymbol{r}^{\perp} - \omega t)} + \text{H.c.} \right] \times \\
&\sum_{\boldsymbol{k}'^{\perp}, k_z^{1\prime} > 0} \sqrt{\frac{\hbar}{2\omega(\boldsymbol{k}') L^2 d}} \left[(ik_z'^1) a_{\boldsymbol{k}'}^L t_{12} e^{ik_z'^2 z} e^{i(\boldsymbol{k}'^{\perp}\cdot\boldsymbol{r}^{\perp} - \omega' t)} + \text{H.c.} \right]
\end{aligned} \tag{2.28}$$

Then we take ensemble average of the operator i.e. $\langle \hat{O} \rangle = \text{Tr}(\frac{e^{-\beta_L H_L}}{Z})$. β_L equals to $1/k_b T_L$ and T_L is the temperature in the left side. H_L is the Hamiltonian in the left side. Z is partition function. According to the Eq. (2.25) and the dispersion relation,

the ensemble average of the transmitted energy current can be written as below:

$$\begin{aligned}\langle j_t^R\rangle =& -v_2^2 \sum_{\boldsymbol{k}^\perp, k_z^1>0} \frac{\hbar}{2\omega(\boldsymbol{k})L^2 d}|t_{12}|^2(-i\omega)(-ik_z^2)\langle(a_{\vec{k}}^L a_{\vec{k}}^{L\dagger} + a_{\vec{k}}^{L\dagger} a_{\vec{k}}^L)\rangle \\ =& \sum_{\vec{k}^\perp, k_z^1>0} \frac{\hbar}{V} v_2^2 k_z^2 |t_{12}|^2 \langle \frac{1}{2}(a_{\vec{k}}^L a_{\vec{k}}^{L\dagger} + a_{\vec{k}}^{L\dagger} a_{\vec{k}}^L)\rangle \\ =& \sum_{\vec{k}^\perp, k_z^1>0} \frac{\hbar}{V} v_2^2 k_z^2 |t_{12}|^2 (n_{\boldsymbol{k}}^L + \frac{1}{2})\end{aligned} \tag{2.29}$$

The same calculation can be performed for the energy current transmitted from the region 2 to the region 1:

$$\langle j_t^L\rangle = \sum_{\boldsymbol{k}^\perp, k_z^2<0} \frac{\hbar}{V} v_1^2 k_z^1 |t_{21}|^2 (n_{\boldsymbol{k}}^R + \frac{1}{2}) \tag{2.30}$$

Since $\omega^2 = [(k_z^i)^2 + (k_i^\perp)^2]v_i^2$, we can get the relation between ω and z component wave vector k_z^i with the fixed $k_i^\perp$:

$$\begin{aligned}&\omega d\omega = v_i^2 k_z^i dk_z^i \\ &\frac{1}{d}\sum_{k_z^i>0} \to \frac{1}{2\pi}\int_0^\infty \frac{\omega d\omega}{v_i^2 k_z^i}\end{aligned} \tag{2.31}$$

Where we take variable substitution according to the continuous dispersion relation and change the summation of k_z^i into frequency domain. Then the Eq. (2.29) and (2.30) can be written with a more simplify way:

$$\begin{aligned}\langle j_t^R\rangle =& \frac{1}{L^2}\sum_{\boldsymbol{k}^\perp}\int_0^\infty \frac{d\omega}{2\pi}\hbar\omega \frac{v_2^2 k_z^2}{v_1^2 k_z^1}|t_{12}|^2(n_{\boldsymbol{k}}^L + \frac{1}{2}) \\ \langle j_t^L\rangle =& \frac{1}{L^2}\sum_{\boldsymbol{k}^\perp}\int_0^\infty \frac{d\omega}{2\pi}\hbar\omega \frac{v_1^2 k_z^1}{v_2^2 k_z^2}|t_{21}|^2(n_{\boldsymbol{k}}^R + \frac{1}{2})\end{aligned} \tag{2.32}$$

In thermal equilibrium i.e. $T_1 = T_2$, the net heat current should equal to zero according to the first law of thermodynamics. That means $\langle j_t^R\rangle$ should equals to $\langle j_t^L\rangle$ and our derivations must have $\frac{v_2^2 k_z^2}{v_1^2 k_z^1}|t_{12}|^2 = \frac{v_1^2 k_z^1}{v_2^2 k_z^2}|t_{21}|^2$. Actually this relation also can be derived easily from the Eq. (2.20). The consistence between two derivation indicates the self-consistence for our scalar wave calculation. Then if we define that

$\frac{v_1^2 k_z^1}{v_2^2 k_z^2}|t_{21}|^2 = \frac{v_2^2 k_z^2}{v_1^2 k_z^1}|t_{12}|^2 = T_{12}(\omega, \boldsymbol{k}^\perp)$, the final net energy current density from the region 1 to the region 2 can be written as a Landauer form:

$$\langle j_{net} \rangle = \langle j_t^L \rangle - \langle j_t^R \rangle = \int_0^\infty \frac{d\omega}{2\pi} \hbar\omega \int \frac{dk_x dk_y}{(2\pi)^2} T_{12}(\omega, \boldsymbol{k}^\perp)(n_{\boldsymbol{k}}^L - n_{\boldsymbol{k}}^R) \tag{2.33}$$

Where $n_{\boldsymbol{k}}^{L(R)}$ is the Bose distribution with the temperature of left(right) region.

Due to the energy conservation, we have the below relation for t_{ij} and r_{ij}:

$$v_2^2 k_z^2 |t_{12}|^2 = v_1^2 k_z^1 (1 - |r_{12}|^2) \tag{2.34}$$

$$v_1^2 k_z^1 |t_{21}|^2 = v_2^2 k_z^2 (1 - |r_{21}|^2) \tag{2.35}$$

Based on Eq. (2.20), (2.32) and (2.34), we can calculate the expression of the transmission with the scalar wave view.

$$T_{12}(\omega, \boldsymbol{k}^\perp) = \begin{cases} \dfrac{(1 - |r_\alpha^{10}|^2)(1 - |r_\alpha^{02}|^2)}{|1 - r_\alpha^{10} r_\alpha^{02} e^{2ik_z^0 d}|^2}, & |\boldsymbol{k}^\perp| < \dfrac{\omega}{v_0}. \\ \dfrac{4\mathrm{Im}(r_\alpha^{10})\mathrm{Im}(r_\alpha^{02}) e^{-2\mathrm{Im}(k_z^0)d}}{|1 - r_\alpha^{10} r_\alpha^{02} e^{2ik_z^0 d}|^2}, & |\boldsymbol{k}^\perp| > \dfrac{\omega}{v_0}. \end{cases} \tag{2.36}$$

Where we rederive Eq. (2.9) and (2.11). The consistence between those calculation indicates a useful benchmark between FE and our scalar wave calculation. However, the results in this section are just a connection between FE and our quantum theory for longitudinal photon. In Chapter 4, we will extend this scalar-field method for to quantum region with the help of NEGF formalism.

2.2.4 Example: near-field phonon effects

In this subsection, we investigate the near-field phonon effects based on our scalar wave method for the RHT. This is an extended example for our scalar wave theory. Phonon, i.e., a collective excitation in a periodic system can also be described by a linear dispersion relation in the small wave vector k region. Similar with the photon, the phonon can also emit from one body to another, and we call it as the phonon radiation regime. However, reaching the phonon radiation regime needs high-quality materials

and length scales should be much smaller than the intrinsic phonon-phonon scattering mean free paths (MFPs)[65]. In the room temperature, MFPs of phonon almost equal to 10 nm. In low temperature, MFPs can reach the micrometer region. That means that the phonon in thermal interface material (TIM) are like ballistic and the phonon-phonon scattering process is low when phonon is transported through the TIM . Typically, there should be a limit called phonon blackbody limit for thermal conductance. Actually, similar to the fact that NFRTH can break the BB limit for the photon, the near-field phonon effect can also break the phonon blackbody limit, enhance the heat conduction and does not based on the phonon-phonon scattering process (DMM). Based on this near-field phonon effects, another thermal transport channel can be found in TIM.

Phonon Black-body limit

Acoustic mismatch model (AMM) At first, we derive the phonon blackbody limit through the AMM. In that model, one assumption is that the phonon is administered by continuum acoustics and interface is explained as a plane[66]. And we only consider two semi-infinite isotropic solid in the $x-y$ plane and suppose that the modulus of rigidity of both materials is zero and neglect the transverse phonons in both sides.

In above simple model, one can obtain the expression as below[67]:

$$\frac{dQ}{dt} = \frac{k_B^4 \Gamma A}{4\pi^2 \hbar^3 v_1^3}[T_1^4 f(T_1) - T_2^4 f(T_2)] \tag{2.37}$$

Here, we have $f(T) = \int_0^{\hbar\omega/k_B T} \frac{z^3 dz}{e^z - 1}, z = \hbar\omega/k_B T, \Gamma = \int_0^{\pi/2} \alpha_1(\theta_1) \sin\theta_1 \cos\theta_1 d\theta_1$. At low temperature, we can make $\hbar\omega/k_B T \to \infty$. In the integral over z as it occurs in the Debye theory of specific heats and we can obtain the relation:

$$\frac{dQ}{dt} = \frac{k_B^4 \Gamma A}{4\pi^2 \hbar^3 v_1^2}(\frac{\pi^4}{15})[T_1^4 - T_2^4] \tag{2.38}$$

Thermal radiation limit In that limit, all phonons from the lower phonon density side are assumed to be transmitted. In the higher phonon density side, enough phonons can be transmitted with serving the principle of detailed balance and the second law

of thermodynamics. That is the maximum thermal transport through phonon which does not violate the principle of detailed balance. We also call it as *"Perfect match model"*[66].

For bulk material at low temperature, in the absence of scattering process, we can build the virtual photon blackbody-like formula i.e. phonon blackbody limit. At low temperature, in an isotropic condensed matter, we introduce the Stefan-Boltzmann constant σ_{phonon} through Eq. (2.38):

$$\sigma_{phonon} = \frac{\pi^2 k_B^4}{120\hbar^3} \sum_i \frac{1}{v_i^2} = \frac{\pi^2 k_B^4}{40\hbar^3} \overline{\frac{1}{3} \sum_i \frac{1}{v_i^2}} \tag{2.39}$$

Where v_i is the group velocity. And phonon has one longitudinal and two transverse branches.

In the phonon blackbody limit, the heat transfer between two body does not dependent on the properties of the left and right material except the temperature. Through Eq. (2.39), we can easily calculate the heat transfer between two bodies in the phonon blackbody limit.

For example, if we set the average group velocity in the middle as $v = 2\ km/s$, temperature $T_1 = 300K\ T_2 = 200K$ and assume the group velocity of three branches are the same, we can get the limited heat transfer:

$$\begin{aligned} \dot{Q}_{phonon} =& \sigma_{phonon}(T_1^4 - T_2^4) = 1.911 \times 10^3 \times (300^4 - 200^4)\ \mathrm{W/m^2} \\ \dot{Q}_{photon} =& 5.670373 \times 10^{-8} \times (300^4 - 200^4)\ \mathrm{W/m^2} \end{aligned} \tag{2.40}$$

Near-field phonon calculation

The near-field phonon calculation is based on the previous scalar wave method. Although our primary goal for the scalar wave method is to rederive the FE results for the RHT, the scalar photon and phonon are similar with each other except the different group velocities and our scalar wave method is still valid for the phonon transport calculation. Due to the similarity between phonon and photon, is there a similar near-field effect for the phonon transport? Fig. (2.4) shows the schematic diagram for the near-field phonon

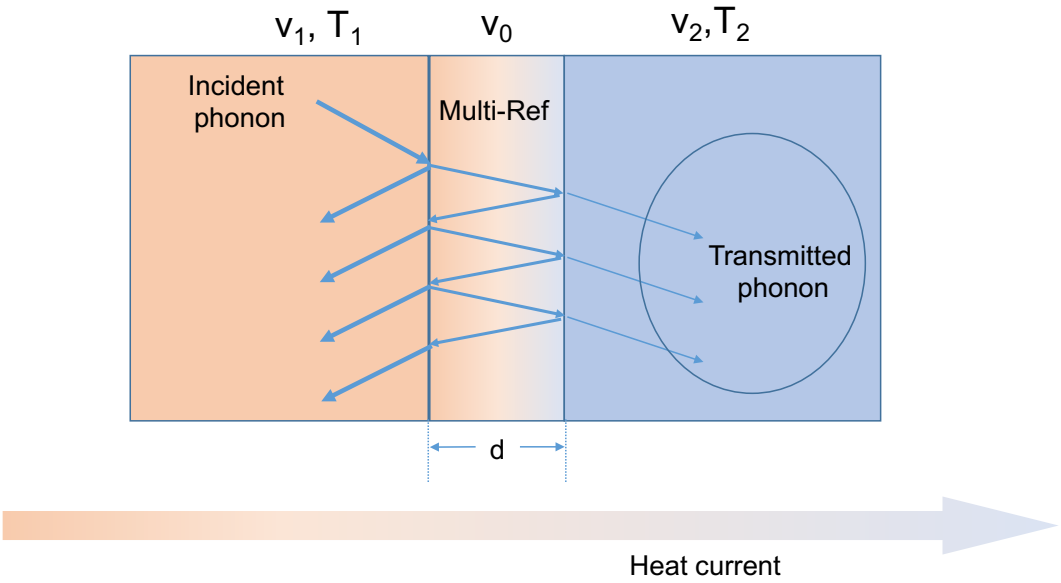

Fig. 2.4: Sketch for near-field phonon effects

thermal transport: the phonon incidents from the region 1 with group velocity v_1 to the region 0 at first, the phonon is reflected at the interface and multiply reflected in the region 0 with group velocity v_0, finally the energy carried by phonon will be transmitted to the region 2 with group velocity v_2. The total energy transfer by phonon can be calculated from the equation(2.33) and (2.36).

Near-field phonon vs phonon black-body limit

The numerical result of the near-field phonon calculation is presented in Fig. (4.8). It shows that in some particular cases, the heat transfer through thermal interface material due to the near-field phonon effects can be even larger than phonon blackbody limit. For example, if we set the model parameter as shown in the figure, we find that when we increase the group velocity of the middle materials (different thermal interface materials), the BB phonon heat transfer will be decreased, but the near-field phonon heat transfer will be changed periodically. Such novel effect indicates that the near-field phonon effect can enhance heat transfer through thermal interface materials. When we choose $v_0 = 17.5\mathrm{km/s}$, the heat transferred by the near-field phonon can be several times larger than phonon blackbody limit results. This result indicates that in a small distance and

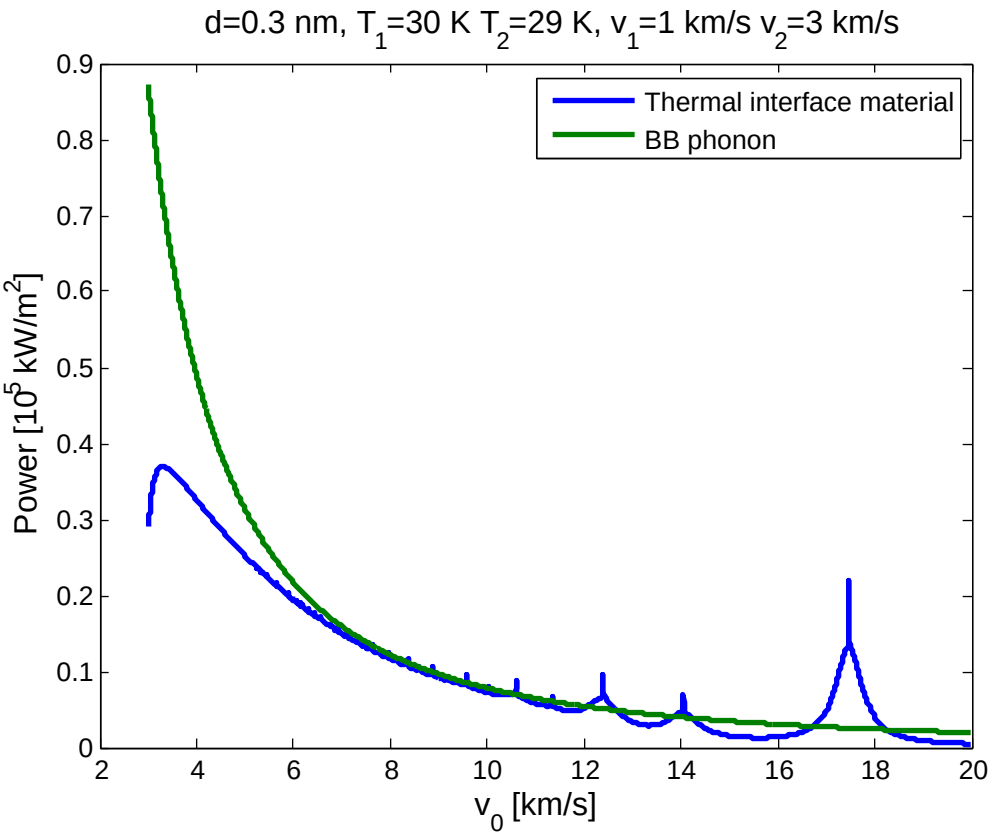

Fig. 2.5: Total heat transfer vs Blackbody phonon effects. The parameter are showed in the title.

low-temperature region, the heat transfer can be dominated by the near-field phonon effects. Our results can numerically provide a unique channel for heat transfer when two bodies are separated by a very small distance. However, there are still some challenges for the near-field phonon effects. According to our calculation, the near-field phonon effects can only be found when the separation between two bodies is tiny small. It is not easy to achieve and measure such condition experimentally.

2.3 Nonequilibrium Green's function method

In this section, we present a general review for the non-equilibrium Green's functions (NEGF). The NEGF is an extension of the standard equilibrium formulation on the imaginary-time axis[68] and is a very useful tool for various research areas. Some general

review can be found in the reference [69–71]. Here, we will brief review the NEGF with non-equilibrium steady state assumption. It is easier to understand the NEGF because the formula for NEGF is greatly simplified in that condition.

2.3.1 Contour-ordered formulation

A general quantum system is driven by an external field and the time evolution of this system is described by a time-dependent Hamiltonian $H(t)$. The system is assumed to be in a mixed state initially $t = 0$, which can be described by the density matrix shown as below:

$$\rho(0) = \frac{1}{\mathcal{Z}} e^{-\beta \mathcal{H}(0)} \tag{2.41}$$

Where $\mathcal{Z} = \mathrm{Tr} e^{-\beta H(0)}$ is the equilibrium partition function. $\beta = 1/k_B T$ is the inverse of temperature times Boltzmann constant. $\mathcal{H} = H(t) - \mu N(t)$ (μ is the chemical potential and $N(t)$ is the number operator for the particles). Here, we discuss only one general quantum system. However, for transport studies, when the systems evolve several leads, we need rewrite Eq. (2.41) with a constrained equilibrium partition function. If the driving field is opened, the system will evolve with time and the time evolution of the system is calculated by the von Neumann equation:

$$i\hbar \frac{d\rho(t)}{dt} = [\mathcal{H}(t), \rho(t)] \tag{2.42}$$

Where $[\cdots, \cdots]$ is the commutator. And the solution can be written by the unitary evolution operator:

$$\rho(t) = U(t,0)\rho(0)U(0,t) \qquad U(t,t') = \begin{cases} \mathcal{T} e^{-i\int dt \mathcal{H}(t)}, t > t' \\ \bar{\mathcal{T}} e^{-i\int d\bar{t} \mathcal{H}(\bar{t})}, t < t' \end{cases} \tag{2.43}$$

Where $\mathcal{T}(\bar{\mathcal{T}})$ is time-ordering (anti-time-ordering) operator. In general, the Hamiltonians at different times do not commute with each other. Then the expectation value of an

observable operator $O(t)$ at time t can be written as below:

$$\langle O(t)\rangle = \mathrm{Tr}[\rho(t)O] \tag{2.44}$$

Combing with Eq. (2.43) and (2.44) and evolve the operator along the imaginary-time axis from 0 to $-i\beta$, the Eq. (2.44) can be written with imaginary-time ordering:

$$\langle O(t)\rangle = \frac{1}{\mathcal{Z}}\mathrm{Tr}[U(-i\beta,0)U(0,t)OU(t,0)] \tag{2.45}$$

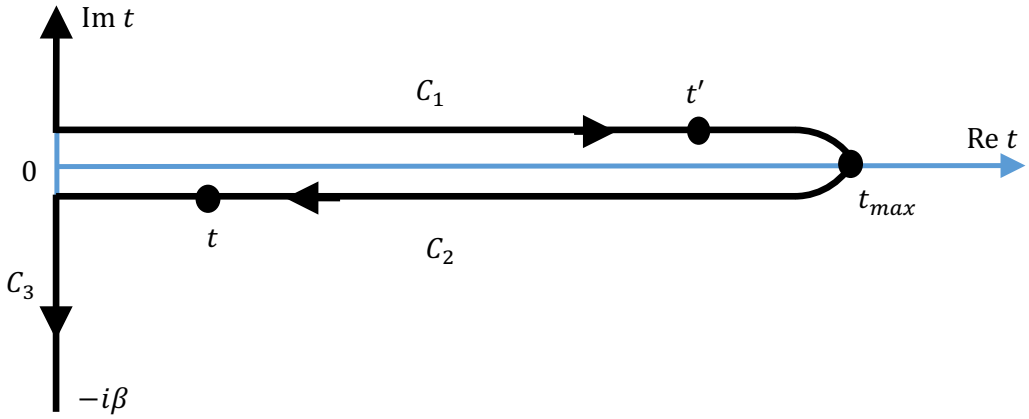

Fig. 2.6: The L-shaped contour $C = C_1 \cup C_2 \cup C_3$ in the Kadanoff-Baym formulism. The arrow means contour order and $t > t'$.

When reading Eq. (2.45) from right to left, we can find that the operator following the time ordering i.e $0 \to t \to 0 \to -i\beta$. Next, we can define such L-shaped contour C with three branches as shown in Fig. (2.6), i.e. $C_1 : 0 \to t_{max}$, $C_2 : t_{max} \to 0$ and $C_3 : 0 \to -i\beta$, where t_{max} is the maximal time for the system evolving[46]. In such contour order, the expectation value of the operator can be rewritten as below:

$$\langle O(t)\rangle = \frac{\mathrm{Tr}\left[\mathcal{T}_C e^{-i\int_C d\bar{t}\mathcal{H}(\bar{t})}O(t)\right]}{\mathrm{Tr}\left[\mathcal{T}_C e^{-i\int_C d\bar{t}\mathcal{H}(\bar{t})}\right]} \tag{2.46}$$

Where $\mathcal{T}_C$ is the contour-ordering operator. The contour-ordered formalism is a power tool for the calculation of high-order correlation function and it is convenient for the

perturbation. expansion.

$$\langle \mathcal{T}_C A(t)B(t')\rangle = \frac{1}{\mathcal{Z}}\mathrm{Tr}\left[\mathcal{T}_C e^{-i\int_C d\bar{t}\mathcal{H}(\bar{t})}A(t)B(t')\right] \tag{2.47}$$

Where A and B is the combinations of creation and annihilation operators. In this expression, the contour-ordered product of two operator can be written as below:

$$\mathcal{T}_C A(t)B(t') = \theta_C(t,t')A(t)B(t') \pm \theta_C(t',t)B(t')A(t) \tag{2.48}$$

Where $\theta_C(t,t')$ is the step function. $\pm$ is determined by the fermionic or bosonic properties of the operators. In the actual calculation, we need specify which branch the operator lies on.

2.3.2 Keldysh contour order

The Keldysh formalism is a useful and simpler approach to the nonequilibrium Green's functions, which is appropriate for the non-equilibrium steady state description[44]. The energy sent to the system by the driving field keeps balance with the energy provided by the environment in the nonequilibrium steady state. In the Keldysh formalism, the initial states are not interacted with each other and the interactions are adiabatically turned on from $t \to -\infty$. So there is no interaction vertex on the imaginary-time axis in contour order. That means, in Fig. (2.6), the imaginary contour order will decouple with up and down branches. And the Kadanoff-Baym contour order can simplified to the Keldysh contour order (Fig. (2.7)).

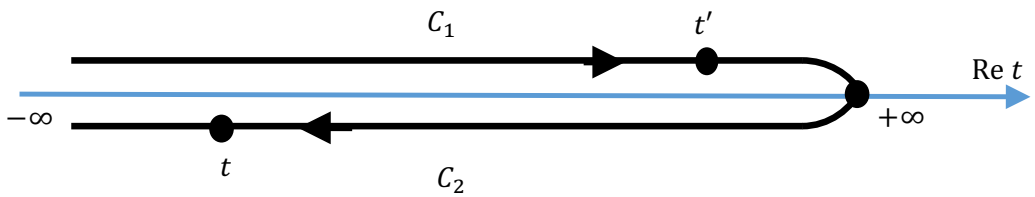

Fig. 2.7: The Keldysh contour with up and down branches ranging from $t = -\infty$ to $t = +\infty$.

2.3.3 Contour-ordered Green's functions

In this section, we start from the single-particle Green's functions, which are the fundamental elements for many-body theory.

$$G(\tau,\tau') = -\frac{i}{\hbar}\left\langle \mathcal{T}_C c(\tau) c^\dagger(\tau')\right\rangle \tag{2.49}$$

Where $\tau(\tau')$ is the time in contour order. $c(c^\dagger)$ is the a creation (annihilation) operator of particles. We do not obtain the spin and other indices in above definition. The contour-ordered Green's functions have 3×3 components because there are three branches. But in Keldysh contour order i.e. non-equilibrium steady state, the Green's function is much simpler i.e. 2×2. For convenience, we express the Green's functions with matrix form i.e.

$$\hat{G} = \begin{pmatrix} G^{++} & G^{+-} \\ G^{-+} & G^{--} \end{pmatrix} = \begin{pmatrix} G^{t} & G^{<} \\ G^{>} & G^{\bar{t}} \end{pmatrix} \tag{2.50}$$

Where $+(-)$ means up(down) branches in Keldysh contour order. $G^{t(\bar{t})}$ is the time-ordered (anti-time-ordered) Green's function. $G^{>(<)}$ is the greater(lesser) Green's function. In our calculations, we are more interested in the G^r and G^a i.e. retarded Green's function and advanced Green's function. The definition for the Green's functions we are concerned are given below in real time:

$$\begin{aligned} G^{>}(t,t') &= -\frac{i}{\hbar}\left\langle c(t)c^\dagger(t')\right\rangle \\ G^{<}(t,t') &= \pm\frac{i}{\hbar}\left\langle c^\dagger(t')c(t)\right\rangle \\ G^{r}(t,t') &= -\frac{i}{\hbar}\theta(t-t')\left\langle [c(t),c^\dagger(t')]_\pm\right\rangle \\ G^{a}(t,t') &= \frac{i}{\hbar}\theta(t'-t)\left\langle [c(t),c^\dagger(t')]_\pm\right\rangle \end{aligned} \tag{2.51}$$

Where in $\pm$, $+$ for fermi operator and $-$ for boson operator. $[,]_\pm$ is anti-commutator (commutator). $\theta(t)$ is the step function. For simplify, we only use fermions as a example

in the below section. For above four Green's functions, there is relation:

$$G^{>} - G^{<} = G^{r} - G^{a} = -iA. \tag{2.52}$$

Where A is the spectrum function.

Besides, for free particles, i.e., no interaction between electrons and electron's other degrees of freedom, the equation of motion for Green's function can be derived from Schödinger equation:

$$\left(i\hbar\frac{\partial}{\partial t} - H\right) G^{>,<}(t,t') = 0, \tag{2.53}$$

$$\left(i\hbar\frac{\partial}{\partial t} - H\right) G^{r}(t,t') = \delta(t-t')I. \tag{2.54}$$

Where H is the Hamiltonian and I is the identity matrix.

2.3.4 Dyson equation

To indicate nonequilibrium systems using Green's functions, we need to combine the self-energy Σ and the noninteracting Green's function G_0. In the Feynman diagram, the sum of all irreducible diagrams of the interacting Green's function G is named as the self-energy. Actually, the self-energy is defined on the same contour order with Green's function and the similar symmetry and boundary conditions can also working for the self-energy. The interacting Green's function G can be described by the Dyson equation:

$$\begin{aligned} G =& G_0 + G_0\Sigma G_0 + G_0\Sigma G_0\Sigma G_0 + \dots \\ =& G_0 + G_0\Sigma G \end{aligned} \tag{2.55}$$

When the self-energy is determined, the full Green's function can be derived from the Eq. (2.55), which is a numerical problem for the calculation.

2.3.5 Fluctuation dissipation theory and Keldysh equation

For equilibrium systems, we have the fluctuation dissipation relation for Green's function in frequency space:

$$\begin{aligned} G^{<}(\omega) &= -f(\omega)\left[G^{r}(\omega) - G^{a}(\omega)\right] = if(\omega)A(\omega) \\ G^{>}(\omega) &= i[1 + f(\omega)]A(\omega) \end{aligned} \tag{2.56}$$

Where $G^{>,<,r,a}(\omega)$ is the corresponding Green's function in frequency domain. $f(\omega)$ is the particle distribution, i.e., Fermi function.

For nonequilibrium steady state, we have the Keldysh equation:

$$G^{>,<}(\omega) = G^{r}(\omega)\Sigma^{>,<}(\omega)G^{a}(\omega) \tag{2.57}$$

Where $\Sigma^{>,<}$ is the greater (lesser) self-energy.

In the actual calculation, once we know all the Green's functions, the physical quantity can be calculated. For example, the current out of the bath can be calculated from the Meir-Wingreen formula[72], which is the standard formula for calculating the current through various systems.

$$I_{\mathrm{Fermi}} = \int_{-\infty}^{+\infty} \frac{d\omega}{2\pi}\hbar\omega\left[G^{>}(\omega)\Sigma^{<}(\omega) - G^{<}(\omega)\Sigma^{>}(\omega)\right], \tag{2.58}$$

$$I_{\mathrm{Boson}} = -\int_{-\infty}^{+\infty} \frac{d\omega}{4\pi}\hbar\omega\left[D^{>}(\omega)\Pi^{<}(\omega) - D^{<}(\omega)\Pi^{>}(\omega)\right]. \tag{2.59}$$

where I_{Fermi} is the current out of the fermi bath and I_{Boson} is the current out of the Boson bath. D and Π are Green's functions and self-energy of boson. When the interaction between particles is ignored, above formulas can be reduced to the Landauer formulas.

Chapter 3

Thermal management in MoS_2 based integrated device using near-field radiation

"No problem is too small or too trivial
if we can really do something about it."
—Richard Feynman

3.1 Introduction

There has been increasing interest in using the transition metal dichalcogenide (TMD) compounds, MX_2 (where M 1/4 Mo/W, X 1/4 S/Se/Te) for electronic and photonic devices, including logic transistors, optoelectronic, memories, lightemitters, photovoltaic and photodetectors, together with physical phenomena such as coupled spin-valley physics[73, 74]. Single-layer MoS_2, a member of the TMD family, is a semiconductor with a large band gap and has been regarded as a promising candidate for field effect transistor applications with an on/off ratio exceeding 108 and high mobility[75–79]. For a MoS_2 transistor, by improving sample quality, removing absorbates, and depositing atop a high-dielectric layer, extrinsic scatters such as charged impurities and grain boundaries can be partially suppressed. The room temperature carrier mobility can be

improved significantly[80–85]. which is close to theoretically predicted phonon-limited intrinsic values[86, 87]. Using multi-terminal transport measurement, a record-high Hall mobility reaching 34000 $\mathrm{cm}^2/\mathrm{Vs}$ for six-layer MoS_2 at low temperature was observed[88]. The growth of MoS_2 on insulating substrates makes it to be promising for fabrication of atomically thin high performance electronic and optoelectronic devices without film transfer. This technique can be used for fabrication of vertically stacked transistors for the future three-dimensional (3-d) integrated circuits (ICs)[89].

Unlike the single MoS_2 transistor device, for MoS_2 based ICs, due to the larger number of transistors or higher functional density, heat dissipation will become a crucial issue[55]. Owing to the atomic thickness of MoS_2, the localized Joule heating can reduce device reliability and performance. The common way for heat transfer is lattice thermal conduction. The heat flux flowing through a system can be described by Fourier's law: $j = -\kappa\nabla T$, where J is the heat flux density in the system, ∇T is the temperature gradient, and κ is the thermal conductivity. For materials such as graphene[90–93], high in-plane thermal conductivity can help dissipate waste heat efficiently. However, the experimental[94–96] and theoretical studies[97–101] reveal that thermal conductivity of monolayer MoS_2 is less than $20\mathrm{W}/(\mathrm{mK})$, which is two orders of magnitude lower than that in graphene. Obviously, there is a problem with using MoS_2 in future ICs, because of its low thermal conductivity and the induced challenge in thermal management. A different cooling strategy for MoS_2 based device is really needed.

In addition to lattice thermal conduction, heat also can be transferred by radiation. The RHT is caused by transportation of electromagnetic wave. But, in far-field region, RHT between two bodies is limited by the Stefan-Boltzman law (Planck's blackbody limit). Comparing with heat conduction, RHT is always ignored in traditional thermal management for ICs. But, RHT can be enhanced by various methods, including using thermal extraction device[102] or NFRHT[28–30, 103, 104], Due to the several orders of enhancement by large density of evanescent modes[6, 8, 34, 104], NFRHT can become a promised way in controlling heat transfer in thermal rectifiers[105], thermal transistor[13], and noncontact cooling[106].

In this Chapter, using the formalism of fluctuation electrodynamics[24, 25], we explored the NFRHT from a monolayer MoS_2 sheet to graphene with short MoS_2-graphene distance (less than 100 nm). According to Wien's law, the peak wavelength λ_{max} is given by: $\lambda_{max} = b/T$, where b is the Wien's displacement constant. The thermal wavelength is 5-10 $\mu\mathrm{m}$ within the considered range of temperature (300-600 K). Therefore, Stefan-Boltzmann law does not hold and NFRHT will play the dominated role. Considering the low in-plane thermal conductivity in MoS_2 and the significantly enhanced NFRHT, for micrometer scaled MoS_2 transistor, the heat channeled by radiation can exceed that by the in-plane lattice thermal conduction. Based on these theoretical results, a distinctive thermal management strategy for MoS_2 ICs is proposed.

3.2 Near-field radiative heat transfer between two suspended plane

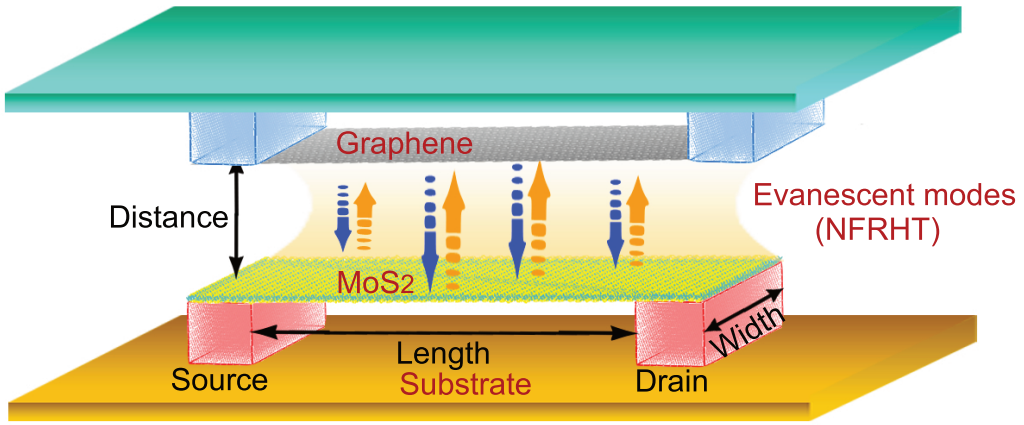

Fig. 3.1: Schematic of our simulation model: one MoS_2 sheet and one graphene sheet are brought into close proximity with a vacuum gap separation d. The temperature of MoS_2 is higher than that of graphene.

We first consider the configuration in Fig. (3.1), where one MoS_2 sheet and one graphene sheet are brought into close proximity with a vacuum gap separation d. The temperature of MoS_2 (graphene) is $T_1(T_2)$. To control optical conductivity of each sheet,

we assume they are connected to external gate electrodes. When electrical current flows through MoS_2, the Joule heating increases the temperature of MoS_2 sheet and leads to NFRHT from MoS_2 to graphene.

In principle, the heat energy transfer between two objects can be described by the electromagnetic flux resulting from fluctuating current sources inside each object: thermal fluctuations in the first object (high temperature) induce correlations between electric currents, which are related to the real part of its conductivity; next, the fluctuating currents in the first object induce electromagnetic fields in the second object (low temperature); then, the heat energy transfer is realized by the Poynting flux around the second object. Under steady state, the heat transfer from object-1 to object-2 is higher than heat transfer along the opposite direction and results in a net heat flow from high temperature object to low temperature object. The total RHT between two objects is given by:

$$H = \int_0^\infty \frac{d\omega}{2\pi}[\Theta_1(\omega, T_1) - \Theta_2(\omega, T_2)] \cdot (f_{far} + f_{near}) \tag{3.1}$$

Where $\Theta(\omega, T) = \hbar\omega/(e^{\hbar\omega/k_B T} - 1)$ is the average energy of photons. The spectral transfer function f_{far} (f_{near}) describes the contribution of far-field (near-field) radiation. For two semi-infinite nonmagnetic planes, f_{far} (f_{near}) is presented as[30, 107]:

$$\begin{aligned} f_{far} =& \int_{q<\omega/c} \frac{dq^2}{(2\pi)^2} \frac{[1 - |r_{1p}(q,\omega)|^2] \cdot [1 - |r_{2p}(q,\omega)|^2]}{|1 - e^{2i\gamma d} r_{1p}(q,\omega) r_{2p}(q,\omega)|^2}, \\ f_{near} =& 4\int_{q>\omega/c} \frac{dq^2}{(2\pi)^2} e^{-2|\gamma|d} \frac{\mathrm{Im} r_{1p}(q,\omega) \mathrm{Im} r_{2p}(q,\omega)}{|1 - e^{-2|\gamma|d} r_{1p}(q,\omega) r_{2p}(q,\omega)|^2}. \end{aligned} \tag{3.2}$$

Where $r_{1(2)}$ is the reflection coefficient of different layers, q is the wave vector, $\gamma = \sqrt{\omega^2/c^2 - q^2}$ is z component of the wave vector, d is the distance of vacuum gap, and p means p-polarized modes. In Eq. (3.1), the spectral transfer function T_{far} (T_{near}) describes the contribution of far-field (near-field) radiation by considering the nonlocal optical effects. For two semi-infinite planes, which are separated by vacuum, the RHT can be calculated from the Green's functions as Fourier integrals along the transverse coordinates (x, y). In z component (perpendicular with plane), we can mathematically

find spectral transfer function (T_{near}).

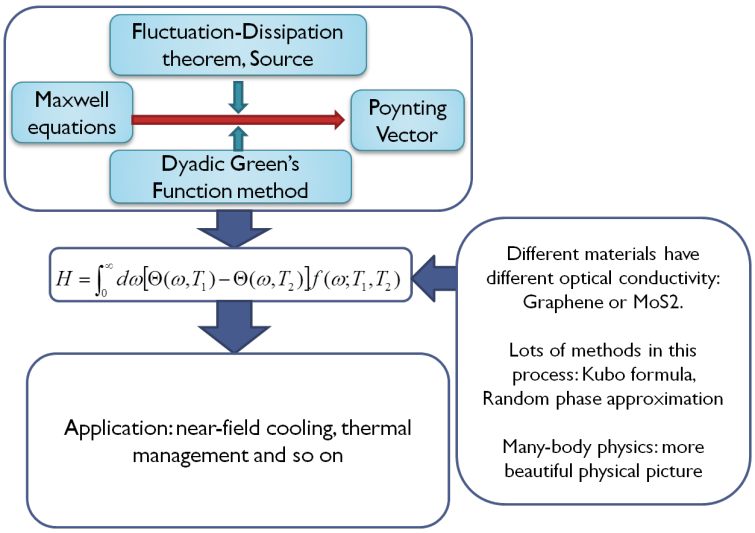

Fig. 3.2: Schematic calculation process for near-field radiative heat transfer based on the fluctuation electrodanamics.

It is necessary to justify the applicability of Eq. (3.1) in studying near-field radiation between ultra-thin 2-d materials. Based on fluctuation electrodynamics, the optical conductivity $\sigma(x, y, z)$ of a semi-infinite plane is used to study the near-field radiation. To study 2-d material in x-y plane with optical conductivity of $\sigma(x, y)$, the form of optical conductivity can be changed to $\sigma(x, y)\delta(z)$. This describes the surface of a semi-infinite plane by surface optical conductivity $\sigma(x, y)$ and others are described by vacuum. Thus the system is equivalent to a 2-d material. With this treatment, Ilic et al. have justified the applicability of equation(3.1) in studying NFRHT between graphene and semi-infinite plane. In 1999, in an independent work, Pendry also demonstrated the equation for p-polarized NFRHT between two flat surfaces is the same as Eq. (3.1). Actually, Eq. (3.1) has been used to study NFRHT between two graphene sheets. A more general consideration is given by reference[107]. Therefore, it is clear that equation is applicable in studying near-field radiation between two 2-d sheets. Besides, in our calculation, electron tunneling[108] and acoustic phonon tunneling[109] are not contained

due to large distance (more than 10 nm) between MoS_2 and graphene considered here.

3.3 Optical conductivity of graphene and MoS_2

3.3.1 Optical conductivity of graphene

From Eq. (3.2), we need get the reflection coefficient $r_{1(2)}$ to calculate the RHT. In our calculation, the reflection coefficient $r_{1(2)}$ equals to $(1-\epsilon)/\epsilon$[8, 110]. Here $\epsilon = 1+\gamma\sigma/(2\epsilon_0\omega)$ is the dielectric function of different layers, σ is the optical conductivity of the layers. We get that reflection coefficient depends on optical conductivity of different materials, which can be divided into intra-band and inter-band parts. The intra-band term can be described by the Drude model, which is the response for intra-band processes at frequencies that are well below the band gap; and the inter-band term describes excitation process with photon frequencies above the band gap. In our calculation, in the limit of high carrier concentration, optical conductivity of Graphene is presented as[111, 112]:

$$\begin{aligned}
\sigma =& \sigma_{intra} + \sigma_{inter}, \\
\sigma_{intra} =& \frac{i}{\omega + i/\tau}\frac{e^2 2k_B T}{\pi\hbar^2}\mathrm{In}\left[2\cosh\frac{\mu}{2k_B T}\right], \\
\sigma_{inter} =& \frac{e^2}{4\hbar}\left[G(\frac{\hbar\omega}{2}) + i\frac{4\hbar\omega}{\pi}\int_0^\infty \frac{G(\xi)-G(\hbar\omega/2)}{(\hbar\omega)^2-4\xi^2}d\xi\right], \\
G(\xi) =& \sinh(\xi/k_B T)/[\cosh(\mu/k_B T)+\cosh(\xi/k_B T)].
\end{aligned} \tag{3.3}$$

Where μ is chemical potential of graphene, $\tau \approx 10^{-13}s$ is the relaxation time which describes the scattering process of graphene and is assumed that it is not varied with temperature (at room temperature region).

3.3.2 Optical conductivity of MoS_2

Different from graphene, MoS_2 has in-equivalent $K(K')$ points in Brillouin zone due to the lack of inversion symmetry. The calculation about optical property of MoS_2 is based

on the below modified Hamiltonian[113]:

$$H = \frac{\Delta}{2}\sigma_z + \lambda\tau s\frac{1-\sigma_z}{2} + t_0 a_0 \mathbf{q}\cdot\sigma_\tau + \frac{\hbar^2|\mathbf{q}|^2}{4m_0}(\alpha_1 + \beta_1\sigma_z). \tag{3.4}$$

where $\sigma_\tau = (\tau\sigma_x, \sigma_y)$ is the Pauli matrices, $s(\tau) = +(-)$ for different $K(K')$ point and describe two independent spin(valley) in the first Brillouin zone, a_0 is lattice constant, m_0 is free electron mass, α_1 and β_1 are high order parameters which are connected with electron or hole effective mass. The intrinsic optical conductivity of MoS_2 also contains two parts: intra-band part and inter-band part. For inter-band part of MoS_2, the calculation starts from the modified Hamiltonian of MoS_2 and use the Kubo formula to calculate the inter-band optical properties[114]. On the other side, the intra-band optical conductivity is calculated by the general formula in the limit of high carrier concentration[111]:

$$\sigma_{\alpha\beta}^{intra}(\omega) = \frac{e}{\pi^2}\int \frac{d^2p v_\alpha v_\beta}{i\omega - \tau^{-1}}\frac{df[\epsilon(p)]}{d\epsilon} \tag{3.5}$$

Where p is the wave vector, $v_{\alpha(\beta)}$ is the group velocity of electron in conduction band, α and β are the indices, f is the Fermi Dirac distribution function. In our numerical calculation, the parameters are taken from first-principle calculation to describe properties of MoS_2[113, 114]. For intraband part, we take the relaxation time data from Cai et al.[97], where τ equals to 1.889×10^{14} s for electron doping case of MoS_2. The adopted parameters for calculation of optical conductivity of MoS_2 are summerized in Table. (3.1).

Δ (eV)	λ (eV)	t_0 (eV)	α_1	β_1
1.9	0.08	1.68	0.43	2.21

Table 3.1: Numerical parameters for monolayer MoS_2

3.4 Results and discussion

The tunable spectral transfer function of NFRHT for different cases is shown in Fig. (3.3). Graphene is a gapless semimetal with Dirac cone structure, and MoS_2 is a direct band

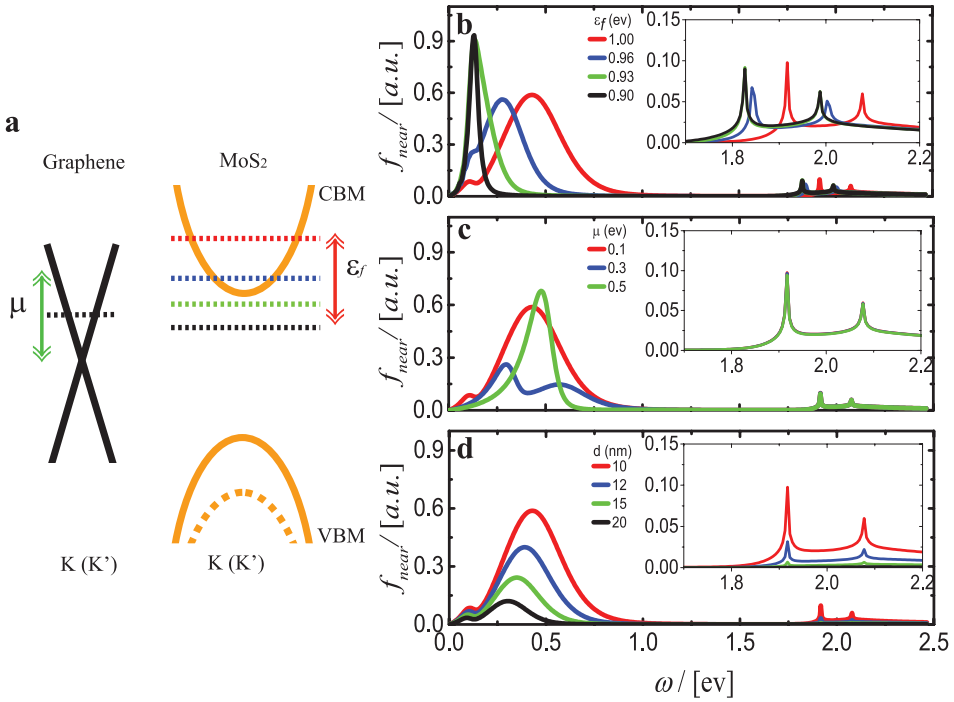

Fig. 3.3: (a) Band shift diagram. (b) Spectral transfer function with different Fermi energy of MoS_2. Distance is 10 nm, and chemical potential of graphene is fixed as 0.1eV. (c) Spectral transfer function with different chemical potential of graphene. Fermi energy of MoS_2 is set as 1.0 eV for electron doping case. (d) Spectral transfer function with different distances between MoS_2 and graphene. A fixed 300 K temperature is applied to both MoS_2 and graphene in all three figures.

gap semiconductor (Fig. (3.3a)). First, we fix the chemical potential of graphene and tune the Fermi energy of MoS_2. Due to the large band gap and spin-orbit coupling in MoS_2, the inter-band transition processes of MoS_2 are the dominant channels at visible light frequency region and split into two small peaks. As shown in the inset of Fig. (3.3b), the inter-band transition peaks can be adjusted by the Fermi energy of MoS_2 (ϵ_f) and there is obvious blue shift when ϵ_f increases, which agrees well with the previous reports[114]. However, the strength of T_{near} at high frequency region (1.5-2.5 eV) is much lower than that at low frequency region ($x < 1.0\mathrm{eV}$) due to the poor absorbing ability of graphene in visible light frequency region. That means intra-band transition of MoS_2 (Drude process) dominates T_{near} in low frequency region. The central frequency of peak (below 1 eV region) has red shifts with the decrease of Fermi energy of MoS_2. At $\epsilon_f = 0.93\mathrm{eV}$, the Fermi energy of MoS_2 is close to its conduction band edge, thus leading to sharp resonant peak. This low frequency resonant peak provides main channel

for NFRHT.

Fig. (3.3c) shows that spectral transfer function can be tuned by the chemical potential of graphene. But, comparing with Fig. (3.3b), Fig. (3.3c) provides more interesting physical processes: the competition between inter-band and intra-band transition in graphene. Due to the gapless of graphene, inter-band transition plays important role in 2μ (μ is the chemical potential) frequency region. When μ is small, the intra-band and inter-band peaks in graphene are coincident due to the thermal broaden. With the increase in chemical potential ($\mu = 0.3\mathrm{eV}$), two kinds of peaks are separated and form different channels with MoS_2 (Blue line in Fig. (3.3c)). The results in Fig. (3.3c) can provide the optimized chemical potential and Fermi energy, and that is useful for taking advantage of NFRHT.

In addition to the chemical potential and Fermi level in graphene and MoS_2, it is obvious that the spectral transfer function should depend on the graphene-MoS_2 gap. Fig. (3.3d) shows T_{near} as function of frequency, with graphene-MoS_2 gap changed from 10 to 20 nm. Although the spectral transfer function curves have the common feature of frequency dependence, there is considerable blue shift when graphene-MoS_2 gap decreases, accompanied with remarkable increase in the strength. When gap decreases from 20 to 10 nm, the strength of T_{near} increases 5 times, showing strong distance dependent NFRHT.

NFRHT between MoS_2 and graphene is quantitatively investigated as a function of distance in Fig. (3.4a) and normalized with blackbody limit. For the resonant case (black line in Fig. (3.3)a : $\mu = 0.1\mathrm{eV}$, $\epsilon_f = 0.9\mathrm{eV}$), three orders of heat enhancements in NFRHT comparing with blackbody limit is realized, and this ratio increases quickly with the vacuum gap decreasing. For example, at small vacuum gap of 10 nm, the heat transfer channeled by near-field radiation is 4×10^3 times of blackbody radiation limit. However, the NFRHT is very sensitive to the chemical potential and Fermi energy of graphene and MoS_2. With slight deviation from the ideal resonant state, the heat transfer decreases significantly, such as from $30 \times 10^3\ \mathrm{kW/m^2}$ to $5 \times 10^3\ \mathrm{kW/m^2}$ with only 0.1 eV change in ϵ_f.

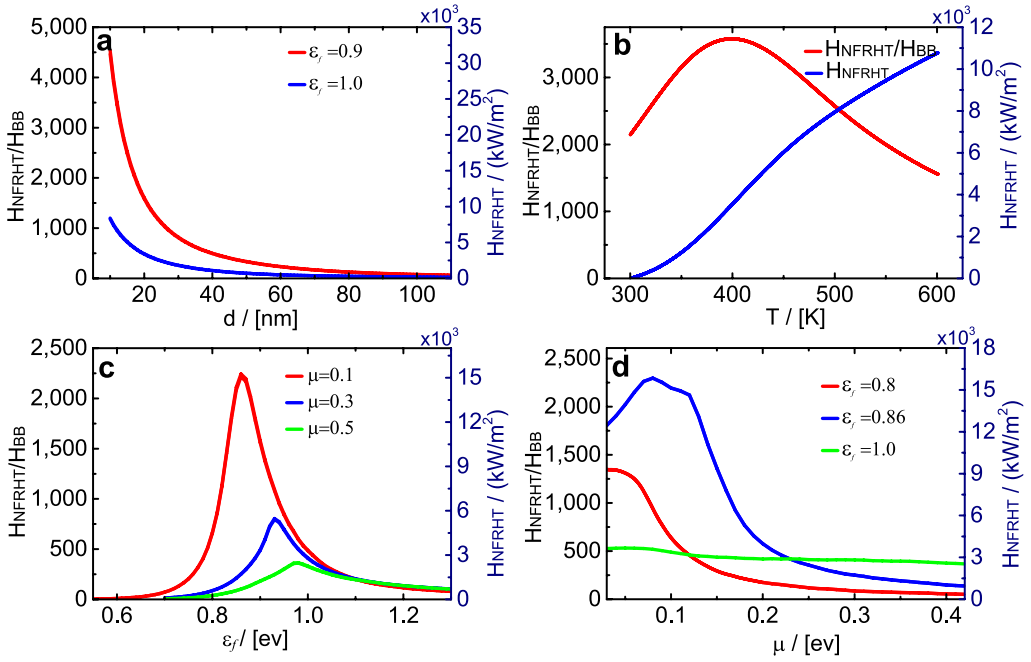

Fig. 3.4: (a) NFRHT as a function of distance between MoS_2 and graphene. Chemical potential of graphene is set as 0.1 eV. Temperature of MoS_2 is 600 K. (b) NFRHT as a function of temperature of MoS_2 sheet. Chemical potential of graphene is 0.1 eV, and Fermi energy of MoS_2 is 0.9 eV. Distance is 20 nm. (c) NFRHT as a function of Fermi energy of MoS_2. Temperature of MoS_2 is 600 K and Distance is 20 nm. (d) NFRHT as a function of chemical potential of graphene. Temperature of MoS_2 is 600 K and Distance is 20 nm. The temperature of graphene is fixed at 300 K.

The ratio between NFRHT and Blackbody limit as a function of temperature of MoS_2 sheet is shown in Fig. (3.4b). It is interesting to find that NFRHT increases almost linearly with the temperature difference between two layers, while heat transfer by blackbody limit grows with T^4. Thus, the ratio of HNFRHT over HBB increases with temperature of MoS_2 sheet, achieves maximum value, and then decreases. In the considered temperature range, heat transfer by near-field radiation keeps thousands times higher than the Blackbody limit, demonstrating the importance of near-field radiation in thermal management of nanoscale devices.

Fig. (3.4c) quantitatively indicates the NFRHT as function of ϵ_f with different chemical potential of graphene. There is an optimal Fermi energy of MoS_2 yielding the maximum attainable value of HNFRHT. When Fermi energy of MoS_2 is close to its conduction band edge, MoS_2 can support Surface Plasmon-polaritons (SPPs) and form resonant channels with graphene to enhance NFRHT. Fig. (3.5) shows that there is strong SPPs peak under resonant cases. Moreover, maximum HNFRHT depends on the

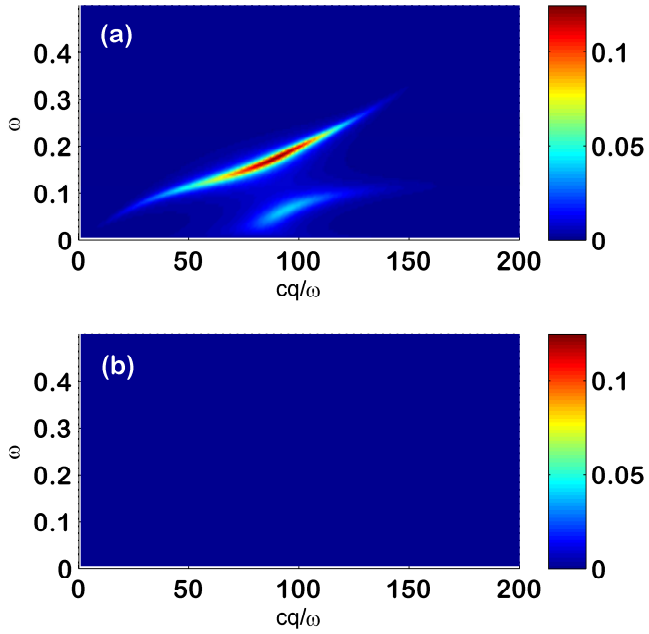

Fig. 3.5: Transmission probabilities of energy carried by modes. (a) Resonant case between MoS_2 and graphene, i.e. Chemical potential of graphene is set as 0.1 eV and $\epsilon_f = 0.9$ eV. (b) Non-resonant case between MoS_2 and graphene, i.e. Chemical potential of graphene is set as 0.1 eV and $\epsilon_f = 0.7$ eV .Temperature of MoS_2 is 600 K and Distance is 20 nm. The temperature of graphene is fixed at 300 K.

choice of chemical potential of graphene. When $\mu = 0.1\mathrm{eV}$, the resonant matching of spectral transfer function significantly enhances the NFRHT. As the chemical potential of graphene changes from 0.1 eV, the plasmons in the graphene and MoS_2 sheets move out of resonance and the heat transfer decreases. The maximum heat transfer by near-field radiation reduces from 15×10^3 $\mathrm{kW/m^2}$ to about 2×10^3 $\mathrm{kW/m^2}$ with chemical potential changes 0.4 eV. Thus, in the application for thermal management, accurate controlling of chemical potential of the low temperature sheet is critical to obtain high heat transfer efficiency. However, Fig. (3.4d) shows that the NFRHT has quite different dependences on μ with varied ϵ_f. When $\epsilon_f = 0.86\mathrm{eV}$ (at the resonance state), NFRHT shows highly tunable properties for different values of μ. When μ increases from 0.1 to 0.4 eV, the HNFRHT decreases with about 14.5×10^3 $\mathrm{kW/m^2}$. In contrast, the HNFRHT versus I curve is almost flat when $\epsilon_f = 1.0\mathrm{eV}$. In this case, the Fermi energy of MoS_2 is shifted away from conduction band edge and SPPs modes in MoS_2 are suppressed. The channels of NFRHT are closed and almost independent with chemical

potential of graphene. Combining the results in Figures (3.4c) and (3.4d), it is clearly shown that the controlling of Fermi energy of MoS_2 sheet is more critical to achieve high energy transfer efficiency in the NFRHT between MoS_2 and graphene sheets.

The improvement of NFRHT provides promising application in thermal management of MoS_2 based electronic and optoelectronic devices. Finally, we discuss the cooling process by NFRHT and compare with the in-plane lattice thermal transport. We consider a MoS_2 sheet that width is 1 $\mu\mathrm{m}$, and the length is varied from 0.5 to 3.5 $\mu\mathrm{m}$. Heat is generated by Joule heating effect and leads to temperature increasing of MoS_2 sheet. So, we assume the temperature of its middle part is 600 K, while the two ends are at a constant temperature of 300 K. According to Fourier's law, there is heat current flow from the middle part to two ends. At steady state, the temperature decreases linearly from middle part to the two ends and heat current can be obtained from the temperature gradient and thermal conductivity. This is heat energy transfer by in-plane lattice thermal conduction. To study the NFRHT, a graphene sheet is placed parallel to MoS_2 sheet, with distance to MoS_2 sheet (varied from 10 to 20 nm). In our calculation, we divided the MoS_2 sheet into different slices along heat current direction (as shown in Fig. (3.6a)), and temperature in each slice is assumed to be constant. We also assume that only the parts which are directly opposite to each other are contributed to the RHT. Then, NFRHT from each slice to the faced graphene section is calculated from fluctuation electrodynamics. Besides, we also do not consider the size effects of surface plamsons.

The thermal conductivity of monolayer MoS_2 is obviously lower than that of graphene; however, there is discrepancy in reported values from different experimental and theoretical works, which is varied from several $\mathrm{W/mK}$ to tens $\mathrm{W/mK}$[86, 94–96, 98–101]. First, we select thermal conductivity of monolayer MoS_2 as 30 $\mathrm{W/mK}$. Solid lines in Fig. (3.6b) show the ratio between NFRHT and in-plane thermal conduction. It is interesting to find that ratio increases quickly when length increases. Although, as commonly expected, RHT is lower than in-plane thermal conduction for short MoS_2 sheet, it exceeds the later one for MoS_2 longer than 2.7 $\mu\mathrm{m}$, with MoS_2-graphene gap

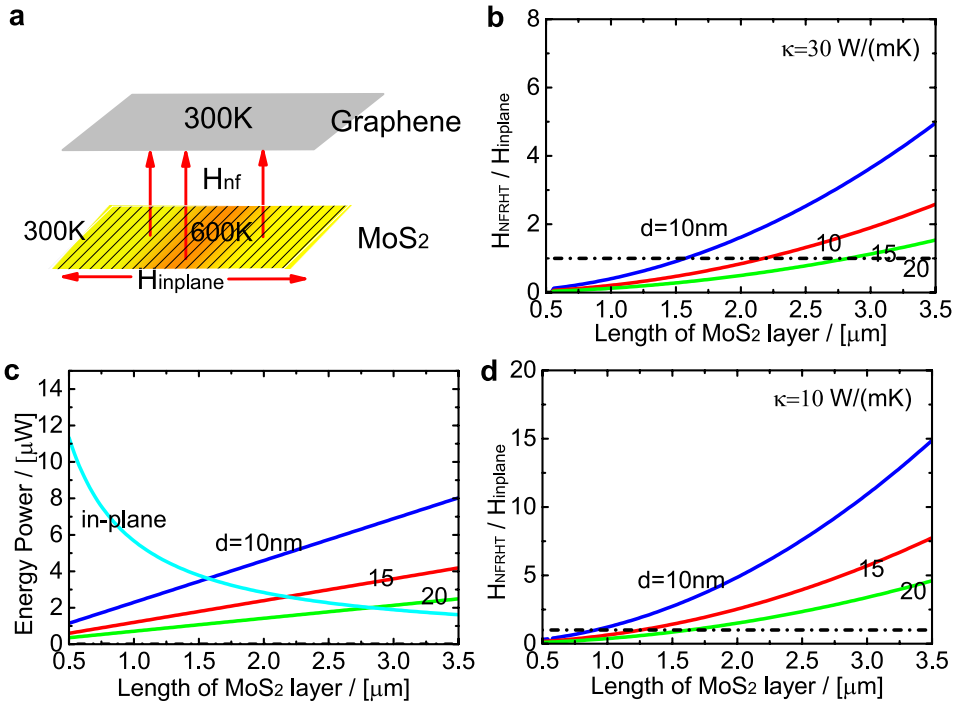

Fig. 3.6: (a) Temperature distribution of NFRHT based cooling device. (b) Ratio of NFRHT and in-plane heat conduction as a function of length of MoS_2 when the thermal conductivity of MoS_2 is 30 $\mathrm{W/mK}$. (c) Energy power of NFRHT and in-plane heat conduction as a function of length of MoS_2. (d) Ratio of NFRHT and in-plane heat conduction as a function of length of MoS_2 when the thermal conductivity of MoS_2 is 10 $\mathrm{W/mK}$. In (b)-(d), Fermi energy of MoS_2 is 0.9 eV and chemical potential of graphene is 0.1 eV. Width of MoS_2 and graphene sheet is 1 $\mu\mathrm{m}$.

$d = 20$ nm. This unexpected phenomenon can be understood from the different size dependences for these two heat transfer mechanisms, which are showed in Fig. (3.6c): energy power of in- plane lattice heat conduction decays fast with increasing length of MoS_2, but energy power of NFRHT almost linearly increases with increasing length of MoS_2. In lattice thermal conduction, when device length increases, the temperature gradient along heat flux direction decreases if the temperature difference between the two ends is constant. This leads to reduction in the total heat current. On the other side, for NFRHT, the total heat energy transfer increases with the increase in sample size. Thus, there is one critical sample length beyond which RHT is higher than the in-plane heat energy conduction. When MoS_2-graphene gap $d = 20$ nm, this critical length is about 2.7 μm, in the range of real MoS_2 devices. Moreover, this critical length decreases with MoS_2-graphene gap decreases. For $d = 10$ nm, for short-channel

MoS_2 device with length less than 1.5 μm, the importance of RHT is appeared. The heat energy transferred by near-field radiation is 5-times of that by the in-plane thermal conduction when length of MoS_2 sheet is 3.5 μm. Considering that the length range of real MoS_2 field-effect-transistor is about 10 μm[75–80, 83], the NFRHT should play dominated role in thermal management of MoS_2 based ICs. As the in-plane heat current is proportional to the value of thermal conductivity, while NFRHT is independent on this material property, the importance of NFRHT is expected to be more significant with the decrease in thermal conductivity. Our numerical results adopting lower values of thermal conductivity are shown in Fig. (3.6d). If various external scattering sources existed to reduce thermal conductivity of MoS_2 sheet to 10 K, with $d = 10$ nm and $L = 3$ μm, the heat energy carried by near-field radiation is one order of magnitude higher than that by lattice thermal conduction, which provides an important cooling strategy for this type of nanoscale devices.

3.5 Summary

In summary, we have numerically studied the NFRHT between MoS_2 and graphene. It is found that the heat transfer by near-field radiation can be controlled by the chemical potential of graphene and the Fermi energy of MoS_2. By appropriately tuning the chemical potential of graphene and Fermi energy of MoS_2, surface plasmon-polaritons form low frequency resonant peaks in spectral transfer function and provide dominated channels for NFRHT. Under resonance, the heat energy transfer via near-field radiation from monolayer MoS_2 to graphene can be several orders of magnitude higher than the Blackbody limit. Due to this large enhancement and low thermal conductivity of monolayer MoS_2, NFRHT can be ten times higher than in-plane lattice thermal conduction. Our work provides a theoretical support for designing strategy for thermal management of future MoS_2 based highly integrated electronic and optoelectronic devices.

Chapter 4

Capacitor physics in ultra-near-field heat transfer

"Science is organized knowledge.
Wisdom is organized life."
—Immanuel Kant

4.1 Introduction

Historically, the studied for blackbody radiation deposits the foundation for radiative heat transfer(RHT)[115]. In fact, Planck's blackbody theory [1] is not valid when distances between objects are comparable to the thermal wavelength, i.e., on the order of micrometers at room temperature. In the early 1970s, scientists started to pay attention to this problem qualitatively. Rytov[116] developed a general theory in the 1950s, known as FE. Then Polder and von Hove (PvH) gave the first formula for the RHT with a parallel-plate configuration[28, 117], which assumes a Landauer form in the parlance of mesoscopic transport theory[107]. In that calculation, the electromagnetic wave is treated through Maxwell's equations. And the quantum effects are only considered in the quantum version of the fluctuation-dissipation theorem. Later, FE method has been applied to study the RHT in other symmetric configurations, such as sphere-plate[2], cylinder-plate[3], as well as one-dimensional gratings[4]. Under the context of pho-

tonic thermal management, the NFRHT[118, 119] between different 2-d materials are studied[6, 120, 121], while novel concepts are frequently proposed, e.g. vacuum thermal rectifier[105], near-field thermal transistor[13] and radiative thermal memory device[15]. Recently, precision measurements of RHT in nanoscale gaps were achieved in different materials with plane-plane or tip-plane configurations[7, 9, 40, 104, 122]. As a whole, sixty years after its birth, fluctuation electrodynamics continues to stimulate interests across a broad spectrum of the scientific community.

Except for a few works[123–126], the quantity of interest for RHT has always concentrated on the calculation of electromagnetic energy flux density, i.e., the Poynting vector[6, 120, 121]. Further, one regularly holds current or polarization density as the only fluctuating source responsible for RHT[2–4, 30, 127]. While FE method has been very successful, some questions persist: down to which length scale does a semiclassical theory as such remain valid? Is current fluctuation the only mechanism to be accounted for in electromagnetic heat transfer? Such are the issues we want to address in this Chapter. Based on a double quantum dots model, we give a detailed account of the fully quantum-mechanical treatment of thermal radiation proposed in a recently submitted paper[128]. We focus on the scalar field, which was initially thought to be for the sake of simplicity. However, ignoring the vector potential $\boldsymbol{A}$[129] (which arises from current fluctuation) reveals that charge fluctuation (to which is associated the scalar potential) plays an equally if not more important role in the RHT within short distances. In particular, we identify a length scale much smaller than the thermal wavelength at room temperature.

From a methodological perspective, the calculation of RHT can be explained as an open system. Since in steady state, we need a source capable of supplying energy for an indefinite amount of time. For two bodies placed extremely close to each other ($<$10 nm), which is now experimentally possible[7, 9, 40, 104, 122], a fully-quantum description is required. In this respect, NEGF is the usual choice of method. It has been used to study quantum thermal transport of electrons and phonons [64, 71, 130–132], and we wish to extend this method to the case of photon-mediated thermal transport.

Importantly, we go beyond the ballistic treatment and consider the nonlinear interactions between the scalar field and the electrons.

This Chapter is formed as follows. We begin with a constructing two-dot capacitor model in section (4.2), where we also write down the Hamiltonian, discuss the quantization of electrodynamics and the inverted harmonic oscillator. In section (4.3), we outline the NEGF methods, solve the Dyson equation and present the Keldysh equation. In section (4.4), we quantize a "Poynting scalar" (heat flux due to the Coulomb interaction) and relate its expectation value to a Green's function. In section (4.4.2), we analyze the current expression under different limiting procedures to represent a physical picture from our simple model. In section (4.5), we take the problem of self-energy calculations. Three approximations are discussed, putting into perspective Rytov's theory and our NEGF approach. In section (4.6), numerical simulations of our theory are given, allowing us to investigate two-dot transport behaviors. We conclude and summarize in section (4.7).

4.2 Model construction

In this section, we deal exclusively with a one-dimensional field. By one dimension, we do not mean that our physical system is a one-dimensional line. Instead, we assume the fields (the scalar potential, or the electric field) which live in a three-dimensional space, depend only on one single variable z. Thus, a three-dimensional parallel plate with sufficiently large cross-sectional area A belongs to a one-dimensional problem.

4.2.1 The Lagrangian of model

We fist consider nanoscale parallel plates with a possible charge of either 0 or $-Q$ as shown in Fig. (4.1) and small cross area A. We regard this system as two quantum dots mathematically. It is like a mean-field approximation because we ignore the electron-electron interaction in the nanoscale plate. To each dot is connected a reservoir, allowing its charge to fluctuate and generate radiation. This simple model allows for analytically tractable expressions, all the while providing an essential ingredient for radiative heat

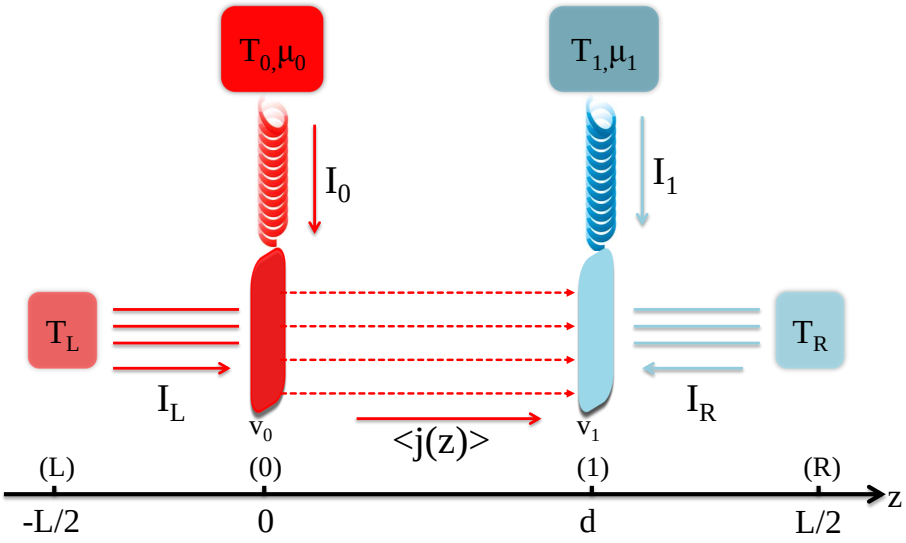

Fig. 4.1: Schematic of the two-dot capacitor model. Scalar photons permeate the space, with T_L and T_R indicating the photon bath temperatures. Electrons of onsite energies v_0 and v_1 are located at $z_0 = 0$ and $z_1 = d$, connected to fermionic reservoirs at temperatures and chemical potentials (T_0, μ_0) and (T_1, μ_1) respectively.

transfer: two separated systems connected to two baths. We postulate the Lagrangian as $L = L_e + L_\gamma + L_{\rm int}$, with

$$\begin{aligned} L_e =& \sum_{j=0,1} c_j^\dagger (i\hbar \dot{c}_j - v_j c_j) + \sum_{j=0,1} \sum_{k\in \text{bath}} d_{jk}^\dagger (i\hbar \dot{d}_{jk} - \epsilon_{jk} d_{jk}) \\ & - \sum_{j=0,1} \sum_{k\in \text{bath}} \left(V_{jk} c_j^\dagger d_{jk} + \text{H.c.} \right), \\ L_\gamma =& s \int dz \left[-\frac{1}{2}\dot{\phi}^2 + \frac{c^2}{2} \left(\frac{\partial \phi}{\partial z} \right)^2 \right], \\ L_{\rm int} =& - \sum_{j=0,1} (-Q) c_j^\dagger c_j \phi(z_j). \end{aligned} \tag{4.1}$$

Here we assume a tight-binding model for the electrons represented by fermionic annihilation operators c_j and creation operators $c_j^\dagger$. The electrons are located at positions z_j with $z_0 = 0$ and $z_1 = d$. The onsite energy of dot j is v_j. The electrons themselves at different sites do not have direct hopping coupling but the electrons are coupled to their

respective baths. Electron bath j is described by fermionic operators $d_{jk}^{\dagger}$ with energy ϵ_{jk} and is coupled to dot j via a tunneling amplitude V_{jk}, where k's are the reservoir modes. For the field $\phi(z,t)$, we have defined the scale factor $s = \epsilon_0 A/c^2$, where ϵ_0 is the vacuum permittivity, A is the cross-sectional area of the plates, c is the speed of light, and the integral extends from $-\infty$ to ∞. We split this integral into three parts, $(-\infty, -L/2]$, $[-L/2, L/2]$, and $[L/2, +\infty)$, and consider them to be the left photon bath, central region, and right photon bath.

The most striking feature of the Lagrangian is the scalar field part. Since we can split the Lagrangian as $L = T - V$, the kinetic energy minus the potential energy, we see that the Lagrangian for the field has both a negative kinetic energy and a negative potential energy. This is the correct Lagrangian to use since it gives the wave equation with the charge as the source from the principle of least action ($\delta \int (\mathcal{L}_\gamma + \mathcal{L}_{int}) dt = 0$)[133, 134],

$$\frac{1}{c^2}\ddot{\phi} - \frac{\partial^2 \phi}{\partial z^2} = \frac{\rho}{\epsilon_0} = \frac{1}{\epsilon_0 A}\sum_j (-Q) c_j^{\dagger} c_j \delta(z - z_j). \tag{4.2}$$

We note that in the limit $c \to \infty$, it reduces to the (one-dimensional) Poisson equation for the potential.

4.2.2 Canonical quantization and Hamiltonian

The introduction of the Lagrangian gives us a good starting point to quantize the system according to the canonical quantization scheme. We compute the conjugate momenta for the dynamical variables c_j, $c_j^{\dagger}$, and ϕ:

$$\begin{aligned} P_{c_j} &= \frac{\partial L}{\partial \dot{c}_j} = i\hbar c_j^{\dagger}, \\ P_{c_j^{\dagger}} &= \frac{\partial L}{\partial \dot{c}_j^{\dagger}} = 0, \\ \Pi_\phi(z) &= \frac{\delta \mathcal{L}}{\delta \dot{\phi}(z)} = -s\dot{\phi}(z). \end{aligned} \tag{4.3}$$

The last derivative above is a functional derivative since $\dot{\phi}(z)$ is a field that depends continuously on z.

We impose canonical commutation relations to quantize the system, turning numbers into operators. However, the fermionic degrees of freedom are already in a quantized form. More precisely, we should think of c_j and its Hermitian conjugate as Grassmann numbers obeying the anti-commutation relation, $c_j c_k^\dagger + c_k^\dagger c_j = \delta_{jk}$. For the field, we have:

$$\begin{aligned}[\phi(z), \phi(z')] &= 0, \\ [\Pi_\phi(z), \Pi_\phi(z')] &= 0, \\ [\phi(z), \Pi_\phi(z')] &= i\hbar\delta(z - z').\end{aligned} \tag{4.4}$$

Due to the negative-definite kinetic energy term, the last commutation relation, i.e. $[\dot{\phi}(z), \phi(z')] = (i\hbar/s)\delta(z - z')$, differs from the usual ones for phonons (or transverse photons) by a minus sign.

The quantum Hamiltonian is obtained from the Legendre transform $H = \sum_j (P_{c_j}\dot{c}_j + P_{c_j^\dagger}\dot{c}_j^\dagger) + \int dz\, \Pi_\phi(z)\dot{\phi}(z) - \mathcal{L}$, giving $H = H_\gamma + H_e + H_{\text{int}}$[128], with:

$$\begin{aligned}H_\gamma &= -s \int dz \frac{1}{2}\left[\dot{\phi}^2 + c^2\left(\frac{\partial\phi}{\partial z}\right)^2\right], \\ H_e &= \sum_{j=0,1} v_j c_j^\dagger c_j + \sum_{j=0,1}\sum_{k\in\text{bath}} \epsilon_{jk} d_{jk}^\dagger d_{jk} + \sum_{j=0,1}\sum_{k\in\text{bath}} \left(V_{jk} c_j^\dagger d_{jk} + \text{H.c.}\right), \\ H_{\text{int}} &= \sum_j (-Q) c_j^\dagger c_j \phi(z_j),\end{aligned} \tag{4.5}$$

where H_γ is the free scalar photon Hamiltonian. In our model, we regard the photon field as a scalar wave propagating at the speed of light, and restrict the 3D photon field to an infinite cuboid with cross-sectional area A. From the free photon Hamiltonian, we see that the scalar field obeys a wave equation: $\frac{\partial^2\phi}{\partial z^2} - \frac{1}{c^2}\frac{\partial^2\phi}{\partial t^2} = 0$ in free space. H_{int} is the interaction between electrons and the scalar potential which assumes the form $q_j\phi(z_j)$, where the charge operator at site j is given by $q_j = (-Q)c_j^\dagger c_j$.

In above models, one question is the use of Lorenz gauge without vector potential—this seems to be incompatible with the gauge condition, $\dot{\phi}/c^2 + \boldsymbol{\nabla}\cdot\boldsymbol{A} = 0$. However, recall that we wish to focus on charge fluctuation, so we shall forego completely the

transverse[1] current $\boldsymbol{J}_\perp = \boldsymbol{0}$[2]. This way, the only part left of the vector potential $\boldsymbol{A} = \boldsymbol{A}_\perp + \boldsymbol{A}_\parallel$ is its longitudinal part $\boldsymbol{A}_\parallel$. Now, in the limit $c \to \infty$, one has $\boldsymbol{\nabla} \cdot \boldsymbol{A}_\parallel = 0$, which together with $\boldsymbol{A}_\perp = \boldsymbol{0}$ implies a vanishing $\boldsymbol{A}$. Thus it is possible to work under Lorenz gauge with a zero vector potential, provided that the current is irrotational, $\boldsymbol{\nabla} \times \boldsymbol{J} = \boldsymbol{0}$, and that we take $c \to \infty$ at the end. A finite speed c is needed for canonical quantization, for otherwise there will be no generalized velocity $\dot{\phi}$ in the Hamiltonian which will result in a vanishing conjugate momentum $\Pi_\phi = 0$. In the limit of taking $c \to \infty$, our scalar field description is completely equivalent to the Coulomb interaction[129].

4.2.3 Inverted harmonic oscillator

Another question is how to deal with a negative-definite Hamiltonian H_γ? One does not encounter this problem in the standard quantum electrodynamics[135], because the negative-definite scalar photon Hamiltonian gets canceled precisely by its longitudinal counterpart that arises from the vector potential[133, 134], resulting in a total free photon Hamiltonian that remains positive definite. Here, we circumvent this difficulty by assigning negative temperatures to the photon baths. However, in the limit $c \to \infty$, the Coulomb interaction—which does not propagate —is recovered, and the photon baths being placed at $\pm\infty$ are immaterial in actual calculations.

The photon baths can be understood as a collection of independent oscillators. Thus, it is sufficient to study a single-mode oscillator at, say, frequency $\omega_0 > 0$. However, these oscillators are inverted, with a negative kinetic energy and negative potential energy. Such model has been studied by Glauber[136] as a quantum amplifying device. Here we see it is necessary to 'build' a photon bath.

Consider thus a single-oscillator Lagrangian $\mathcal{L} = T - V = -\frac{1}{2}(\dot{u})^2 - \left(-\frac{1}{2}\omega_0^2 u^2\right)$. The conjugate momentum is $p = -\dot{u}$. This implies the canonical commutation relation is $[u, p] = [\dot{u}, u] = i\hbar$. The Hamiltonian is the negative of the usual one, $H =$

[1] For a smooth vector field $\boldsymbol{V}$ admitting Helmholtz decomposition[134], i.e. $\boldsymbol{V} = \boldsymbol{V}_\perp + \boldsymbol{V}_\parallel$, its transverse and longitudinal part satisfy respectively $\boldsymbol{\nabla} \cdot \boldsymbol{V}_\perp = 0$ and $\boldsymbol{\nabla} \times \boldsymbol{V}_\parallel = \boldsymbol{0}$.

[2] The longitudinal current $\boldsymbol{J}_\parallel$ is needed for charge continuity equation but does not appear directly in the Hamiltonian.

$p\dot{u} - \mathcal{L} = -\frac{1}{2}\left(p^2 + \omega_0^2 u^2\right)$, which is negative definite. We can introduce the creation and annihilation operators in the usual way, $u = \sqrt{\hbar/(2\omega_0)}\left(a + a^\dagger\right)$, and $-p = \dot{u} = i\sqrt{\hbar\omega_0/2}\left(-a + a^\dagger\right)$. This leads to the commutation relation:

$$[a, a^\dagger] = -1. \tag{4.6}$$

The Hamiltonian can then be written as:

$$H = -\frac{1}{2}\hbar\omega_0\left(aa^\dagger + a^\dagger a\right) = -\hbar\omega_0\left(aa^\dagger + \frac{1}{2}\right), \tag{4.7}$$

where the extra $-\hbar\omega_0/2$ is the zero-point motion energy, and $aa^\dagger$ is the number operator. Since $[H, a] = -\hbar\omega_0 a$, and $[H, a^\dagger] = \hbar\omega_0 a^\dagger$, the meaning of $a^\dagger$ (a) increasing (decreasing) the energy by $\hbar\omega_0$ remains the same as in the usual oscillator. Since the eigen-energies of the system cannot be positive, the raising operation must terminate at the zero-number state. This gives the condition $a^\dagger|0\rangle = 0$. Thus, how the eigenstates are built is now different. The eigenvalues are $E_n = -\hbar\omega_0(n + 1/2)$, $n = 0$, 1, 2, $\cdots$, with the eigenvectors $\propto a^n|0\rangle$.

We can work out the statistical mechanics of the problem. The average occupation number in a canonical ensemble is:

$$\left\langle aa^\dagger\right\rangle_H = \frac{\mathrm{Tr}\left(aa^\dagger e^{-\beta H}\right)}{\mathrm{Tr}\left(e^{-\beta H}\right)} = \frac{1}{e^{-\beta\hbar\omega_0} - 1} \equiv N_{-\beta}(\omega_0). \tag{4.8}$$

In deriving the above, one encounters a geometric series in $e^{\beta\hbar\omega_0}$, which, for $\omega_0 > 0$, converges only if $\beta < 0$. Thus, we see that the partition function is defined only for $\beta < 0$, i.e. statistical mechanics demands that scalar photon baths yield negative absolute temperature. Also, $\left\langle a^\dagger a\right\rangle_H = \left\langle aa^\dagger\right\rangle_H + 1 = -N_\beta(\omega_0)$. One can check that the fluctuation-dissipation theorem holds in the usual way,

$$\begin{aligned} D^<(\omega) &= N_\beta(\omega)\big(D^r(\omega) - D^a(\omega)\big), \\ D^>(\omega) &= \big(N_\beta(\omega) + 1\big)\big(D^r(\omega) - D^a(\omega)\big), \end{aligned} \tag{4.9}$$

where the Green's functions are defined in the variable u according to the usual convention[64, 71].

4.3 NEGF, Dyson equation and Keldysh equation

4.3.1 NEGF and Dyson equation

In Rytov's theory[116], one focuses on the electromagnetic fields due to fluctuating sources whose autocorrelation function is given phenomenologically. On the other hand, NEGF focuses on correlation functions and allows fields, matter and their interaction to be studied altogether. As discussed below, the two approaches are equivalent under the local equilibrium approximation. However, NEGF can handle electron-photon interactions in a perturbative way or through mean-field schemes such as the self-consistent Born approximation. Thus, NEGF is a more general and more powerful method.

In the formalism of NEGF, we define the contour-ordered Green's function for photons[41, 64, 71]:

$$\begin{aligned} D(z,\tau;z',\tau') &= \frac{1}{i\hbar}\langle T_\tau \Delta\phi^H(z,\tau)\Delta\phi^H(z',\tau')\rangle_H \\ &= \frac{1}{i\hbar}\langle T_\tau \Delta\phi(z,\tau)\Delta\phi(z',\tau')e^{-\frac{i}{\hbar}\int H_{\rm int}(\tau'')d\tau''}\rangle_{H_\gamma+H_e}, \end{aligned} \tag{4.10}$$

where the first line is in the Heisenberg picture with time evolution according to the total Hamiltonian H, while on the second line, we have transformed the variables into the interaction picture. The interaction Hamiltonian is

$$H_{\rm int}(\tau) = \sum_j (-Q)c_j^\dagger(\tilde{\tau})c_j(\tau)\phi(z_j,\tau). \tag{4.11}$$

Above, τ and τ' are Keldysh contour times. $\tilde{\tau} = \tau + \Delta\tau$. Under T_τ, i.e., the contour-ordering operator, $\tilde{\tau}$ is always slightly later than τ. This is to avoid swapping the number operator $c_j^\dagger c_j$ to $c_j c_j^\dagger$. $\langle \dots \rangle = \mathrm{Tr}(\rho_C\rho_B\rho_\gamma\dots)$ is the product initial state ($\rho_{C(B\gamma)}$ is the density matrix in center system, electron baths, and free photon system) and the thermal state is assumed to be of the Gibbs form $\propto e^{-\beta_i H_i}$. Particularly noteworthy is that we

have already incorporated the effect of the scalar photon baths in the distribution ρ_γ, as well as the effect of electron baths in ρ_B so that these quadratic coupling terms do not appear in H_{int} which only contains nonlinear electron-photon interactions.

The standard diagrammatic expansion (or equation-of-motion method) can be used to cast the result in a Dyson equation,

$$D(z,\tau;z',\tau') = D_0(z,\tau;z',\tau') + \sum_j \int d\tau_1 \int d\tau_2 D_0(z,\tau;z_j,\tau_1)\Pi_j(\tau_1,\tau_2)D(z_j,\tau_2;z',\tau'). \tag{4.12}$$

Because of the extreme locality in our interaction terms, the self energies Π_j take discrete values at the site of electrons, and is diagonal in index j. Applying the Langreth rules[41], and using time-translational invariance, the contour-ordered photon Green's function can be made simple in the frequency domain after Fourier transform. This results in a pair of equations, the Dyson equation for the retarded component,

$$D^r(z,z',\omega) = D_0^r(z,z',\omega) + \sum_j D_0^r(z,z_j,\omega)\Pi_j^r(\omega)D^r(z_j,z',\omega), \tag{4.13}$$

where $\Pi_j^r(\omega)$ is the retarded photon self-energy of dot j, and the Keldysh equation which will be discussed in the next subsection.

In order to fully specify the problem and discuss its solution, one needs to give a recipe to compute D_0^r, which is the Green's function for the free photon (including the effect of "Rubin" baths on the left and right sides) governed by the Hamiltonian H_γ.

$$D_0^r(z,t;z',t') = \frac{1}{i\hbar}\theta(t-t')\langle[\phi(z,t),\phi(z',t')]\rangle_{H_\gamma}. \tag{4.14}$$

The easiest approach is to consider the equation of motion of the retarded Green's function. Taking derivatives with respect to t twice, using the commutation relations for ϕ given by Eq.((4.4)), we obtain

$$\epsilon_0 A\left(\frac{1}{c^2}\frac{\partial^2}{\partial t^2} - \frac{\partial^2}{\partial z^2}\right) D_0^r(z,t;z',t') = \delta(z-z')\delta(t-t'). \tag{4.15}$$

Define the usual Fourier transform:

$$D_0^r(z,z',\omega) = \int_{-\infty}^{+\infty} D_0^r(z,t;z',0)e^{i\omega t}\,dt, \tag{4.16}$$

and using time translational invariance, we obtain

$$-\epsilon_0 A\left[\left(\frac{\omega}{c}+i\eta\right)^2+\frac{\partial^2}{\partial z^2}\right]D_0^r(z,z',\omega)=\delta(z-z'). \tag{4.17}$$

We have added a damping term $\eta \to 0^+$ so that the inverse Fourier transform satisfies $D_0^r(z,t,z',0) = 0$ for $t < 0$, consistent with the definition. The differential equation can be solved, yielding the solution

$$D_0^r(z,z',\omega) = -\frac{e^{i(\frac{\omega}{c}+i\eta)|z-z'|}}{2\Omega}, \tag{4.18}$$

where $\Omega = i\epsilon_0 A\left(\frac{\omega}{c}+i\eta\right)$, and it is an important parameter which appears prevalently in this work.

Although the full photon Green's function D^r is defined for the continuum of z, its solution is essentially characterized by the set of points z_j where electrons sit. Thus, we can solve the Dyson equation in matrix form, specializing z and z' to the points $\{z_j\} \cup Z$, where Z is a set of discrete points outside the locations of the electrons. This feature is very convenient, as it turns a continuum problem defined for all z into a discrete problem. The solution is given in matrix form by $D = (D_0^{-1} - \Pi)^{-1}$.

Alternatively, we can also act the differential operator appearing on the left of D_0^r in Eq. ((4.17)) to the Dyson equation, and obtain the differential equation:

$$-\epsilon_0 A\left[\left(\frac{\omega}{c}+i\eta\right)^2+\frac{\partial^2}{\partial z^2}\right]D^r(z,z',\omega)=\delta(z-z')+\sum_j \delta(z-z_j)\Pi_j^r(\omega)D^r(z_j,z',\omega). \tag{4.19}$$

This equation can be interpreted as the scalar potential generated by a unit active (external) charge located at z', together with the induced extra charges at the electron sites, z_j, due to the linear response to the applied field. Indeed, the induced charge at

site j is given by $\delta q_j = \Pi_j^r \phi(z_j)$, and Π_j^r is the associated response function (dynamic susceptibility of the charge). In fact, Π_j^r is exactly the dielectric constant in disguise, given by $\epsilon_j = 1 - v * \Pi_j^r$, where v is the bare Coulomb potential. The detailed solutions for Dyson equation are showed in Appendix (4.8.1).

4.3.2 Keldysh equation

While the retarded Green's functions describe the nature of wave propagation and the equation of motion, (nonequilibrium) thermal dynamic distributions are given by the lesser or greater Green's functions. Since the left side for $z < -L/2$ and $z > L/2$ are designated as photon baths, their effect should be reflected in the distribution. Thus, the lesser Green's function must be based on the decoupled subsystems, symbolically, in the form $D = d + d\Pi D$ (defined on contour), where d is the Green's function of the isolated center (see Appendix (4.8.2)), Π includes the contributions from the dots, Π_i, as well as the photon baths, Π_L and Π_R. The Keldysh equation associated with this contour-ordered Dyson equation is then

$$D^<(z, z', \omega) = \sum_j D^r(z, z_j, \omega)\Pi_j^<(\omega)D^a(z_j, z', \omega), \tag{4.20}$$

where $\{z_j\} = \{-\frac{L}{2}, 0, d, \frac{L}{2}\}$ and $\{j\} = \{L, 0, 1, R\}$ for the two-dot model. The advanced Green's function is given by $D^a(z, z', \omega) = D^r(z', z, \omega)^*$.

In Appendix (4.8.2), we show that the bath self-energy is:

$$\Pi_\alpha^<(\omega) = 2\Omega N_\alpha(\omega), \quad \alpha = L, R \tag{4.21}$$

$$\Pi_\alpha^>(\omega) = 2\Omega(1 + N_\alpha(\omega)), \tag{4.22}$$

where $N_\alpha(\omega) = 1/\big(\exp(\beta_\alpha \hbar\omega) - 1\big)$ is the Bose function at temperature $T_\alpha = 1/(k_B\beta_\alpha)$. Since our baths have negative-definite Hamiltonians, they have to be assigned negative temperatures, $\beta_\alpha < 0$, for a convergent partition function (see section (4.2.3)).

4.4 Energy Currents

4.4.1 Poynting scalar

After setting up the machinery to compute the Green's functions, we now consider how to connect them to physical observables. In our problem, the most important physical quantities are the energy currents. We define the energy leaving the baths as positive, thus,

$$I_\alpha = -\left\langle \frac{dH_\alpha}{dt} \right\rangle, \tag{4.23}$$

where $\alpha = L,\ R,$ and j. We denote the left (right) photon baths by H_L (H_R), while H_j^B, $j = 0, 1, \cdots$ refer to the electron baths. Referring to Fig. (4.1), the conservation of energy is easy to understand, $I_L + I_0 + I_1 + I_R = 0$. The lead currents are given by the well-known Meir-Wingreen formulas[41, 72]:

$$I_j = \int_{-\infty}^{+\infty} \frac{dE}{2\pi\hbar} E \left[G_j^>(E)\Sigma_j^<(E) - G_j^<(E)\Sigma_j^>(E) \right], \tag{4.24a}$$

$$I_\alpha = -\int_{-\infty}^{+\infty} \frac{d\omega}{4\pi} \hbar\omega \left[D^>(\omega, z_\alpha, z_\alpha)\Pi_\alpha^<(\omega) - D^<(\omega, z_\alpha, z_\alpha)\Pi_\alpha^>(\omega) \right]. \tag{4.24b}$$

where $j = 0, 1$, $\alpha = L, R$, and $z_L = -L/2$, $z_R = L/2$.

In addition to the currents leaving the baths, we can also ask: what is the energy current between the dots, or between the dot and photon baths? Towards that end, we shall derive an expression for the energy current carried by the scalar photons. For lack of a better name, we shall call it as the "Poynting scalar", in analogy to classical electrodynamics and reminding oneself that this energy is carried by scalar photons. According to the Hamiltonian (treated classically), Eq. ((4.5)), the energy per unit volume is

$$u(z,t) = -\frac{\epsilon_0}{2}\left[\frac{\dot{\phi}^2}{c^2} + \left(\frac{\partial\phi}{\partial z} \right)^2 \right]. \tag{4.25}$$

Differentiating this expression with respect to time, and using the equation of motion of ϕ in vacuum, we write $\partial u/\partial t + \partial j/\partial z = 0$, with

$$j(z,t) = \epsilon_0 \dot{\phi} \frac{\partial\phi}{\partial z}. \tag{4.26}$$

This will be our starting point to derive a quantized "Poynting scalar" at location z. First and foremost, a symmetrization is in place to ensure hermiticity:

$$\epsilon_0 \dot{\phi} \frac{\partial \phi}{\partial z} \longrightarrow \frac{\epsilon_0}{2} \left[\dot{\hat{\phi}} \frac{\partial \hat{\phi}}{\partial z} + \frac{\partial \hat{\phi}}{\partial z} \dot{\hat{\phi}} \right] \tag{4.27}$$

We now discuss the necessity of anti-normal ordering to remove the zero-point motion contribution. Consider the Hamiltonian Eq. (4.5) *without* the electron-photon interaction H_{int}, which is a solvable system, with the scalar field ϕ given by:

$$\hat{\phi}(z,t) = \sum_q \sqrt{\frac{\hbar}{2\omega_q s L}} \left(\hat{a}_q e^{i(qz - \omega_q t)} + \text{H.c.} \right). \tag{4.28}$$

Here, q is the wavevector and $\omega_q = c|q|$ is the dispersion relation. The bosonic annihilation $\hat{a}_q$ and creation operator $\hat{a}_q^\dagger$ satisfy an unusual commutation relation, i.e. $[\hat{a}_q, \hat{a}_p^\dagger] = -\delta_{qp}$.

Were (4.27) the quantized expression of the "Poynting scalar", one would have:

$$\begin{aligned}
\hat{j}(z,t) &= \epsilon_0 \sum_{q,q'} \text{sgn}(q') \frac{\hbar \sqrt{\omega_q \omega_{q'}}}{2scL} (\hat{a}_q e^{i(qz - \omega_q t)} - \text{H.c.})(\hat{a}_{q'} e^{i(q'z - \omega_{q'} t)} - \text{H.c.}) \\
&= \epsilon_0 \sum_{q,q'} \text{sgn}(q') \frac{\hbar \sqrt{\omega_q \omega_{q'}}}{2scL} \Big([\hat{a}_q \hat{a}_{q'} e^{i(q+q')z - i(\omega_q + \omega_{q'})t} - \hat{a}_q \hat{a}_{q'}^\dagger e^{i(q-q')z - i(\omega_q - \omega_{q'})t}] + \text{H.c.} \Big).
\end{aligned} \tag{4.29}$$

which, upon taking the expectation value with respect to the zero-photon state $|0\rangle$, yields:

$$\langle 0 | \hat{j}(z,t) | 0 \rangle = -\epsilon_0 \sum_q \frac{\hbar \omega_q}{2scL} \text{sgn}(q) \langle 0 | \hat{a}_q^\dagger \hat{a}_q + \hat{a}_q \hat{a}_q^\dagger | 0 \rangle. \tag{4.30}$$

Recall that in present there is no H_{int} but only the free photon field, so the above is expected to vanish. In section (4.2.3), we show that the unusual commutation relation imposes $\hat{a}_q^\dagger |0\rangle = 0$. Therefore, one should perform an anti-normal ordering on (4.27):

$$\hat{j} = \frac{\epsilon_0}{2} | : \dot{\hat{\phi}} \frac{\partial \hat{\phi}}{\partial z} + \frac{\partial \hat{\phi}}{\partial z} \dot{\hat{\phi}} : |, \tag{4.31}$$

with $| : \cdots : |$ the anti-normal ordering, so that in the non-interacting scenario the current

expectation value is zero. Having achieved the purpose of quantizing the "Poynting scalar", we shall also drop the hats on the quantum operators. We show in Appendix C that when the expectation value is taken (with respect to a nonequilibrium steady state), the above can be written as:

$$\langle j(z)\rangle = \epsilon_0 \int_0^\infty \frac{d\omega}{\pi} \hbar\omega \mathrm{Re}\, \frac{\partial D^>(\omega, z, z')}{\partial z'}\bigg|_{z'=z}. \tag{4.32}$$

Energy conservation dictates that $I_L + I_0 = Aj(d/2)$ and $I_1 + Aj(d/2) + I_R = 0$. Therefore, it is mandatory for the "Poynting scalar" to agree with the heat current entering the photon bath. Indeed, it can be shown that $I_{L,R} = Aj(z)$ when $z < 0$ or $z > d$, as outlined in the next section. In what follows, we shall refer to the integrand in Eq. (4.32) as the "spectral transfer function".

4.4.2 Currents in various limits

Notice that the parameters η, L are introduced to dodge the pole of the retarded unperturbed photon Green's function, and to give our problem a finite size. Recall also that the speed of light c should be taken as ∞ for a gauge-consistent theory. In this section, we consider different limiting procedures for these parameters η, c, L, and discuss their significance by studying the resulting current expression.

$\eta \to 0^+$ limit

First, we consider the perfect medium limit, $\eta \to 0^+$, keeping the other parameters of the model fixed. Only in this limit, the energies I_α from various baths are strictly conserved during wave propagation. Indeed, for $\eta \to 0^+$, the parameters λ, δ, and γ become phase factors with unit modulus. As a result, the retarded and lesser photon Green's functions become independent of the central region size L, and $j(z)$ is piecewise constant.

We give the heat current calculated from Meir-Wingreen formula, I_L, I_R, as well as the "Poynting scalar" expression $Aj(z)$, for $z < d$, $0 < z < d$, and $z > d$ without committing ourselves to the actual form of the self energies due to electrons, $\Pi_{0,1}^{r,<,>}$.

For the bath spectral functions, we have $\Pi^r_\alpha - \Pi^a_\alpha = \Pi^>_\alpha - \Pi^<_\alpha = 2\Omega$, $\alpha = L, R$. So these formulas are still fairly general. The formulas are obtained straightforwardly using the solutions of the retarded Green's function D^r, together with the Keldysh equation, $D^{<,>} = D^r \Pi^{<,>} D^a$, and the assumption $|\lambda| = |\gamma| = |\delta| = 1$:

$$\begin{aligned} I_L = -\int_{-\infty}^{+\infty} \frac{d\omega}{2\pi}\, \hbar\omega\, \Omega \Big\{ & |D_{00}|^2 \left(\Pi_0^> N_L - \Pi_0^< (N_L+1)\right) + \\ & |D_{01}|^2 \left(\Pi_1^> N_L - \Pi_1^< (N_L+1) + 2\Omega(N_R - N_L)\right) \Big\}. \end{aligned} \tag{4.33}$$

Here, N_L and N_R are the Bose functions associated with the photon baths, and D_{00} and D_{01} are defined in Appendix (4.8.1). A similar expression can be written down for I_R. The "Poynting scalar" formula is

$$\begin{aligned} Aj(z<0) = -\int_0^{+\infty} \frac{d\omega}{\pi}\, \hbar\omega\, \Omega \Big\{ & |D_{00}|^2 \left(\Pi_0^> + 2\Omega(N_L+1)\right) \\ & + |D_{01}|^2 \left(\Pi_1^> + 2\Omega(N_L+1)\right) + \quad (N_L+1)(D_{00}^* - D_{00}) \Big\}. \end{aligned} \tag{4.34}$$

Since I_L and $Aj(z<0)$ have the same physical meaning–the energy from the left bath going to the right–they should be identical. Indeed, this can be shown using an important identity for the Green's functions[137]:

$$D^r - D^a = D^r(\Pi^r - \Pi^a)D^a, \tag{4.35}$$

where D^r, Π^r, etc., are 4×4 matrices whose entries correspond to the positions $z \in \{-L/2, 0, d, L/2\}$, and Π^r is diagonal with diagonal elements $\{\Pi^r_L, \Pi_0, \Pi_1, \Pi^r_R\}$. Using this identity, and the relation $\Pi_j - \Pi_j^* = \Pi_j^> - \Pi_j^<$, $j = 0, 1$, the last term $\mathrm{Im}\, D_{00}$ in the "Poynting scalar" formula can be transformed into a form involving the self energies, and the equivalence is proved.

Local equilibrium approximation (LEA)

As the electron contributions to photon self energies, $\Pi_j^{r,<}$, are not known exactly, one has to make various approximations in order to make concrete predictions. In this paper, we consider three kinds of approximations. The local equilibrium approximation,

the Born approximation (BA), and the self-consistent Born approximation. We first elaborate on the LEA. By LEA, we mean that the electrons are in respective equilibrium with the associated electron baths. Specifically, we assume that the electron-photon interaction is so weak that the thermal equilibria of the electrons are not disturbed. Thus, the charge's degrees of freedom being in equilibrium, the corresponding self energies satisfy the fluctuation-dissipation theorem:

$$\begin{aligned} \Pi_j^< &= N_j(\Pi_j - \Pi_j^*), \\ \Pi_j^> &= (N_j + 1)(\Pi_j - \Pi_j^*), \quad j = 0, 1. \end{aligned} \tag{4.36}$$

Notice that the photon self energies are related to the charge's degrees of freedom $c_j^\dagger c_j$, so the flucutation-dissipation theorem is boson-like, with Bose function $N_j = 1/(\exp(\beta_j \hbar\omega) - 1)$.

Under LEA, our theory is identical to Rytov fluctuation electrodynamics[107] (except here, we consider charge fluctuations). We denote the transmission function by $T_{\alpha\beta}(\omega)$. For our two-dot model, there is a "detailed-balance" condition, i.e. $T_{\alpha\beta}(\omega) = T_{\beta\alpha}(\omega)$. Based on such relation, the four-terminal Laudauer-$\mathrm{B\ddot{u}ttiker}$ form of current expression can be derived for the bath $\alpha = L$, 0, 1, and R:

$$I_\alpha = \int_0^\infty \frac{d\omega}{2\pi} \hbar\omega \sum_{\gamma=L,0,1,R} [N_\alpha(\omega) - N_\gamma(\omega)] T_{\alpha\gamma}(\omega). \tag{4.37}$$

This form guarantees energy conservation explicitly, $\sum_\alpha I_\alpha = 0$. The transmission

functions are given explicitly by:

$$T_{01} = \left|\frac{4\Omega}{\mathcal{D}}\right|^2 \mathrm{Im}\Pi_0\,\mathrm{Im}\Pi_1, \tag{4.38}$$

$$T_{0L} = 4|\Omega||D_{00}|^2\,\mathrm{Im}\Pi_0, \tag{4.39}$$

$$T_{0R} = \frac{16}{|\mathcal{D}|^2}|\Omega|^3\,\mathrm{Im}\Pi_0, \tag{4.40}$$

$$T_{1L} = \frac{16}{|\mathcal{D}|^2}|\Omega|^3\,\mathrm{Im}\Pi_1, \tag{4.41}$$

$$T_{1R} = 4|\Omega|\,|D_{11}|^2\,\mathrm{Im}\Pi_1, \tag{4.42}$$

$$T_{LR} = \frac{(2\Omega)^4}{|\mathcal{D}|^2}. \tag{4.43}$$

The diagonal terms $T_{\alpha\alpha}$ are irrelevant, and other terms are obtained by symmetry, $T_{\alpha\beta} = T_{\beta\alpha}$.

We consider some special cases. If $\Pi_0 = \Pi_1 = 0$, i.e. a system with no dot, then all the transmission functions are 0 except $T_{LR} = 1$. This represents a perfect transmission from the left bath to right bath. If the two photon baths have different temperatures, the whole system is not in thermal equilibrium and an energy current flows between the two photon baths.

Next, we consider the energy exchange between scalar photons and electrons. Notice that $\mathrm{Im}\Pi_j < 0$ if $\omega > 0$ as shown in Fig. (4.2). This means that the transmission coefficients between the photon baths and electron, i.e. Eqs. (4.39)–(4.42) are negative. Now, scalar photon baths, having negative-definite Hamiltonians, must be assigned a negative temperature (see section (4.2.3)). Therefore, the difference of the Bose function between a scalar photon and an electron bath is always negative, i.e. $N_{L/R} - N_{0/1} < 0$ for $\omega > 0$. Thus the integrand in the Landauer-Büttiker formula (4.37) is always positive when we consider the energy contributed by scalar photons to the electrons. This matches the expectation that a negative temperature is hotter than any positive temperature[138, 139]. However, as we discuss in the following subsection, scalar photon baths will not play any role when $c \to \infty$.

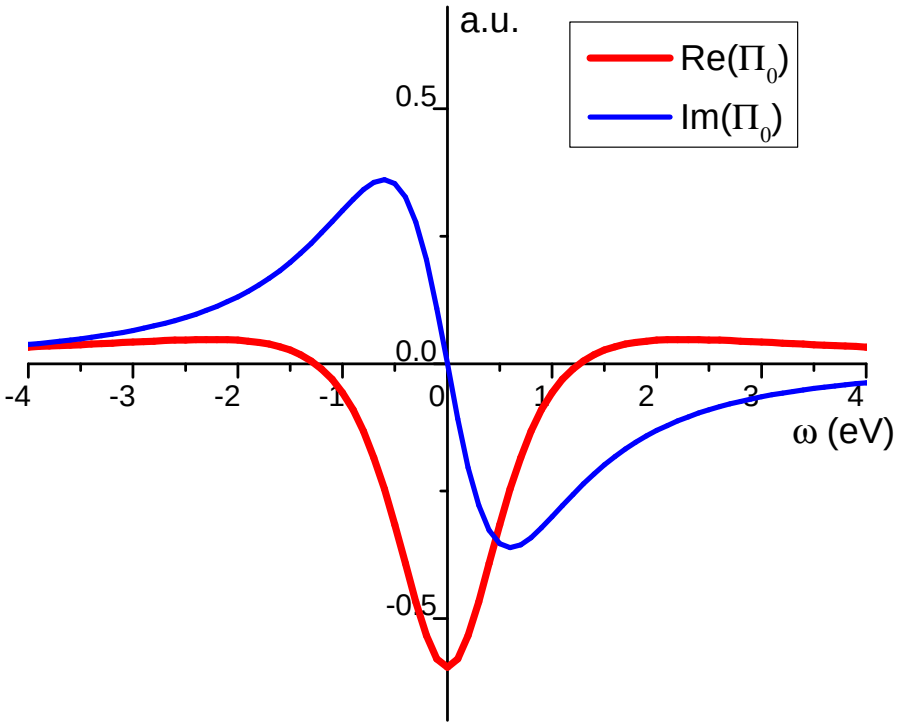

Fig. 4.2: Real and imaginary part of the photon self-energy.

$c \to \infty$ limit

Infinite speed of light is the limit that must be taken for a gauge-consistent theory. One could think of c as a speed that is needed only for field quantization. Once it has served this purpose, in all resulting expressions, e.g. the current formula, transmission coefficients, one eliminates c by letting it goes to infinity.

Returning to the transmission coefficients, observe that the speed of light appears in $\Omega = i\epsilon_0 A\omega/c = O(1/c)$ (we already sent η to 0^+), and also $\mathcal{D} = O(1/c)$. Using this fact, the coefficients that involve at least one photon bath, i.e. Eqs. (4.39)–(4.43) can be shown to vanish, leaving T_{01} as the only nonzero transmission. This shows that in the strict Coulomb interaction limit, energy cannot be transmitted to long distances. We also comment that the infinite speed limit is a robust limit independent of how the other limits (η and L) are taken.

When $c \to \infty$, the transmission function between dot 0 and dot 1, Eq. (4.38)

simplifies to:

$$T_{01} = \frac{4\,\mathrm{Im}\Pi_0\,\mathrm{Im}\Pi_1}{|\Pi_0 + \Pi_1 - \Pi_0\Pi_1/C|^2}, \tag{4.44}$$

where the parameter $C = \epsilon_0 A/d$ is precisely the capacitance of the parallel plate capacitor. This shows that our model contains indeed the physics of parallel-plate capacitors. Furthermore, the pole of (4.44) gives a critical length $\tilde{d}$:

$$\tilde{d} = \epsilon_0 A \left(\frac{1}{\Pi_0(0)} + \frac{1}{\Pi_1(0)} \right), \tag{4.45}$$

where the self energies are evaluated at zero frequency. Notice that $\tilde{d}$ is a negative quantity in normal systems, so the transmission never really diverges. But $\tilde{d}$ is a length scale that differs markedly from the thermal wavelength $\lambda_T = 2\pi\hbar c/(k_B T)$.

$L \to \infty$ limit

In contrast to the above two limits, we get rid of the photon bath in a technically consistent way, that is, we let the medium (the vacuum) be dissipative, and we put the baths at $\pm\infty$. In the limit $L \to \infty$ but keeping η finite, the medium consumes the bath energies. As a result, the bath contribution disappears. Since the baths are infinitely far away, their energies are dissipated on the way to the dots, so it is equivalent to having a distribution which is strictly 0. We are left with the dots only.

In Fig. (4.3), we numerically check the distance dependence of heat current in three different limits. We find that blue circles and green triangles almost coincide with the red solid line. This indicates that the currents in three different limits are consistent: the $c \to \infty$ limit is similar with both LEA and BA. However, energy conservation of the whole system is not guaranteed under BA. Hence, in numerical calculations, it is the self-consistent Born approximation (SCBA) that we use to calculate the nonequilibrium "Poynting scalar".

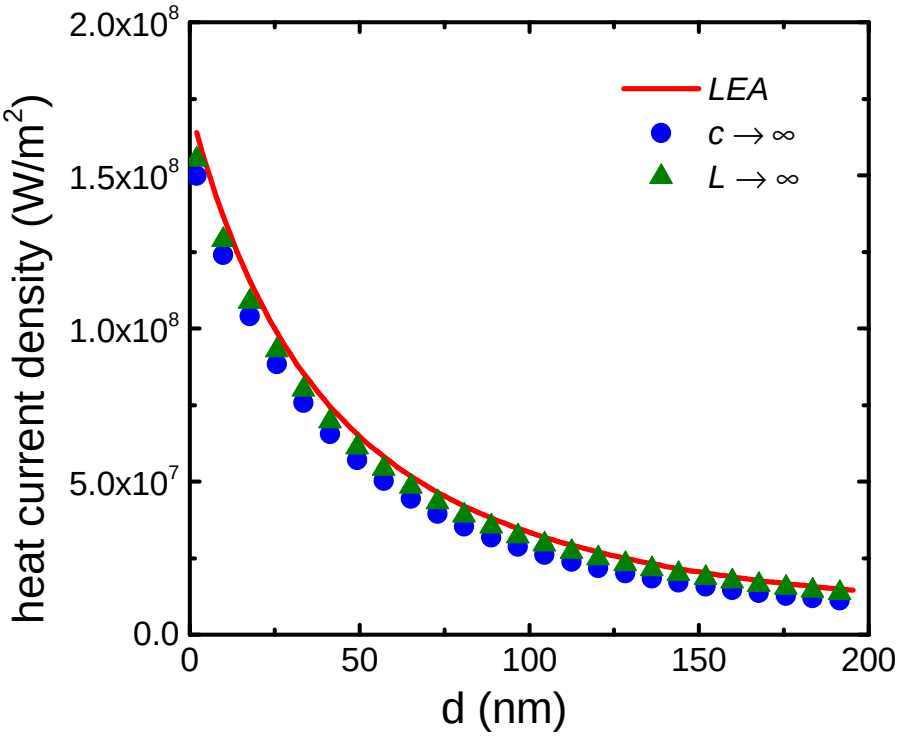

Fig. 4.3: Distance dependence of heat current under different limits. The temperature of dot 0 is 1000 K and dot 1 is 300 K. In LEA calculation, the temperature of left and right photon bath is set as -30 K. The onsite energy of dot 0 is 0.0 eV and dot 1 is 0.01 eV. The chemical potential of dot 0 is 0.0 eV and dot 1 is 0.02 eV. We take the wide band limit(4.51), with $\Gamma_0 = 1$ eV and $\Gamma_1 = 0.5$ eV, $E_0 = E_1 = 50$ eV. The Q factor is $1e$ and the area of capacitor $A = 19.2\times19.2$ nm^2.

4.5 Calculations of self energies

To make numerical predictions of our analytic formulas for the currents, we need a way of computing the photon self energies. If the local equilibrium approximation (LEA) is assumed, we only need to know the retarded self energies. This correlation function can be calculated exactly since we assume that the electrons are kept in equilibra with the baths, unaffected by the photons. A formula is given in Appendix (4.8.3). However, if the electron-photon interaction of our model is taken into account, there is no exact method for such calculations, except the purely formal Hedin equation[140]. Thus, we consider various approximation schemes.

4.5.1 Photon self-energy

In a diagrammatic expansion of the contour-ordered scalar photon Green's function $D(\tau, \tau')$, we can write the result as a Dyson equation. The lowest order term in this expansion for the self-energy (all the irreducible diagrams) $\Pi(\tau, \tau')$ is [42, 141]

$$\Pi_{jk}(\tau, \tau') \approx \frac{1}{i\hbar}\langle T_\tau q_j(\tau) q_k(\tau')\rangle_{H_e}, \tag{4.46}$$

where $q_j = (-Q)c_j^\dagger c_j$ is the charge operator at site j. Notice that $\Pi_{jk}(\tau, \tau') = 0$ if $j \neq k$, true for all orders, because we excluded inter-dot coupling in the Hamiltonian (4.5). In other words, electrons are not allowed to jump from one site to the other. Since Π is diagonal, we use the notation $\Pi_j \equiv \Pi_{jj}$. After applying Wick's theorem[142], the resulting expression can be written as a series of diagrams, see Fig. (4.4). If we stop here and use the equilibrium distributions of the electrons G_0, we obtain LEA, as discussed earlier. This is however not an exact result. We have neglected many diagrams and kept only the loop (polarization) diagram (see Fig. (4.4)(a)). In particular, we have ignored a class of nontrivial diagrams known as ladder diagrams (see Fig. (4.4)(b)). In order to include systematically the ladder diagrams, we need to solve the Bethe-Salpeter equation[142, 143], which is computationally much more involved.

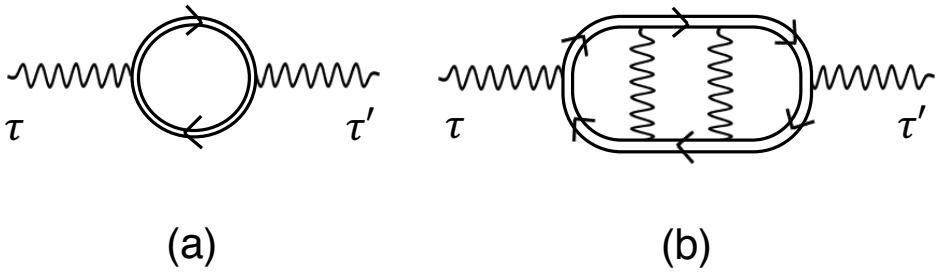

Fig. 4.4: Diagrammatic expansion of the photon Green's function (4.10), including the photon lines at both ends. (a) Lowest-order non-trivial loop diagram. (b) Typical ladder diagram in higher-order expansions which are not included.

The next level of approximation is the Born approximation (BA). In the Born approximation, we do not use the equilibrium Green's functions of the electrons. Instead, we include the lowest order nonlinear self-energy as a perturbation. As it turns out, this is a bad approximation, because energy conservation is not done consistently. More

precisely, the energy conservation, $\sum I_\alpha = 0$, is violated at the next order (Q^4) of approximation.

Thus, for numerical simulations, we adopt the well-established self-consistent Born approximation (SCBA)[130]. This calculation requires iterations until a convergence criterion is attained. Fig. (4.5) shows the Ferman diagrams for electron self-energy where the screened Coulomb interaction is donated by the double wiggled line and the interacting Green function is denoted by a double straight line. In GW method, the self energy is also given by similar diagrams. However the GW method can be derived when we neglect the vertex corrections completely in Hedin equations. The SCBA used here can be understood though GW methods and Hedin equations.

As mentioned, we only keep diagram (a) in Fig. (4.4). The nonlinear photon self-energy in contour time is given by:

$$\Pi_j(\tau,\tau') = -i\hbar Q^2 G_j(\tau,\tau')G_j(\tau',\tau). \tag{4.47}$$

After applying the Langreth rules[41], the photon self energies in real time read:

$$\begin{aligned}
\Pi_j^{>}(t) =& -i\hbar Q^2 G_j^{>}(t)G_j^{<}(-t),\\
\Pi_j^{<}(t) =& -i\hbar Q^2 G_j^{<}(t)G_j^{>}(-t),\\
\Pi_j^{r}(t) =& \theta(t)\left[\Pi_j^{>}(t) - \Pi_j^{<}(t)\right],
\end{aligned} \tag{4.48}$$

where $\theta(t)$ is the Heaviside step function. In numerical calculations, we transform Eq. (4.48) to the frequency domain using the fast Fourier transform.

4.5.2 Electron self-energy

For an unperturbed electron, the retarded Green's function is written in standard form,

$$G_{0,j}^r(\omega) = \frac{1}{\hbar\omega - v_j - \Sigma_{b,j}^r(\omega)}, \tag{4.49}$$

where the subscript 0 refers to the absence of interaction and v_j is the onsite energy of dot j, $\Sigma^r_{b,j}(\omega)$ is the retarded electron bath self-energy for electron bath j, given explicitly by:

$$\Sigma^r_{b,j}(\omega) = \sum_{k\in\text{bath}} \frac{|V_{jk}|^2}{\hbar\omega + i\eta_k - \epsilon_{jk}}, \tag{4.50}$$

where one must then specify the mode energy ϵ_{jk}, coupling strength V_{jk} and damping factor η_k for mode k in bath j. In this work, we use the Lorentz-Drude model[144]:

$$\Sigma^r_{b,j}(\omega) = \frac{\Gamma_j/2}{i + \hbar\omega/E_{0,j}}. \tag{4.51}$$

The wide-band limit is obtained by taking $E_0 \to \infty$, which reduces the self-energy to a constant. Adding a decay makes it more physical, as the real time function $\Sigma^r(t)$ has an exponential decay with decay time $\hbar/E_0$. This model has been used for electronic transport studies of quantum dots[41, 144]. In calculations, we set Γ and $E_0 > 0$ as constant. The free electron lesser Green's function can be easily derived using the fluctuation-dissipation theorem for electrons. When electron-photon interaction is active, the full retarded Green's functions are obtained from a Dyson equation and the lesser Green's function can be derived from Keldysh equation with external interaction self-energy:

$$G^r_j(\omega) = \frac{1}{\hbar\omega - v_j - \Sigma^r_{b,j}(\omega) - \Sigma^r_{n,j}(\omega)}, \tag{4.52}$$

$$G^<_j(\omega) = G^r_j(\omega)[\Sigma^<_{b,j}(\omega) + \Sigma^<_{n,j}(\omega)]G^a_j(\omega). \tag{4.53}$$

$\Sigma^{r,<}_{n,j}(\omega)$ is the retarded and lesser self-energy due to nonlinear electron-photon interactions at site j. $\Sigma^<_{b,j}(\omega)$ is the lesser Green's function of the electron bath which can be derived from the fluctuation-dissipation relation, i.e. $\Sigma^<_{b,j}(\omega) = -f_j(\omega)[\Sigma^r_{b,j}(\omega) - \Sigma^a_{b,j}(\omega)]$, where $f_j(\omega) = 1/\{\exp([\beta_j(\hbar\omega - \mu_j)] + 1\}$ is the Fermi distribution for dot j. $G^r_j(\omega)$ is the total retarded Green's function and $G^<_j(\omega)$ is the total lesser Green's function. For our two-dot capacitor model, the nonlinear self energies $\Sigma^{r,<}_{n,j}(\omega)$ can be obtained from the Hartree and Fock diagrams[132] (see Fig. (4.5)) in a diagrammatic expansion for

the Green's function $G(\tau, \tau')$.

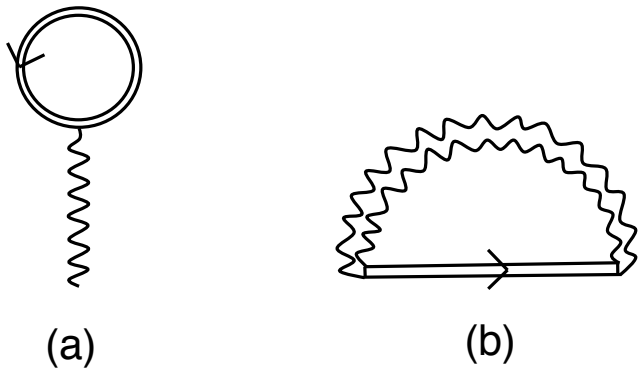

Fig. 4.5: Self energies in the diagrammatic expansion of the electron Green's function $G(\tau, \tau')$. (a) Hartree term. (b) Fock term.

For each of the dots $j = 0$, 1, up to first non-trivial diagrams, we have, for the nonlinear electron self energies:

$$\begin{aligned}
\Sigma^{<}_{n,j}(t) &= i\hbar Q^2 G^{<}_{j}(t) D^{<}(z_j, z_j, t), \\
\Sigma^{r}_{n,j}(t) &= \theta(t)[\Sigma^{>}_{n,j}(t) - \Sigma^{<}_{n,j}(t)] \\
&\quad - i\hbar Q^2 \sum_{k=0,1} \Big[- G^{<}_{k}(t=0) \int dt' D^{r}_{0}(z_j, z_k, t') \Big].
\end{aligned} \tag{4.54}$$

Hence, electrons interact with photons via the photon Green's function D, which in turn interacts with the electron Green's function G. Thus the equations have to be solved iteratively.

4.5.3 Computational Details

In actual calculations, we always take the limit $c \to \infty$, under which Eq. (4.60) reduces to:

$$\begin{aligned}
D_{00} &= \frac{C - \Pi_1}{\mathcal{D}}, \\
D_{11} &= \frac{C - \Pi_0}{\mathcal{D}}, \\
D_{01} &= D_{10} = \frac{C}{\mathcal{D}},
\end{aligned} \tag{4.55}$$

where, as before, $C = A\epsilon_0/d$ is the capacitance but the denominator is now $\mathcal{D} = \Pi_0\Pi_1 - C(\Pi_0 + \Pi_1)$. With these coefficients, the radiative heat current in the limit $c \to \infty$ simplifies from Eq. (4.32) to:

$$\langle j \rangle = \frac{1}{A}\int_0^\infty \frac{d\omega}{\pi}\mathrm{Re}\left[i\hbar\omega|D_{10}|^2(\Pi_1^>\mathrm{Im}\Pi_0 - \Pi_0^>\mathrm{Im}\Pi_1)\right]. \tag{4.56}$$

Numerically, the terms (4.55) diverge in the high frequency regime, leading to unstable iterations under SCBA. To overcome this difficulty, we multiply Eq. (4.55) with an artificial damping factor $\frac{1}{1+(E/E_d)^2}$ to help with convergence under SCBA and E_d is set as 4 eV in the following calculations. We have checked numerically that despite this artificial damping, energy conservation is still satisfied after several iterations.

4.6 Results and discussion

BA vs SCBA In this paragraph, we first discuss the differences between BA and SCBA. The solid lines in Fig. (4.6) show the heat current between two quantum dots under BA with different dot chemical potentials. A first observation is that the chemical potential of quantum dots hugely influences the heat current. As the chemical potential increases, the total heat current under BA decreases and eventually converges to the same value at large dot separation. Such convergence can be understood by the evanescent properties of the scalar field: with an increasing gap between the dots, the heat current density decreases and ultimately becomes insensitive to the source properties. However, in sharp contrast to BA, currents computed under SCBA (dotted lines) increase with chemical potential. This can be understood as follows. As the chemical potential is increased (within a reasonable parameter region), the dot becomes highly occupied, leading to a stronger electron-photon interaction. Under SCBA, the self energies of electrons and scalar photons are updated at each iteration, allowing this strong interaction to be more aptly captured. On the other hand, BA crudely stops at just the first iteration. Therefore, one expects the heat current to be enhanced under SCBA and not necessarily so for the case of BA. Another observation is that both BA and SCBA show a convergence (at

large dot separation) of heat currents towards two different chemical potentials. Finally, it is seen that the chemical potential only affects the heat current at small distances, which again can be understood from the rapidly-decaying property of the scalar field.

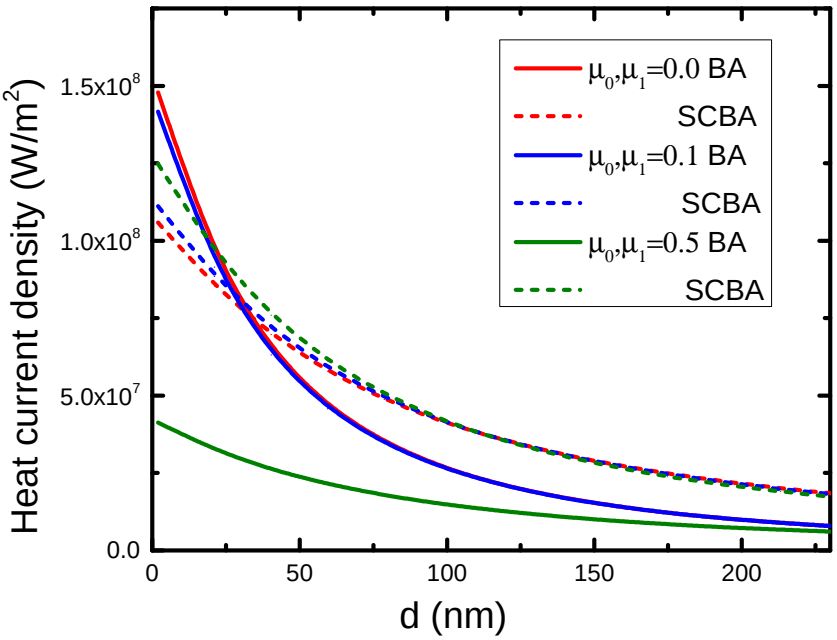

Fig. 4.6: Distance dependence of heat current density for different dot chemical potentials, using either BA or SCBA. The temperature of dot 0 is 1000 K and dot 1 is 300 K. The chemical potentials of both dots are equal. $Q = 1e$.

Q and area dependence In our model, the parameter Q is the maximum charge at the dot. It also determines the strength of electron-photon interaction. Fig. ((4.7)a) shows the Q dependence of the heat current density at different chemical potentials. As in Fig. (4.6), the heat current between two quantum dots can be amplified by increasing the dot chemical potential. Besides, the heat currents at different chemical potentials converge to the same value as Q is increased. This can be understood as follows: with a strong electron-photon interaction, the electrons in quantum dots are less prone to excitations by thermal fluctuation alone. Hence, the effect of chemical potential on the heat current is expected to diminish for large Q.

For smaller values of Q, the heat current is more easily controlled by the chemical

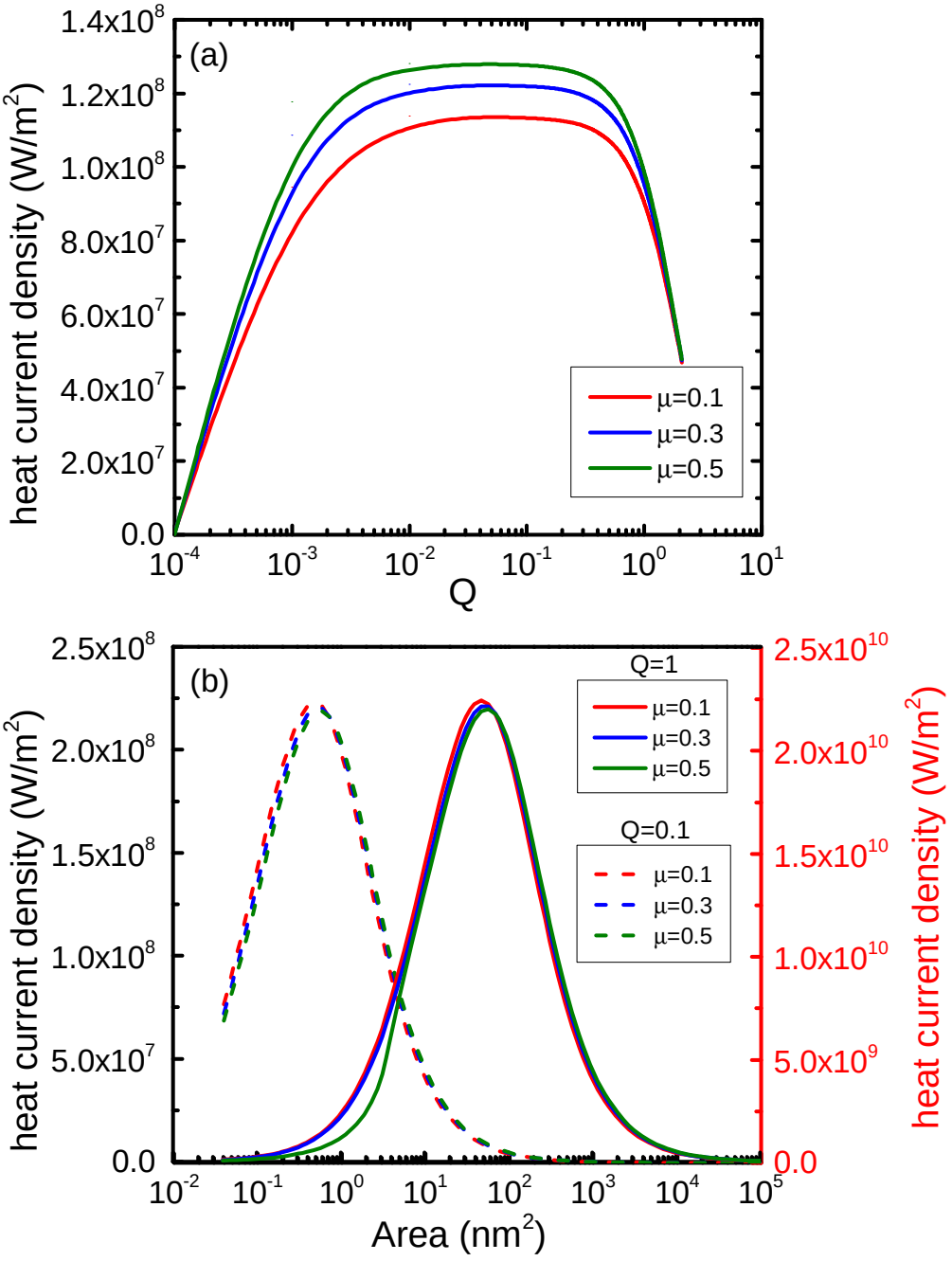

Fig. 4.7: Charge-dependence and area-dependence of the heat current density for different dot chemical potentials under SCBA. (a) Charge-dependence of current density. (b) Area dependence of current density. The left axis scale corresponds to the solid line and right axis scale corresponds to the dashed line. The temperature of dot 0 is 1000 K and dot 1 is 300 K. The chemical potentials of both dots are the same. The distance between the two dots is 19.7 nm.

potential of quantum dots. However, as Q approaches zero, the heat current decays rapidly, and vanishes for $Q = 0$. Therefore, this parameter needs to be optimally chosen to control the heat transfer. For gold, the free electron concentration is 5.90×10^{22} cm^{-3} and the estimated value of Q is of the order of $10^3 e$. In this case, the scalar field is therefore not expected to be the dominant heat transfer channel. On the contrary, semiconductors or certain 2-d materials such as graphene have much lower free electron density compared to bulk gold, $Q \approx 10^{-1} e$, hinting at a more controllable RHT by tuning the chemical potential.

Fig. ((4.7)b) shows the area dependence of the heat current density between the two dots. Comparing the peak positions of the solid and the dashed line (corresponding to different Q), we find that the peak position is proportional to Q^2. Hence, within this parameter regime ($0.1e < Q < 1e$), the dot area A, which governs partly the capacitance $C = \epsilon_0 A/d$, plays a crucial role in the heat transfer.

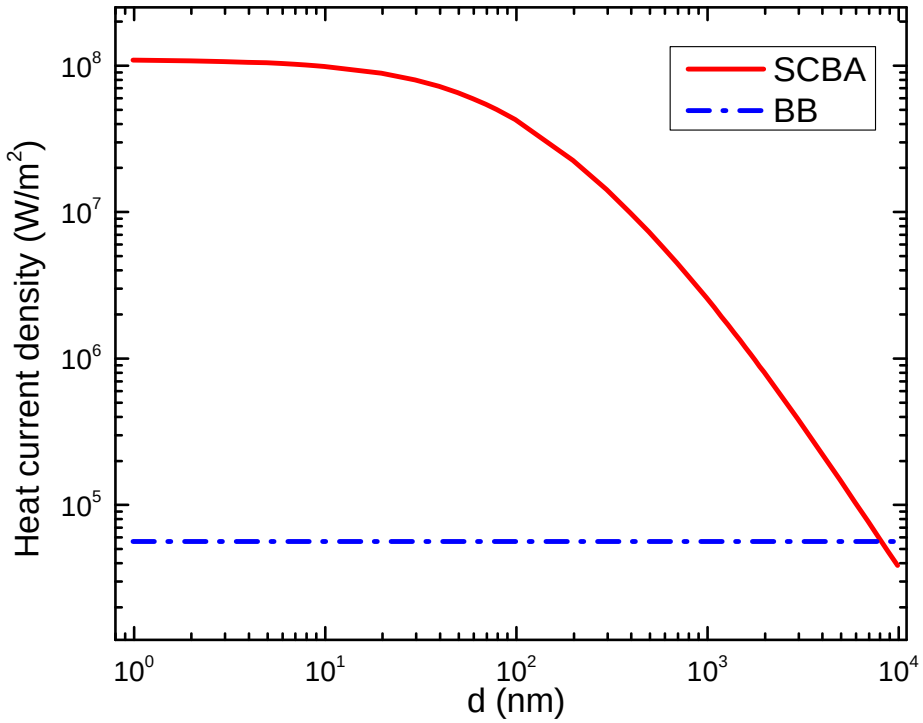

Fig. 4.8: Current calculation under SCBA and the blackbody limit in log-log plot. The temperature of dot 0 is 1000 K and dot 1 is 300 K. The chemical potential of dot 0 is 0.0 eV and dot 1 is 0.02 eV. $Q = 1e$ and the area is set as 388 nm^2.

Scalar field vs blackbody limit Fig. (4.8) presents the distance dependence of heat current density in a double logarithmic plot. For large distances, the heat current density decreases like d^{-2}. Such a scaling law arises from the capacitor property, which can be manifested in the expression for transmission coefficient when $c \to \infty$, i.e. Eq. (4.44). This is different from the case of p-polarized waves, which diverges like d^{-2} only for short distance (< 0.1 nm). Our prediction of a d^{-2} scaling at large distances for a nanocapacitor can be experimentally tested, such as with a tip-plane heat current measurement. However, the heat current is suppressed at close separation because of the large value of capacitance when the two dots are nearly in contact. With such large capacitance, our calculation predicts a constant transmission in the $d \to 0$ limit.

Fig. (4.8) shows an extremely large enhancement of heat transfer mediated by the scalar photons. Comparing the red solid and blue dashed-dotted lines at 10 nm, we find that the heat current density is two thousand times larger than the blackbody limit. This result demonstrates that the heat transfer channel provided by electron-photon interaction is the dominant one for nanocapacitors at small separations.

Capacitor physics Fig. ((4.9)a) shows the heat current density $\langle j \rangle$ as a function of the two-dot separation d. A key parameter is the area A; we choose it to be close to the experimental values in Ref. [9]. The results are insensitive to the onsite potentials v_j and chemical potentials μ_j, provided Γ_j is large. We note that the energy current takes an exact scaling form, $\langle j \rangle A = F(x)$, $x = A/(Q^2 d)$, with the area A, distance d, and charge Q. Further analysis shows that $F(x) \propto x^2$ for small x and approaches a constant for large x. Under the strong coupling limit, $k_B T_j \ll \Gamma_j$, in addition to a T_j^4 temperature dependence, the current is proportional to $A/(d^2 Q^4)$ for small x and $1/(A\Gamma^2)$ for large x [here $\Gamma \approx \max(\Gamma_0, \Gamma_1)$]. The crossover from one type of behavior to the other type of behavior is controlled by $\Gamma \approx Q^2/(2C)$. Alternatively, a length scale can be obtained from D_{01}, giving $\tilde{d} = -\epsilon_0 A[1/\Pi^r_{00}(0) + 1/\Pi^r_{11}(0)]$. The current decreases as $1/d^2$ for large d and saturates at the scale given by $\tilde{d}$ (about $40\,\mathrm{nm}$ with our choice of parameters) for small d.

This phenomenon is different from near-field radiative heat transfer results at a

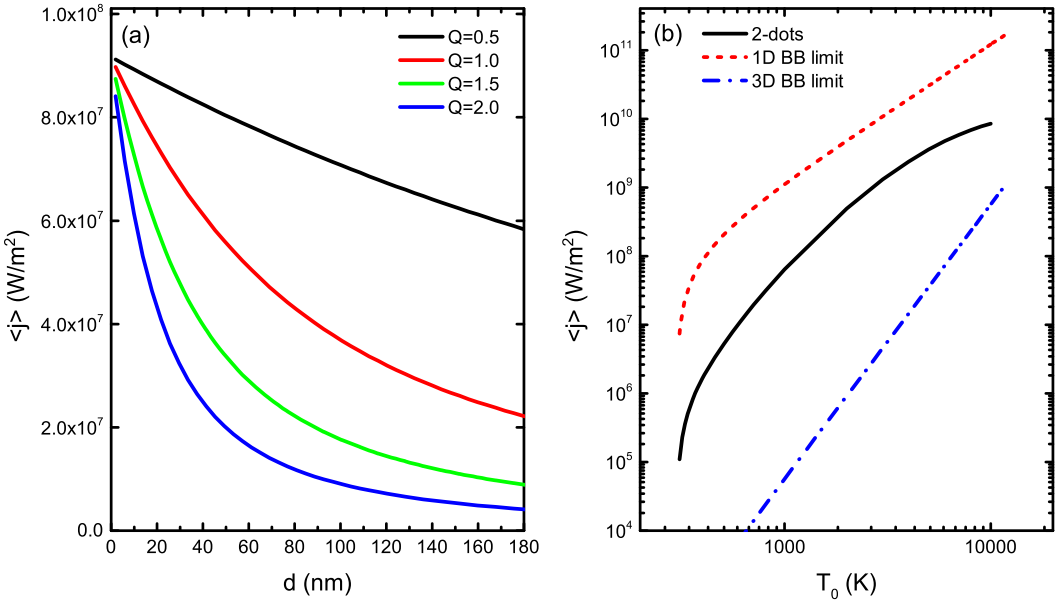

Fig. 4.9: (a) Heat current density $\langle j \rangle$ as a function of distance d with different maximum charge Q for the two-dot model. We set the temperatures of the baths at $T_0 = 1000\,\mathrm{K}$, $T_1 = 300\,\mathrm{K}$, chemical potentials $\mu_0 = 0\,\mathrm{eV}$, $\mu_1 = 0.02\,\mathrm{eV}$, and onsite $v_0 = 0$, $v_1 = 0.01\,\mathrm{eV}$, area $A = 388\ (\mathrm{nm})^2$, and the electron bath parameters $\Gamma_0 = 1\,\mathrm{eV}$, $\Gamma_1 = 0.5\,\mathrm{eV}$, $E_0 = 2.0\,\mathrm{eV}$, $E_1 = 1.0\,\mathrm{eV}$. (b) The temperature dependence of heat current density. Here, we set $T_1 = 300\,\mathrm{K}$ and vary T_0, with $d = 35.5\,\mathrm{nm}$ and $Q = 1\,e$. Other parameters are the same as previous figure.

length scale less than $\hbar c/(k_B T)$ dominated by evanescent modes when the transverse component of the wave vector $q_\perp > \omega/c$. There are no evanescent modes in our 1D model since $q_\perp = 0$ permanently. Besides, Fig. (4.9)(a) also shows large values of heat transfer. At the saturation value, the heat current density is approximately 9×10^7 W/m^2, which is about a thousand times larger than the black-body (BB) limit of 5.6×10^4 W/m^2. This enhancement is at least one order of magnitude larger than a typical PvH theory prediction for metals, which is in the range of the hundreds. Compared to a one-dimensional Landauer formula (1D BB) result with perfect transmission, i.e. 1.1×10^9 W/m^2, our numbers are about 1/12-th of that upper limit [145]. Such enhancement is mainly due to transverse confinement (there is only one transmission mode) and the small area A. The temperature dependence of the current density is plotted in Fig. (4.9)(b). Asymptotically for large T_0 fixing T_1, the Stefan-Boltzmann law gives the fourth power of T_0 and the 1D BB limit gives a quadratic function of T_0.

The results presented above are for strong couplings, where Γ_j is comparable to electron energy scale of order eV. For weak couplings, SCBA convergence is difficult.

However, we observe the physics remains qualitatively the same if we do not do self-consistency. In such a framework, the photon self-energies $\Pi^{>}_{jj}$ can be approximated by the fluctuation-dissipation theorem, assuming each dot is in local thermal equilibrium. Within this framework of approximation, we can recover a Caroli/Landauer formula.

4.7 Conclusion

In this Chapter, using the method of NEGF, we studied the heat flux between a nanoscale capacitor, mediated by the Coulomb interaction, generated by charge fluctuation. By modeling the capacitor as a double quantum dot, we ruled out transverse electrical current and focused only on charge fluctuation. Keeping in mind that $c \to \infty$ must be taken at the end for a gauge-invariant theory, we worked under Lorenz gauge to quantize the scalar potential. We then outlined the framework of NEGF and solved the Dyson equation. From a classical continuity equation, we derived a Coulomb heat flux, dubbed "Poynting scalar", discussed its quantization, and related it to the greater Green's function. Next, we studied the current expression under various limits of three model parameters. This was achieved by focusing on the local equilibrium approximation, which bridges our approach and Rytov's theory. To illustrate the greater generality of NEGF, we discussed two approximation schemes on the self energies: the BA and SCBA. Finally, we performed numerical simulations, explored the dependences of heat current on different parameters, and demonstrated how chemical potential can be used to tune radiative thermal rectification. We also found a thousandsfold enhancement of the heat current compared with the blackbody limit and discovered a new distance dependence $(1/d^2)$ at large distances.

Although our model might be unrealistic, it contains an essential feature of most thermal transport problems: a left/right partition of the whole system. It also helps address several issues, such as the ambiguity of heat fluxes ("Poynting scalar" and photon bath energy current), the necessity of a negative definite scalar photon Hamiltonian, and perhaps most importantly how our approach is a generalization of Rytov's phenomenological theory. A more interesting three-dot transistor model will be the subjects

of future work.

4.8 Appendix

4.8.1 Solution of Dyson equation

The differential equation in section (4.3) can be solved using transfer matrix[62], or a straightforward boundary-condition matching. Consider the case $z' < 0$, for example. In each region we can write the solution as forward-moving and backward-moving waves:

$$D^r(z,z') = \begin{cases} be^{-i\tilde{k}z}, & z < z', \\ ce^{i\tilde{k}z} + de^{-i\tilde{k}z}, & z' < z < 0, \\ Ae^{i\tilde{k}z} + Be^{-i\tilde{k}z}, & 0 < z < d, \\ te^{i\tilde{k}z}, & d < z, \end{cases} \tag{4.57}$$

where we define the "wavevector" $\tilde{k} = \frac{\omega}{c} + i\eta$. Since we demand D^r to be a bounded function at $|z| \to \infty$, for $z < z'$ ($z > d$) the wave moves only backward (forward). The function is continuous at the points z', 0, and d where we have charges:

$$\begin{aligned} b\gamma' &= \frac{c}{\gamma'} + d\gamma', \\ c + d &= A + B, \\ A\lambda + \frac{B}{\lambda} &= t\lambda. \end{aligned} \tag{4.58}$$

We have defined the parameters $\lambda = e^{i\tilde{k}d}$, $\gamma' = e^{i\tilde{k}|z'|}$. The first derivatives need to be discontinuous so as to generate the Dirac delta functions on the right-hand side of the equation. This gives

$$\begin{aligned} \left(d\gamma' - \frac{c}{\gamma'} - b\gamma'\right)\Omega &= 1, \\ (B - A + c - d)\Omega &= (A + B)\Pi_0, \\ \left(A\lambda - \frac{B}{\lambda} - t\lambda\right)\Omega &= t\lambda\Pi_1. \end{aligned} \tag{4.59}$$

The six unknowns can be solved through these six linear equations.

For convenience of later calculations, we give here the solution of the Dyson equation for the two-dot case. They also degenerate to a one-dot or no dot case if we set $\Pi_1 \equiv \Pi_1^r(\omega)$ or Π_0 or both to zero. We note that the retarded Green's function is symmetric in space arguments, $D^r(z,z',\omega) = D^r(z',z,\omega)$. The matrix elements associated with the locations of two dots are:

$$\begin{aligned} D_{00} &= D^r(0,0,\omega) = \frac{(1-\lambda^2)\Pi_1 + 2\Omega}{\mathcal{D}}, \\ D_{01} &= D_{10} = D^r(0,d,\omega) = \frac{2\lambda\Omega}{\mathcal{D}}, \\ D_{11} &= D^r(d,d,\omega) = \frac{(1-\lambda^2)\Pi_0 + 2\Omega}{\mathcal{D}}, \end{aligned} \tag{4.60}$$

where we have defined

$$\mathcal{D} = (\lambda^2-1)\Pi_0\Pi_1 - 2\Omega\left(\Pi_0+\Pi_1\right) - 4\Omega^2. \tag{4.61}$$

For $-L/2 < z < 0$, the rest of the elements can be expressed in terms of D_{jk} $(j,k = 0,1)$. We have

$$\begin{aligned} D^r(z,-L/2,\omega) &= \frac{(\gamma^2-1)}{2\gamma\Omega}\delta + \gamma\delta D_{00}, \\ D^r(z,0,\omega) &= \gamma D_{00}, \\ D^r(z,d,\omega) &= \gamma D_{01}, \\ D^r(z,L/2,\omega) &= \frac{\gamma\delta}{\lambda} D_{01}, \end{aligned} \tag{4.62}$$

where we have defined $\gamma = e^{i\left(\frac{\omega}{c}+i\eta\right)|z|}$ and $\delta = e^{i\left(\frac{\omega}{c}+i\eta\right)L/2}$. For $0 < z < d$, we obtain

$$\begin{aligned} D^r(z,0,\omega) &= \left(\frac{\gamma^2-\lambda^2}{\gamma}\Pi_1 + 2\gamma\Omega\right)\frac{1}{\mathcal{D}}, \\ D^r(z,d,\omega) &= \Big((1-\gamma^2)\Pi_0 + 2\Omega\Big)\frac{\lambda}{\gamma\mathcal{D}}, \\ D^r(z,-L/2,\omega) &= D^r(z,0,\omega)\,\delta, \\ D^r(z,L/2,\omega) &= D^r(z,d,\omega)\,\frac{\delta}{\lambda}. \end{aligned} \tag{4.63}$$

For $d < z < L/2$, we have

$$\begin{aligned} D^r(z,-L/2,\omega) &= \frac{\gamma\delta}{\lambda}D_{01}, \\ D^r(z,0,\omega) &= \frac{\gamma}{\lambda}D_{01}, \\ D^r(z,d,\omega) &= \frac{\gamma}{\lambda}D_{11}, \\ D^r(z,L/2,\omega) &= \frac{(\gamma^2-\lambda^2)\delta}{2\gamma\lambda^2\Omega} + \frac{\gamma\delta}{\lambda^2}D_{11}. \end{aligned} \tag{4.64}$$

4.8.2 Scalar photon bath

We discuss here the bath spectrum of the scalar photon. As per standard procedures of open quantum systems, we need to partition the photon field into system and baths. Our strategy is to first discretize the photon to have recourse to the well-developed surface Green's function[64, 131]. We then take the continuum limit to obtain a bath spectrum of the photon field defined on a continuum.

Discretization of scalar photon field

In Sec. (4.2), when describing the photon Hamiltonian H_γ, we split the real line into three regions for the left bath in $(-\infty,-L/2]$, the central system in $[-L/2,L/2]$ and the right bath in $[L/2,\infty)$. However, given that the Hamiltonian is an integral on the line, it is not clear what the interaction between the bath and the central region is. For this reason, we consider a discretized version of the model by putting the problem on a 1D lattice with lattice constant a. The spatial derivative in potential energy thus becomes a finite difference, and the z integral becomes a discrete sum:

$$\begin{aligned} H_\gamma =& -s\int dz\frac{1}{2}\left[\dot{\phi}^2 + c^2\left(\frac{\partial\phi}{\partial z}\right)^2\right] \\ \longrightarrow& -\frac{s}{2}\sum_n a\left[\dot{\phi}_n^2 + c^2\left(\frac{\phi_{n+1}-\phi_n}{a}\right)^2\right]. \end{aligned} \tag{4.65}$$

Similar to phonon on a lattice, we set $x = j\cdot a$ and $\phi_j = \frac{1}{\sqrt{sa}}u_j$. Continuum limit is recovered for $a\to 0$. Putting a "spring constant" $k = \frac{c^2}{a^2}$, we find a discretized photon

Hamiltonian[131]:

$$H_0 = -\sum_n \frac{1}{2}\dot{u}_n^2 - \frac{1}{2}k\sum_n (u_{n+1} - u_n)^2, \tag{4.66}$$

which has the same form as a phonon Hamiltonian (except for the minus sign). For the equation of motion of u_n we have:

$$\ddot{u}_n = k(u_{n+1} - 2u_n + u_{n-1}), \tag{4.67}$$

which also follows from a direct discretization of the wave equation $\frac{\partial^2\phi}{\partial t^2} = c^2\frac{\partial\phi}{\partial x^2}$. Eq. (4.67) can be solved by setting:

$$u_n = A\lambda^n e^{-i\omega t}. \tag{4.68}$$

Putting $\omega \to \omega + i\tilde{\eta}$ (for regularization) and $\lambda = e^{iq\cdot a}$, we find the dispersion relation for the discretized photon field:

$$(\omega + i\tilde{\eta})^2 = 2k[1 - \cos(q\cdot a)]. \tag{4.69}$$

In the continuum limit $a \to 0$, the above reads $\omega + i\tilde{\eta} = \pm c\cdot q$, recovering the free photon dispersion relation in continuum.

Using the discretized photon quadrature operator u_j, we define the decoupled retarded Green's function as:

$$\check{d}^r_{jk}(\omega) = -\frac{i}{\hbar}\int_0^\infty dt e^{i\omega t}\langle[u_j(t), u_k(0)]\rangle_{H_0}, \tag{4.70}$$

where H_0 is the unperturbed free photon Hamiltonian. Its relation to the usual one defined on a continuum, namely:

$$d^r(x, x', \omega) = -\frac{i}{\hbar}\int_0^\infty dt e^{i\omega t}\langle[\phi(x,t), \phi(x',0)]\rangle_{H_0}, \tag{4.71}$$

is given by:

$$d^r(x, x', \omega) = \lim_{a \to 0} \frac{1}{sa} \check{d}^r_{jk}(\omega), \tag{4.72}$$

where $j \cdot a$ and $k \cdot a$ correspond respectively to x and x'.

self-energy of scalar photon bath

Consider a semi-infinite chain of discretized photons, labeled by $j = -1, -2, \cdots$. We derive the surface Green's function of this system by attaching a new site $j = 0$ to the right-most site $j = -1$. The retarded Green's function (4.70), when regarded as an infinite matrix, satisfies the following equations:

$$[(\omega + i\tilde{\eta})^2 - \widetilde{K}]\check{d}^r = -I, \tag{4.73}$$

where I is the identity matrix (the minus sign originates from the unusual commutation relation $[u_j, \dot{u}_k] = -\delta_{jk}$), and $\widetilde{K}$ is an infinite tridiagonal matrix given by:

$$\widetilde{K} = \begin{bmatrix} 2k & -k & & \\ -k & 2k & -k & \\ & -k & 2k & \ddots \\ & & \ddots & \ddots \end{bmatrix}. \tag{4.74}$$

Focusing on the first column of the right-hand side of (4.73), we find a system of difference equations:

$$k\check{d}^r_{j-1,0} + [(\omega + i\tilde{\eta})^2 - 2k]\check{d}^r_{j,0} + k\check{d}^r_{j+1,0} = 0, j = -1, -2, \cdots \tag{4.75}$$

with boundary condition:

$$[(\omega + i\tilde{\eta})^2 - 2k]\check{d}^r_{0,0} + k\check{d}^r_{-1,0} = -1. \tag{4.76}$$

To solve (4.75) and (4.76), consider the ansatz $\check{d}^r_{j,0} = \alpha\lambda^j$, where $j = 0, -1, -2, \cdots$, which gives the quadratic equation:

$$k\lambda^{-1} + [(\omega + i\tilde{\eta})^2 - 2k] + k\lambda = 0. \tag{4.77}$$

This equation admits two roots: $\lambda_<, \lambda_>$ with $|\lambda_<| < 1$ and $|\lambda_>| > 1$. We choose the second root so that $\check{d}^r_{j,0}$ goes to zero for $j \to -\infty$. Using the boundary condition (4.76), we find $\alpha = 1/(k\lambda_>)$ and hence $\check{d}^r_{j,0} = \lambda_>^{j-1}/k$.

Next, we consider attaching the first system site $j = 1$ to the semi-infinite chain (Fig. (4.10)).

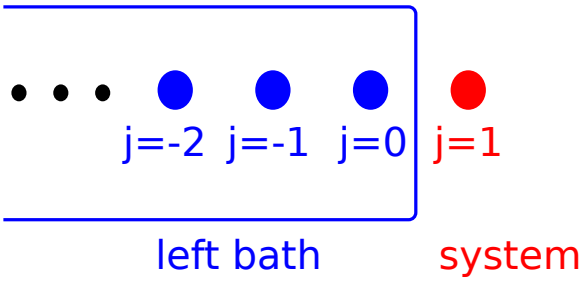

Fig. 4.10: Derivation of discretized photon bath self-energy. Attaching the first system site $j = 1$ to the semi-infinite left bath $j = 0, -1, -2, \cdots$ leads to the identification of bath self-energy, Eq. (4.79), from the Dyson equation describing the coupling.

This coupling can be described by a Dyson equation:

$$\begin{bmatrix} \check{D}^r_{11} & \check{D}^r_{01} \\ \check{D}^r_{10} & \check{D}^r_{00} \end{bmatrix} = \begin{bmatrix} \check{d}^r_{11} & 0 \\ 0 & \check{d}^r_{00} \end{bmatrix} + \begin{bmatrix} \check{d}^r_{11} & 0 \\ 0 & \check{d}^r_{00} \end{bmatrix} \begin{bmatrix} 0 & k \\ k & 0 \end{bmatrix} \begin{bmatrix} \check{D}^r_{11} & \check{D}^r_{01} \\ \check{D}^r_{10} & \check{D}^r_{00} \end{bmatrix}, \tag{4.78}$$

where the $\check{D}^r$'s denote the discretized retarded photon Green's functions that result from coupling the left bath to site $j = 1$. From the equation for $\check{D}^r_{11}$, one identifies the left photon bath self-energy $\check{\Pi}^r_L$:

$$\check{D}^r_{11} = [(\check{d}^r_{11})^{-1} - \underbrace{(k\check{d}^r_{00}k)}_{\check{\Pi}^r_L}]^{-1}. \tag{4.79}$$

Hence, we find:

$$\check{\Pi}_L^r = k\check{d}_{00}^r k = k\lambda_<, \tag{4.80}$$

where we used the fact that $\lambda_>\lambda_< = 1$ in view of the quadratic equation (4.77), which can be solved (up to second order in a) by:

$$\begin{aligned} \lambda_< &= e^{i(\frac{\omega}{c}+i\tilde{\eta})a}, \\ \lambda_> &= e^{-i(\frac{\omega}{c}+i\tilde{\eta})a}. \end{aligned} \tag{4.81}$$

Armed with the retarded left photon bath self-energy, we find the lesser self-energy using the fluctuation-dissipation relation:

$$\check{\Pi}_L^< = N_L[\check{\Pi}_L^r - \check{\Pi}_L^a] \approx N_L k \left[2ia\frac{\omega}{c}\right]. \tag{4.82}$$

Finally, using the relation between discretized and continuum Green's functions, Eq. (4.72), we obtain for the left photon bath:

$$\Pi_L^< = \lim_{a\to 0} sa\check{\Pi}_L^< = 2isc\omega N_L = 2\Omega N_L, \tag{4.83}$$

where $\Omega = isc^2(\frac{\omega}{c} + i\eta) = i\epsilon_0 A(\frac{\omega}{c} + i\eta)$ as in the main text, and a damping factor η has been added.

Meir-Wingreen formula for the scalar photon bath

Lastly, we comment on the validity of the usual Meir-Wingreen formula. Since we have in hand a negative definite Hamiltonian for the scalar photon, a sign-flip is apparently needed compared to the usual case of positive definite bath Hamiltonian. However, a similar sign flip occurs for the Green's functions D, Π. Thanks to the symmetrical combination of the Green's functions ($D^<\Pi^>$ or $D^>\Pi^<$) in the integrand for current, the minus sign is canceled, allowing the usual Meir-Wingreen formula to remain intact without any sign-flip needed.

4.8.3 Matsubara sum formula for photon self energies due to electrons

Under the local equilibrium approximation, the polarization diagram, i.e. Eq. (4.48) for the photon self-energy, can be calculated exactly. In frequency domain, Eq. (4.48) becomes:

$$\Pi_j^r(\omega) = -i\hbar Q^2 \int_{-\infty}^{+\infty} \frac{d\omega'}{2\pi} \left[G_j^r(\omega') G_j^<(\omega' - \omega) + G_j^<(\omega') G_j^a(\omega' - \omega) \right]. \tag{4.84}$$

This integral can be performed by closing a contour using the residue theorem. Writing $E = \hbar\omega$, under the wide-band limit for electron bath we find:

$$\Pi_j^r(E) = Q^2 \Bigg\{ \frac{i\Gamma_j [f(v_j + i\frac{\Gamma_j}{2} + E) - f(v_j + i\frac{\Gamma}{2})]}{(E + i\Gamma_j)E} - \sum_{n=0}^{\infty} \frac{ik_B T \Gamma_j}{(\mu_j - v_j + i\hbar\omega_n)^2 + \frac{\Gamma_j^2}{4}} \times \Big(\frac{1}{\mu_j - v_j + i\hbar\omega_n + E + i\frac{\Gamma_j}{2}} + \frac{1}{\mu_j - v_j + i\hbar\omega_n - E - i\frac{\Gamma_j}{2}} \Big) \Bigg\}, \tag{4.85}$$

where $f(E) = 1/[\exp(\frac{E-\mu}{k_B T}) + 1]$ is the Fermi function, and $\omega_n = (2n+1)\pi k_B T/\hbar$ is the Matsubara frequency.

4.8.4 Consistence between FE and NEGF

In this subsection, we give a connection between FE and NFGF calculation. During the derivation of FE calculation for RHT, the important statistical correlation function is the use of fluctuation-dissipation theory for current-current relation, i.e.:

$$\langle j_\mu(\vec{r}_1, \omega) j_v^*(\vec{r}_2, \omega') \rangle = \frac{4}{\pi} \epsilon''(\omega) \hbar\omega^2 \left[\frac{1}{e^{\hbar\omega/kT} - 1} + \frac{1}{2} \right] \delta(\omega - \omega') \delta(\vec{r}_1 - \vec{r}_2) \delta_{\mu v} \tag{4.86}$$

To clarify the connection between two methods, we calculate the current-current correlation through NFGF. For scalar photon, we need to change the current-current correlation into charge-charge correlations. For the self-energy calculation of photon, we use the

loop diagram and can be defined as below:

$$\Pi_{\mu v}(\vec{r}_1,\tau_1,\vec{r}_2,\tau_2) = -\frac{i}{\hbar}\left\langle T_\tau j_\mu(\vec{r}_1) j_v(\vec{r}_2,\tau_2)\right\rangle \tag{4.87}$$

Where $\mu, v = x, y, z$ corresponds to direction components of self-energy. $\tau_{1,2}$ are Keldysh contour time. The position vector $\vec{r}$ can be separated as left part and right part and we assume that the current of two part is uncorrelated, i.e. $\langle j^L j^R\rangle = 0$. The $\langle j^L(\vec{r}_1,\tau_1,\vec{r}_2,\tau_2) j^L(\vec{r}_1,\tau_1,\vec{r}_2,\tau_2)\rangle$ and $\langle j^R, j^R\rangle$ should be obtain. For the left part of photon self-energy, we have:

$$\Pi^L_{\mu v}(\vec{r}_1,\tau_1,\vec{r}_2,\tau_2) = -\frac{i}{\hbar}\left\langle T_\tau j^L_\mu(\vec{r}_1) j^L_v(\vec{r}_2,\tau_2)\right\rangle \tag{4.88}$$

Under local equilibrium approximation, i.e. left part and right part are equilibrium with T_L and T_R, we have the fluctuation-dissipation theorem. It is reasonable approximation when the electron-photon coupling strength is weak. Then we use the LEA for the calculation of photon self energy component in real time:

$$\Pi^{L>}_{\mu v}(\vec{r}_1,\vec{r}_2,\omega) = [1+N_L(\omega)][\Pi^{Lr}_{\mu v}(\vec{r}_1,\vec{r}_2,\omega) - \Pi^{La}_{\mu v}(\vec{r}_1,\vec{r}_2,\omega)] \tag{4.89}$$

$$\Pi^{L<}_{\mu v}(\vec{r}_1,\vec{r}_2,\omega) = N_L(\omega)[\Pi^{Lr}_{\mu v}(\vec{r}_1,\vec{r}_2,\omega) - \Pi^{La}_{\mu v}(\vec{r}_1,\vec{r}_2,\omega)] \tag{4.90}$$

Generally, the retarded photon self energy can be related to the optical conductivity $\sigma_{\mu v}(\omega)$ by the linear response theory of Kubo.

$$\Pi^{Lr}_{\mu v}(\vec{r}_1,\vec{r}_2,t) = -\frac{i}{\hbar}\theta(t)\left\langle[j^L_\mu(\vec{r},t), j^L_v(\vec{r}_2,0)]\right\rangle \tag{4.91}$$

$$\Pi^{Lr}_{\mu v}(\vec{r}_1,\vec{r}_2,\omega) = \int dt e^{i\omega t}\Pi^{Lr}_{\mu v}(\vec{r}_1,\vec{r}_2,t) \tag{4.92}$$

$$\sigma^L_{\mu v}(\omega) = -\frac{e^2}{i\omega V}\left\langle\tau_{\mu v}\right\rangle - \frac{1}{i\omega V}\int_0^\infty \frac{1}{i\hbar}[J^L_\mu(t), J^L_v(0)]e^{i\omega t}dt \tag{4.93}$$

$$= -\frac{e^2}{i\omega V}\left\langle\tau_{\mu v}\right\rangle - \frac{1}{i\omega V}\int d\vec{r}_1^3\int d\vec{r}_2^3\Pi^{Lr}_{\mu v}(\vec{r}_1,\vec{r}_2,\omega) \tag{4.94}$$

$$\sigma^L_{\mu v}(\vec{r}_1,\vec{r}_2,\omega) \approx \frac{ie^2 n}{m\omega}\delta_{\mu v} - \frac{V}{i\omega}\Pi^{Lr}_{\mu v}(\vec{r}_1,\vec{r}_2,\omega) \tag{4.95}$$

$$\epsilon(\omega) = 1 + \frac{i\sigma(\omega)}{\epsilon_0\omega} \tag{4.96}$$

Then we get the connection between retarded photon self energy and dielectric constant:

$$\epsilon^L_{\mu v}(\vec{r}_1,\vec{r}_2,\omega) = 1 - \frac{e^2 n}{\epsilon_0 m\omega^2} - \frac{V}{\epsilon_0\omega^2}\Pi^{Lr}_{\mu v}(\vec{r}_1,\vec{r}_2,\omega) \tag{4.97}$$

$$\mathrm{Im}\Pi^{Lr}_{\mu v}(\vec{r}_1,\vec{r}_2,\omega) = -\frac{\epsilon_0\omega^2}{V}\epsilon''_{\mu v}(\vec{r}_1,\vec{r}_2,\omega) \tag{4.98}$$

Under random phrase approximation or local approximation, we have:

$$\frac{\epsilon''_{\mu v}(\vec{r}_1,\vec{r}_2,\omega)}{V} = \epsilon''(\omega)\delta_{\mu v}\delta^3(\vec{r}_1-\vec{r}_2) \tag{4.99}$$

If the dielectric constant is homogeneous in $x-y$ direction, we can simplify the notation and only consider the z direction. The lesser photon self energy under local equilibrium for both left and mid can be written by fluctuation dissipation relation.

$$\Pi^{>}_{\mu v}(z,\omega) = \begin{cases} -2i\omega^2[1+N_L(\omega)]\epsilon_0\epsilon''^L(z,\omega) & z\ in\ left, \\ 0 & z\ in\ vaccum \\ -2i\omega^2[1+N_R(\omega)]\epsilon_0\epsilon''^R(z,\omega) & z\ in\ right \end{cases} \tag{4.100}$$

The Poynting vector can be calculated from lesser Green's function.

$$\begin{aligned} \langle S_z\rangle =& \frac{1}{\mu_0}\int_{-\infty}^{+\infty}\frac{d\omega}{2\pi}\hbar\omega\left(-\frac{\partial}{\partial z'}\right)\sum_{\alpha=x,y} D^{>}_{\alpha\alpha}(\vec{r}_1,\vec{r}_2,\omega) \\ =& \frac{1}{\mu_0}\int_{-\infty}^{+\infty}\frac{d\omega}{2\pi}\hbar\omega\left(-\frac{\partial}{\partial z'}\right)\sum_{\alpha=x,y}\int\frac{dq_\perp^2}{(2\pi)^2}dzdz'\times \\ & \sum_{\mu v=x,y,z} D^r_{\alpha\mu}(\perp,\omega,z,z')\Pi^{>}_{\mu v}(q_\perp,\omega,z,z')D^a_{v\alpha}(q_\perp,\omega,z,z') \\ =& \int_{-\infty}^{+\infty}\frac{d\omega}{2\pi}\hbar\omega\left\{[T_L(\omega)N_L(\omega)-T_R(\omega)N_R(\omega)]+[T_L(\omega)-T_R(\omega)]\right\} \\ =& \int_{-\infty}^{+\infty}\frac{d\omega}{2\pi}\hbar\omega[N_L(\omega)-N_R(\omega)]T(\omega) \end{aligned} \tag{4.101}$$

Where $T(\omega) = T_{L(R)}(\omega)$ is:

$$T(\omega) = T_{L(R)}(\omega) = \left(-\frac{2i\epsilon_0\omega^2}{\mu_0 V}\right)\left(-\frac{\partial}{\partial z'}\right)\sum_{\alpha=x,y}\sum_{\mu v=x,y,z} D^r_{\alpha\mu}(q_\perp,\omega,z,z')\epsilon^{L(R)\prime\prime}_{\mu v}(\omega)D^a_{v\alpha}(q_\perp,\omega,z,z') \tag{4.102}$$

Where we have $T_L(\omega) = T_R(\omega)$ due to the detail balance. So we get a Landauer-type expression for the Poynting vector. When we obtain the multiple reflection of photon and get the explicit expression for the transmission, we can obtain the same formula as previous results. The scalar photon derivation is similar as the derivation of vector photon if we change the current-current correlation as charge-charge correlation. In our work, we focus on the scalar photon part due to it is can be connected to the Coulomb interaction which is not paid much attention in the RHT research area.

Chapter 5

Radiative quantum thermal rectifier and transistor

"Only those who attempt the absurd can achieve the impossible."

—Albert Einstein

5.1 Introduction

In the last century, electricity management and electricity logic device have been achieved by the two important components: the diode and the transistor[146]. The electric diode is a two-terminal electronic component. This device has low resistance to the current in one direction and high resistance in the reverse direction. The electronic transistor consists of the drain, the source, and the gate. The electron current between source and drain can be controlled by the changing of gate voltage. In a electric transistor, a small change of gate voltage will lead to a large change of source and drain current. In the last two decades, by analogy with electricity management and electricity logic device, researchers developed the similar thermal logical devices to control the heat easier. Similar to electric diode, people have focused on the thermal rectifiers which have the asymmetric heat current when the temperature is inverted. Analogically, the thermal transistor can be designed through phononic and electronic thermal transport[55].

Recently, due to the special properties of thermal radiative heat transport, the thermal rectifiers and thermal transistors can be investigated theoretically in near-field or far-field region[12, 13, 53, 147, 148]. To achieve the properties of the thermal transistor, the researchers have to involve the phase change materials[13]. However, different with electricity logic device, such radiative thermal logical devices have very large cross areas to enhance the radiative heat current, which is not convenient for integration.

At the same time, the development of quantum systems has also been used for the photon rectifiers and transistors in the last two decades. The radiative heat current between quantum systems is slightly different with previous radiative heat current calculation based on fluctuation electrodynamics. Very recently, Joulain et.al demonstrate a quantum thermal transistor through three coupled two-level system using quantum master equation approach[14]. But the configuration of such quantum thermal device is difficult to achieve experimentally. In this section, we combine with our previous capacitor physics results and numerically demonstrate a quantum thermal rectifier and transistor through scalar field photon, which in principle is more achievable in experiments.

5.2 Method

The method used in this section is the same as that in Chapter 4. So in this part, we only briefly show the schematic calculation process in Fig. (5.1) and detailedly show how to construct a non-linear heat bath which is not mentioned as before. For the actual thermal rectifier calculation, we use the self-consistence Born approximation, which is similar to the GW method for optical conductivity calculation. However, for the radiative quantum thermal transistor calculation, we use the local equilibrium approximation for simplicity. It is a good approximation when the system is weakly coupled with the heat bath.

The RHT between dots can be calculated though previous "Poynting scalar" formula,

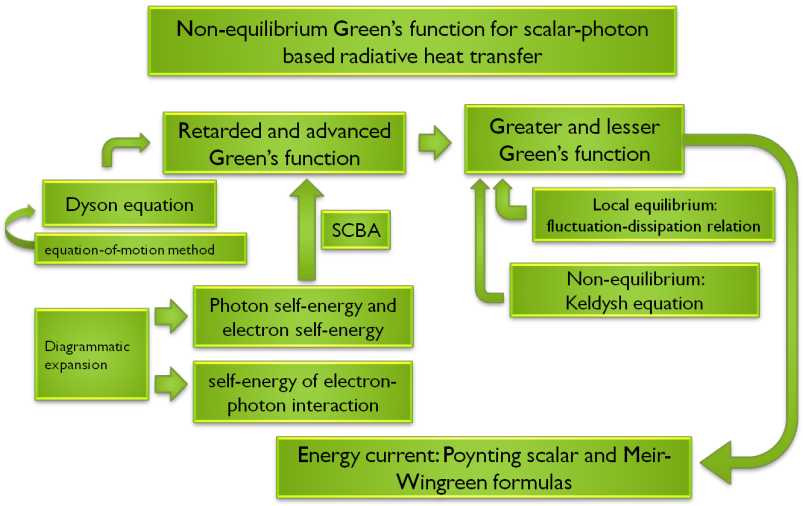

Fig. 5.1: Schematic calculation process for near-field radiative heat transfer based on the non-equilibrium Green's functions.

i.e.:

$$\langle j(z)\rangle = \epsilon_0 \int_0^\infty \frac{d\omega}{\pi} \hbar\omega \mathrm{Re}\, \frac{\partial D^{>}(\omega, z, z')}{\partial z'}\bigg|_{z'=z}. \tag{5.1}$$

Where we shall refer to the integrand in Eq. (5.1) as the "spectral transfer function".

The NEGF method is a formalism from the view of quantum field theory. For the purpose of constructing a radiative quantum thermal transistor, the FE method is not suitable because it is not easy to find the corresponding dielectric constant for the quantum system, especially for the small size quantum system. From the quantum field view, the dissipation part of the energy is related to the self-energy of a quantum system. To solve that, we need the quantum field technique. This is why our method for radiative heat transfer in nanoscale is important for this research area.

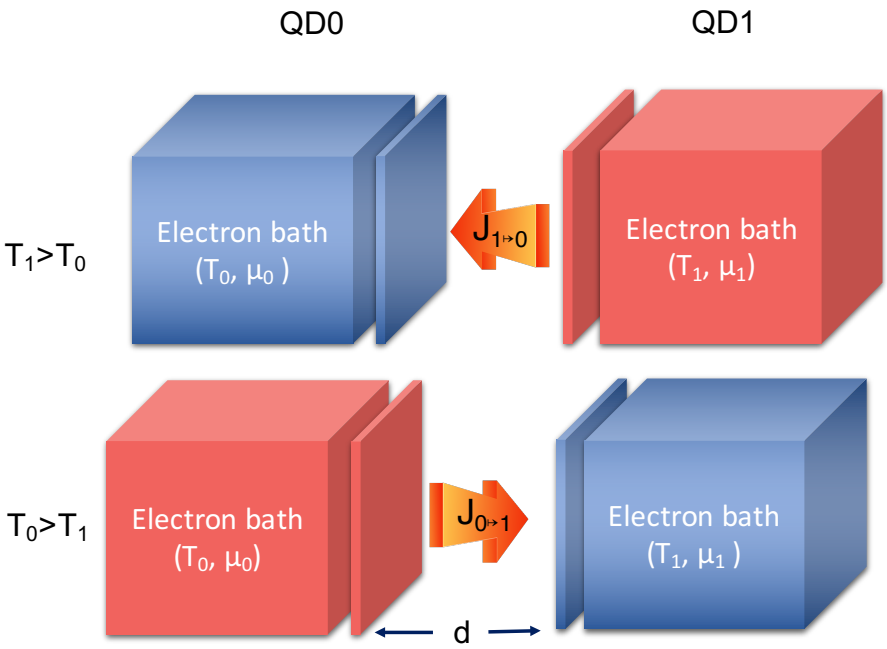

Fig. 5.2: Sketch of thermal rectifier

5.3 Scalar-photon-based thermal rectifier

Thermal rectification is a phenomenon in which the heat flux depends on the sign of the temperature difference of two bodies. In the literature, a vast majority of the previous works focuses on geometry or phonon-induced rectification[12, 53, 55, 149, 150]. While not much has been done on voltage-controlled thermal rectification, our simple two-dot model is suitably tailored for that. Therefore, we discuss in this paragraph the tunability of thermal rectification via chemical potential. Fig. (5.2) shows the schematic sketch for the thermal rectifier based on two quantum dots. To quantify the strength of thermal rectification, we define the rectification constant:

$$R = \frac{J_{0\to1} - J_{1\to0}}{J_{1\to0}}, \tag{5.2}$$

where $J_{i\to j}$ is the radiative heat current from system i to system j. The temperature difference has the same magnitude but opposite sign to $J_{0\to1}$ and $J_{1\to0}$.

Fig. 5.3 shows the chemical potential dependence of rectification strength. For simplicity, we set the same chemical potential for both dots. Within experimentally-

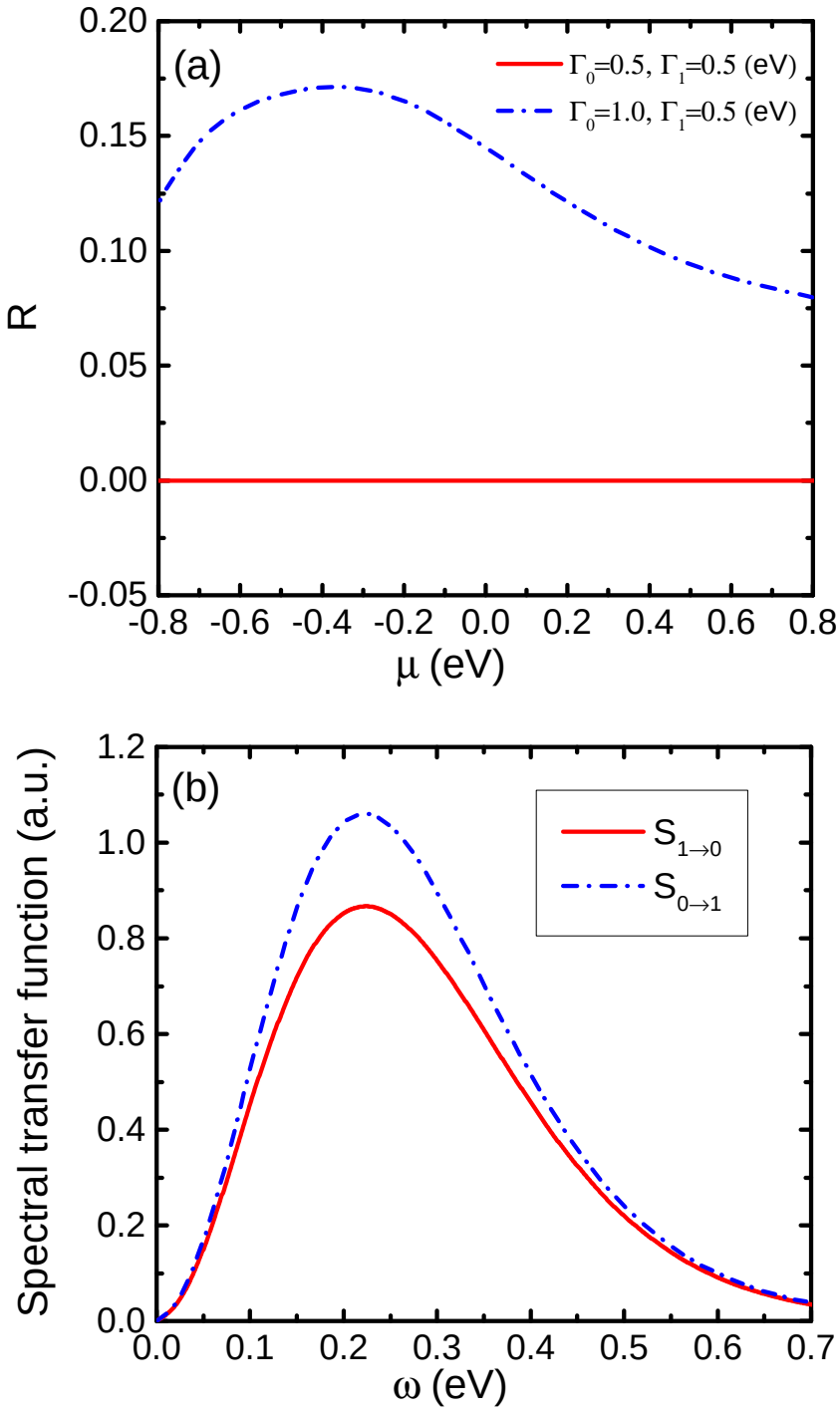

Fig. 5.3: Thermal rectification effects. (a) Rectification constant as a function of the chemical potential of the quantum dots, with both dots having the same chemical potential. (b) Spectral transfer function of two quantum dots with switched temperature. The chemical potential of two quantum are set as -0.4 eV. In above two figures, the temperatures are set at 1000 K and 300 K. Distance between the two quantum dots is set as 19.2 nm. $Q = 1e$.

accessible parameter regimes, i.e., -0.8 eV to 0.8 eV, the rectification constant varies from 0.08 to 0.17, and is maximized at -0.4 eV. On the other hand, the heat flux is very small when the chemical potential is greater than 1.0 eV or smaller than -1.0 eV. Such parameter regime corresponds to a highly occupied or unoccupied electron level, both indicating the lack of carriers for heat flux generation. One can also study rectification by means of the spectral transfer function. In Fig. 5.3(b), the blue dash-dot ($S_{0\to1}$) and red solid line ($S_{1\to0}$) have the same peak position at 0.22 eV but different maxima. In the wide-band limit for the electron bath, the value Γ, which determines the dot-bath coupling, is set at 1 eV for dot 0 and 0.5 eV for dot 1. Both parameters are in the strong-coupling regime, so the energy flux from electron bath to the dot depends greatly on the coupling strength. Due to the asymmetric coupling, the electron hopping to the dots are different so that the temperature response of the dots are effected and the rectification effects can be found in that condition. On the contrary, if two dots have symmetry electron bath coupling, we can not find the rectification effects in the red line in figure (5.3a).

5.4 Radiative quantum thermal transistor

5.4.1 Sketch of radiative quantum thermal transistor

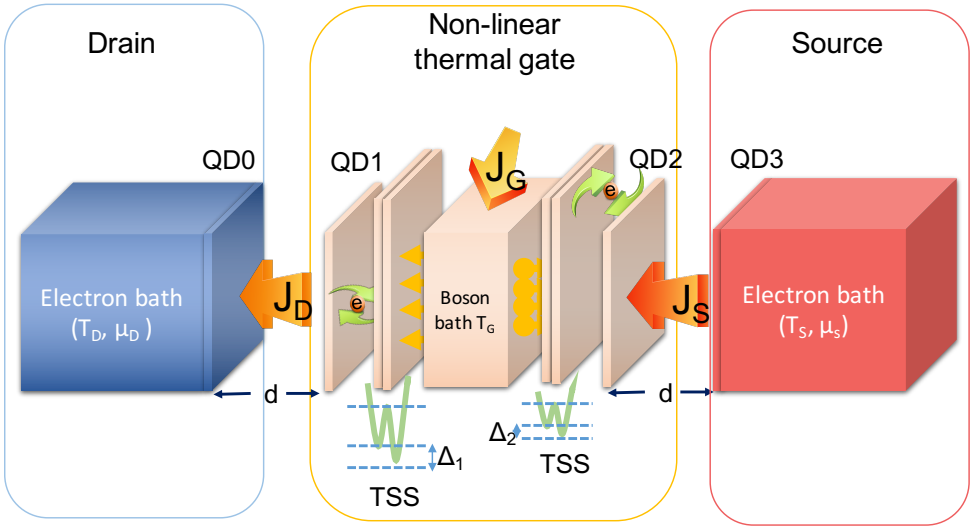

Fig. 5.4: schematic sketch of the radiative quantum thermal transistor

Fig. (5.4) shows the schematic sketch of the radiative quantum thermal transistor. In this model, we consider four quantum dots, i.e. the QD 0 and QD 3 are regarded as the drain and source of the transistor, the QD 1 and QD 2 coupling to the non-linear thermal bath, which is consisted with two states system (TSS) and the boson bath, is considered as the thermal gate of the transistor. The radiative heat flux can be transfer from the QD 3 to QD 2 through Coulomb interaction but can not transfer from the QD 3 to QD 0 directly. Where J_S is the heat current from source to gate, J_D is the heat current from gate to drain, and J_G is heat current take into the gate from gate bath.

5.4.2 Non-linear quantum thermal environments

As shown in the previous Chapter, the wide-band approximation is always used for our electron bath calculation, and the bath is assumed as a half-infinite chain of harmonic oscillators. For some normal cases, such approximation can keep consistency with actual systems. However, Fig. (5.5) shows the actual calculations for thermal transistor with a linear thermal gate bath. Due to the "normal" properties of the linear bath, we can not build a thermal transistor with such linear gate. So, due to the special properties of the thermal transistor, a non-linear heat bath gate, i.e., a temperature dependent thermal gate, is really needed for switching, modulating and amplifying heat current. In this section, we discuss the construction of a non-linear thermal bath.

Model hamitonian of the non-linear thermal bath

At first, we regard a single level quantum dot as our system, which can be explained as a nanoscale disk with possible charge of 0 or Q. Our single level system is coupled to a two-state system (TSS), such as a unsymmetric double-well quantum oscillator which is assumed that only two lowest energy states are populated and the energy difference Δ between two ground states is much smaller than the higher transition energy. And the TSS is coupled to a linear boson bath. As seen from our single level system, the TSS+(linear boson bath) can be consider as a non-linear bath because the anharmonicity of a TSS and the linear bath can guarantee the whole system is a nonlinear

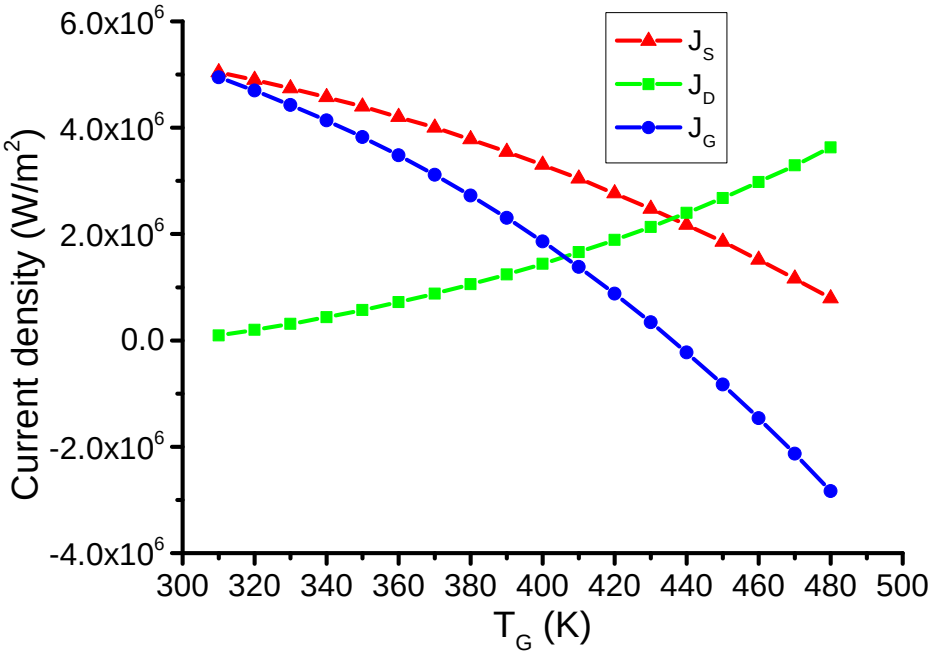

Fig. 5.5: Transistor with a linear bath gate. Current density of source, drain and gate as a function of gate temperature. The distances between gate, source and drain d is set as 18 nm. The temperature of source T_S is 500 K and the corresponding temperature for drain T_D is 100 K. Γ_1 equals 1 eV and Γ_2 equals to 0.5 eV. Chemical potential and site energy are all set to zero.

system and a thermal reservoir. As shown in Fig. (5.3), the total Hamiltonian of the system with a non-linear thermal bath can be written as below in the rotating-wave approximation[151, 152]:

$$H = vc^{\dagger}c + \eta\sigma_x(c^{\dagger} + c) + \frac{\Delta}{2}\sigma_z + \sum_k [\omega_k a_k^{\dagger} a_k + \lambda\sigma_x(a_k^{\dagger} + a_k)]. \tag{5.3}$$

Where v is the site energy of quantum dot. c and $c^{\dagger}$ are the annihilation and creating operator of electron and it satisfies anticommutation relation. $d_{1(2)}$ and $d_{1(2)}^{\dagger}$ are the annihilation and creating operator of TSS and subscript $1(2)$ corresponds to ground(excited) state. For convenience, the Pauli matrix is used to describe the properties of the TSS. $\sigma_{x,y,z}$ is the Pauli matrix. $\sigma^{\pm} = \frac{1}{2}(\sigma_x \pm i\sigma_y)$ and it can be also rewritten as: $\sigma^{+} \to d_2^{\dagger}d_1, \sigma^{-} \to d_1^{\dagger}d_2$. Δ is the energy gap of TSS. η is the coupling between the quantum dot and TSS. The second term of the Hamiltonian corresponds to standard electron hoping between quantum dot and TSS. a_k and $a_k^{\dagger}$ is the annihilation

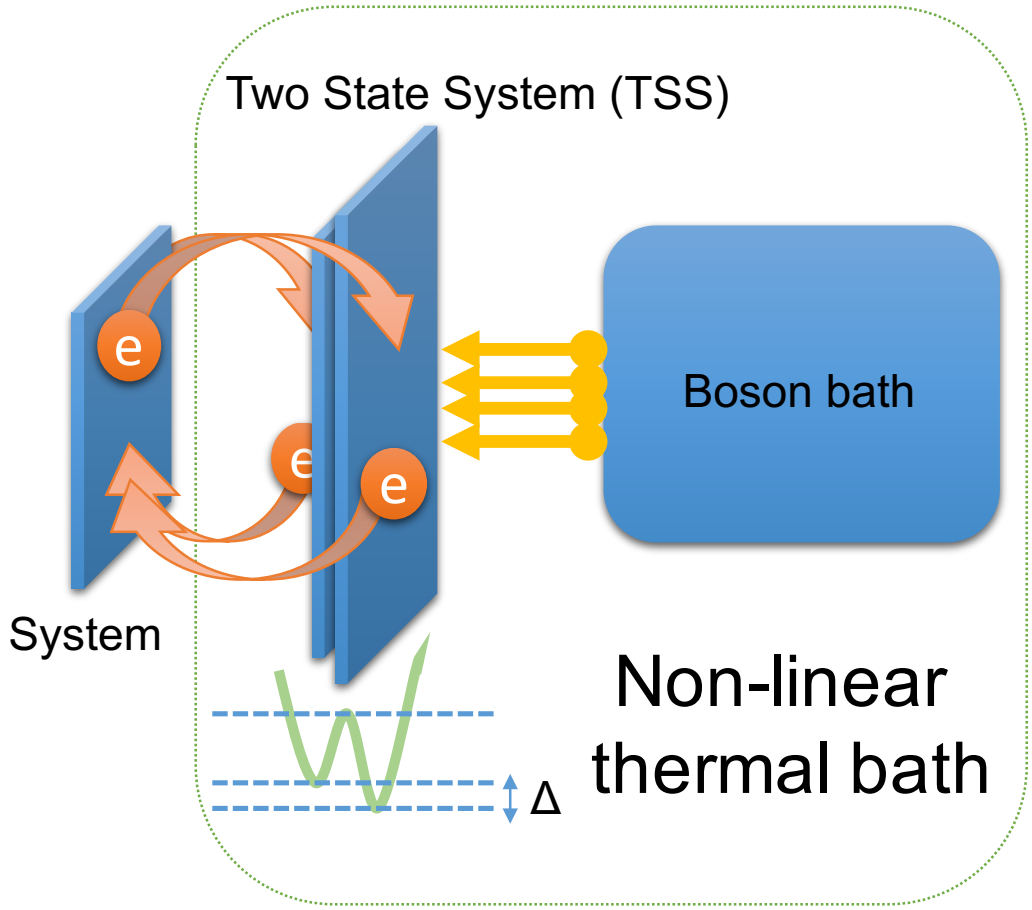

Fig. 5.6: schematic sketch of nonlinear heat bath: a single level quantum dot coupled with asmmentric double quantum well

and creating operator of boson bath and it satisfies commutation relation. λ is the coupling between TSS and boson bath.

In Eq. (5.3), if we get rid of the system and system-TSS coupling terms, the left Hamiltonian is the same as the normal spin-boson model[153, 154]. This is the logic sketch to build a non-linear thermal bath: the normal heat bath coupled to a non-linear harmonic oscillator. When turning on the coupling between system and TSS, the overall system i.e. TSS+(boson bath) behaves like non-linear thermal bath. Such system can be achieved experimentally[155–159]. For example, Eq. (5.3) can be achieved by attaching a graphene sheet to a double quantum well (DQW) with exciton gas. The attached graphene sheet acts as 2d electron gas which can interact with the photon and transfer radiative heat to drain or source. The DQW and exciton gas act as a nonlinear thermal bath which can change the optical properties of attached graphene sheet and

radiative heat flux can be controlled by the temperature of such non-linear thermal bath. However, It is difficult to find a dielectric constant to describe the optical properties of such multicomponent system. That means the normal fluctuation electrodynamics is not a reasonable method to calculate radiative heat flux. Our previous NEGF method is needed for such quantum system.

Green's function of the TSS-boson model

The final goal of this section is to calculate the self-energy of the non-linear thermal bath. According to the procedure of surface Green's function calculation, we need to compute the Green's function of the TSS-boson thermal bath at first. As usual, the Green's function of the TSS can be defined as below and we set $t' = 0$ for simplicity.

$$\begin{aligned} G^{>}(t, t' = 0) &= -\frac{i}{\hbar}\langle \sigma^{-}(t)\sigma^{+}(0)\rangle, \\ G^{<}(t, t' = 0) &= -\frac{i}{\hbar}\langle \sigma^{+}(0)\sigma^{-}(t)\rangle, \\ G^{r}(t, t' = 0) &= -\frac{i}{\hbar}\theta(t - t')\langle\{\sigma^{-}(t), \sigma^{+}(0)\}\rangle. \end{aligned} \tag{5.4}$$

At first, we turn off the dot-nonlinear-bath coupling i.e. $\eta = 0$. In that condition, the master equation method can be used for Eq. (5.3). In the interaction picture and thermal equilibrium, we can write the master equation as below[151]:

$$\begin{aligned} \frac{d\rho^I}{dt} =& -\gamma(1 + \bar{n})(\sigma^{+}\sigma^{-}\rho^I + \rho^I\sigma^{+}\sigma^{-} - 2\sigma^{-}\rho^I\sigma^{+}) \\ & -\gamma\bar{n}(\sigma^{-}\sigma^{+}\rho^I + \rho^I\sigma^{-}\sigma^{+} - 2\sigma^{+}\rho^I\sigma^{-}), \end{aligned} \tag{5.5}$$

Where $\bar{n} = \frac{1}{e^{\Delta/k_BT}-1}$ is the expectation value of $\langle a_k^{\dagger}a_k\rangle$. γ is a constant coefficient that depends on TSS-Boson bath coupling λ. In above equation, we have neglect the Lamb shifted term. In Schrödinger picture, we can rewrite the master equation as below:

$$\frac{d\rho^s}{dt} = \frac{d\rho^I}{dt} - i\frac{\Delta}{2}[\sigma_z, \rho^s]. \tag{5.6}$$

The state coherence $\langle\sigma^-\rangle, \langle\sigma^+\rangle$ follow the equation:

$$\begin{aligned}\frac{d}{dt}\langle\sigma^-\rangle =& (-i\Delta - \gamma(1+2\bar{n}))\langle\sigma^-\rangle.\\ \frac{d}{dt}\langle\sigma^+\rangle =& (i\Delta - \gamma(1+2\bar{n}))\langle\sigma^+\rangle.\end{aligned} \tag{5.7}$$

The solution of above atomic coherence can be written as below (matching the boundary condition i.e. decay at $t \to \pm\infty$):

$$\begin{aligned}\langle\sigma^-(t)\rangle =& e^{-[i\Delta t+\gamma(1+2\bar{n})|t|]}\langle\sigma^-(0)\rangle,\\ \langle\sigma^+(t)\rangle =& e^{-[-i\Delta t+\gamma(1+2\bar{n})|t|]}\langle\sigma^+(0)\rangle.\end{aligned} \tag{5.8}$$

The real time Green's function defined in Eq. (5.4) can be calculated from Eq. (5.8) with quantum regression theorem. For simplify, we set $t' = 0$.

$$\begin{aligned}G^>(t,0) =& -\frac{i}{\hbar}\langle\sigma^-(t)\sigma^+(0)\rangle\\ =& -\frac{i}{\hbar}e^{-\gamma(1+2\bar{n})|t|}e^{-i\Delta t}\langle\sigma^-(0)\sigma^+(0)\rangle,\\ G^<(t,0) =& -\frac{i}{\hbar}\langle\sigma^+(0)\sigma^-(t)\rangle\\ =& [\frac{i}{\hbar}\langle\sigma^+(0)\sigma^-(-t)\rangle]^*\\ =& -\frac{i}{\hbar}e^{-\gamma(1+2\bar{n})|t|}e^{-i\Delta t}\langle\sigma^+(0)\sigma^-(0)\rangle,\\ G^r(t,0) =& \theta(t)[G^>(t,0) - G^<(t,0)].\end{aligned} \tag{5.9}$$

Where the whole nonlinear bath are in equilibrium so we have $\langle\sigma^+(0)\sigma^-(0)\rangle = \frac{e^{-\Delta/2T}}{2\cosh(\Delta/2T)}$ and $\langle\sigma^-(0)\sigma^+(0)\rangle = 1 - \langle\sigma^+(0)\sigma^-(0)\rangle$ are the probability weights for energy levels of TSS. The Green's functions of the TSS-boson model into frequency domain can be written as below:

$$\begin{aligned}G^>(\omega) =& -\frac{i}{\hbar}\frac{2\gamma(1+2\bar{n})}{[\gamma(1+2\bar{n})]^2+(\omega-\Delta)^2}\langle\sigma^-(0)\sigma^+(0)\rangle,\\ G^<(\omega) =& -\frac{i}{\hbar}\frac{2\gamma(1+2\bar{n})}{[\gamma(1+2\bar{n})]^2+(\omega-\Delta)^2}\langle\sigma^+(0)\sigma^-(0)\rangle,\\ G^r(\omega) =& \frac{1}{\hbar}\frac{1-2\langle\sigma^+(0)\sigma^-(0)\rangle}{i\gamma(1+2\bar{n})+(\omega-\Delta)}.\end{aligned} \tag{5.10}$$

Surface Green's function of the non-linear TSS-boson thermal bath

Due to the coupling between quantum dot and TSS, reduced Dyson equation for the non-linear thermal gate can be written as below:

$$\begin{bmatrix} D^r_{QD} & D^r_{QDB} \\ D^r_{BQD} & D^r_B \end{bmatrix} = \begin{bmatrix} d^r_{QD} & 0 \\ 0 & d^r_B \end{bmatrix} + \begin{bmatrix} d^r_{QD} & 0 \\ 0 & d^r_B \end{bmatrix} \begin{bmatrix} 0 & \eta \\ \eta & 0 \end{bmatrix} \begin{bmatrix} D^r_{QD} & D^r_{QDB} \\ D^r_{BQD} & D^r_B \end{bmatrix}. \quad (5.11)$$

Where $D^r_{QD}(D^r_B)$ is the retarded Green's function of the quantum dot (bath). $d^r_{QD}(d^r_B)$ is the retarded Green's function without the dot-bath coupling. η is the dot-bath coupling strength. According to the Eq. (5.11), the expression of D^r_{QD} can be derived.

$$(D^r_{QD})^{-1} = (d^r_{QD})^{-1} - \eta d^r_B \eta. \quad (5.12)$$

From Eq. (5.12), the retarded self-energy of non-linear thermal bath Σ^r_{nl} equals to $\eta^2 d^r_B$. In the normal bath, we can assume the fluctuation dissipation relation can be satisfied and the lesser and greater self-energy can be easily derived. In our non-linear thermal bath, we assume that such bath still in local equilibrium. Based on the Eq. (5.10) and (5.12), the self-energy of our non-linear bath can be written as below:

$$\Sigma^r_{nl}(\omega) = \frac{\eta^2}{\hbar}\left[\frac{1 - 2\langle\sigma^+(0)\sigma^-(0)\rangle}{i\gamma(1+2\bar{n}) + (\omega - \Delta)}\right]. \quad (5.13)$$

Fig. (5.7) shows the real and imaginary part of the retarded nonlinear bath self-energy. This nonlinear self-energy has a Lorentz-Drude peak in frequency Δ and it has a strong bath temperature dependence. The temperature dependence is the key difference between normal linear thermal bath and the nonlinear thermal bath. Such properties can make the thermal transistor becoming realiable.

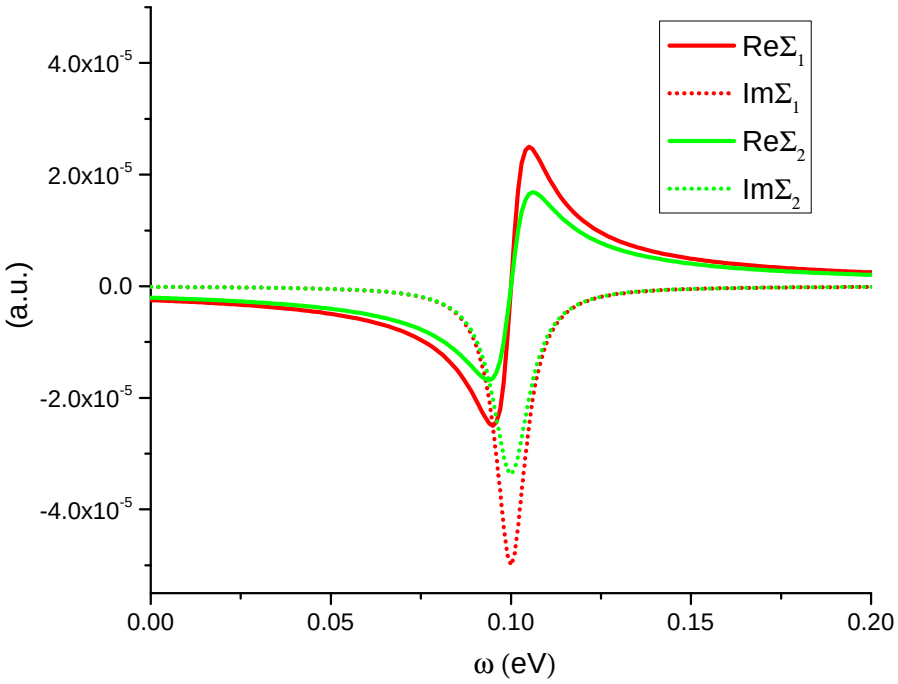

Fig. 5.7: Real and imaginary part of the retarted nonlinear bath self-energy. Δ equals to 0.05 eV and temperature T equals 300 K.

5.4.3 Results and discussion

Thermal switching

As shown in Fig. (5.8), when the temperature of gate equals to 100 K, the heat flux from gate to the drain J_D equals to zero. It is the apparent result due to the 0-th law of thermal dynamics. At the same time, the heat flux from source to the drain J_S is very small but not equals to zero. Comparing with the value of J_S with $T_G = 260$ K, J_S with $T_G = 100$ K is almost ten percent of that value. It means that we can call it is the "off" mode of the quantum radiative thermal transistor when T_G close to the temperature of the drain T_D. With the increase of T_G, the transistor is in the "on" mode.

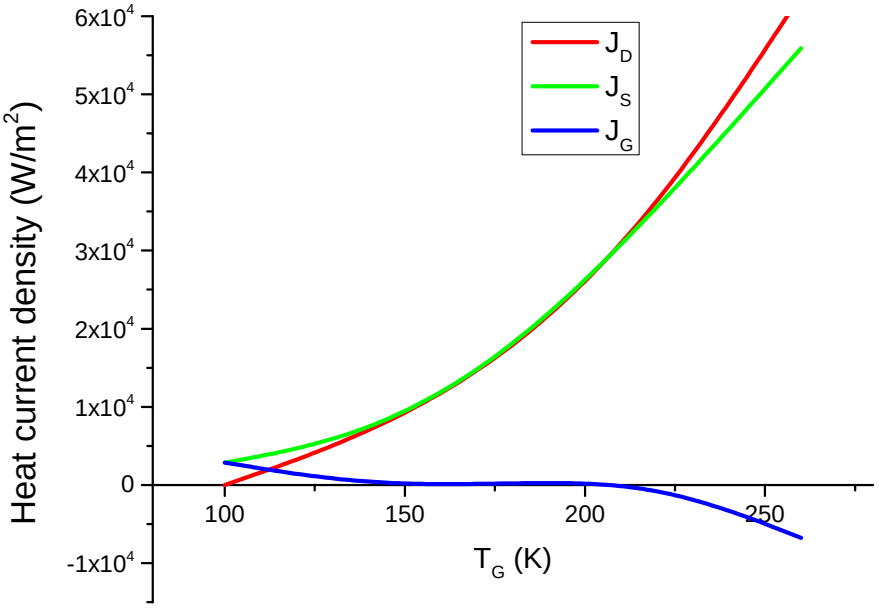

Fig. 5.8: Radiative quantum thermal transistor. Radiative current density of drain, source and gate as a function of gate temperature. The distances between gate, source and drain d is set as 36 nm. The temperature of source T_S is 500 K and the corresponding temperature for drain T_D is 100 K. $\Delta_{1(2)}$ are set as 0.1 eV. The site energy v_0, v_1 and v_3 are set as 0 eV and v_2 are set as 0.11 eV. The hopping strength between quantum dot1 and TSS η is set as 0.005 eV and 0.0005 eV between dot2 and TSS to adjust heat current. In dot0 and dot3, we use wide bath approximation and the coupling strength are set as 0.5 eV and the energy cutoff are 50 eV. The chemical potential of QD1 to QD4 are set as 0 eV for simplicity. The coupling between TTS and boson bath λ_1 are both set as 0.005 eV for the weak coupling assumption of quantum master equation.

Thermal modulation

When T_G is changed from 100 K to 260 K, Fig. (5.8) shows there is very small gate current J_G and very large source and drain heat current $J_S \& J_D$ are existed comparing with J_G. These results indicate that a small change of J_G can lead to the large changes of $J_S \& J_D$, when the gate temperature is changed from 100 K to 260 K. Then in another word, the heat flux out of the source and heat flux transferred into drain can be modulated by a small change of gate heat flux.

Thermal amplification

Another important feature of a thermal transistor is the ability to amplify the current towards the drain. Previous researchers applied the phase transition materials to achieve thermal amplification, and the amplification effects only exist in a small gate temperature region[13]. In our calculation, we can achieve a significant thermal amplification in a large gate temperature region through the novel properties of the non-linear heat bath. As we know, the negative differential thermal conductance is the key factor to have a thermal amplification effect. The amplification factor can be defined as below.

$$\alpha = \left|\frac{\partial J_D}{\partial J_G}\right| = \frac{1}{\left|1 - \frac{\partial J_S}{\partial T_G} / \frac{\partial J_D}{\partial T_G}\right|}. \tag{5.14}$$

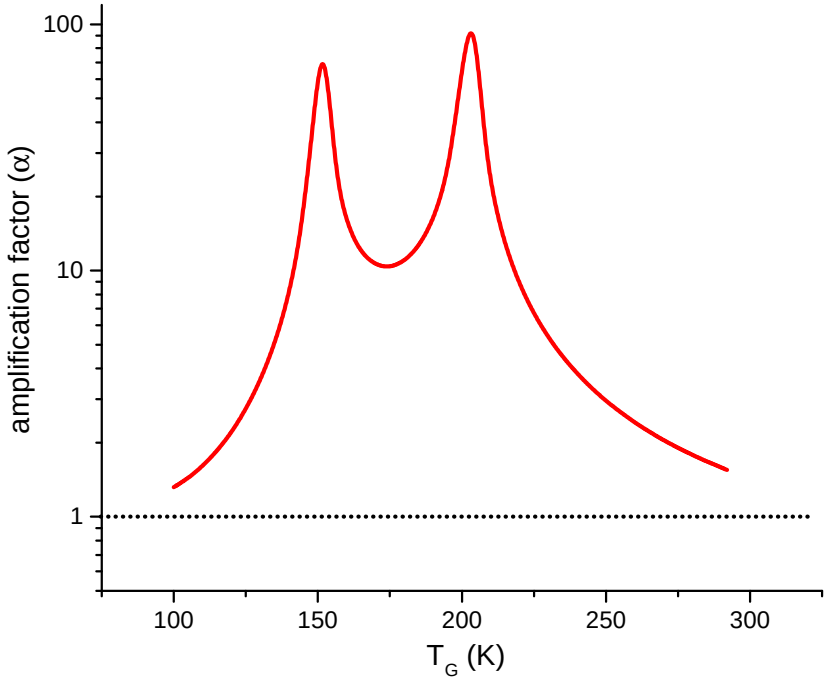

Fig. 5.9: Amplification factor of radiative quantum thermal transistor. Red line is the amplification factor as a function of gate temperature. Dot line is the amplification factor $\alpha = 1$.

Fig. (5.9) shows the amplification factor α as a function of gate temperature in a solid red line. Comparing the dot line $\alpha = 1$, the amplification factor α can be always

larger than 1 when T_G locates from 100 K to 260 K. Especially, when T_G equals to 150 K or 210 K, we find that the gate temperature dependence of J_S and J_D is almost the same and there will be a large amplification effects.

Discussion

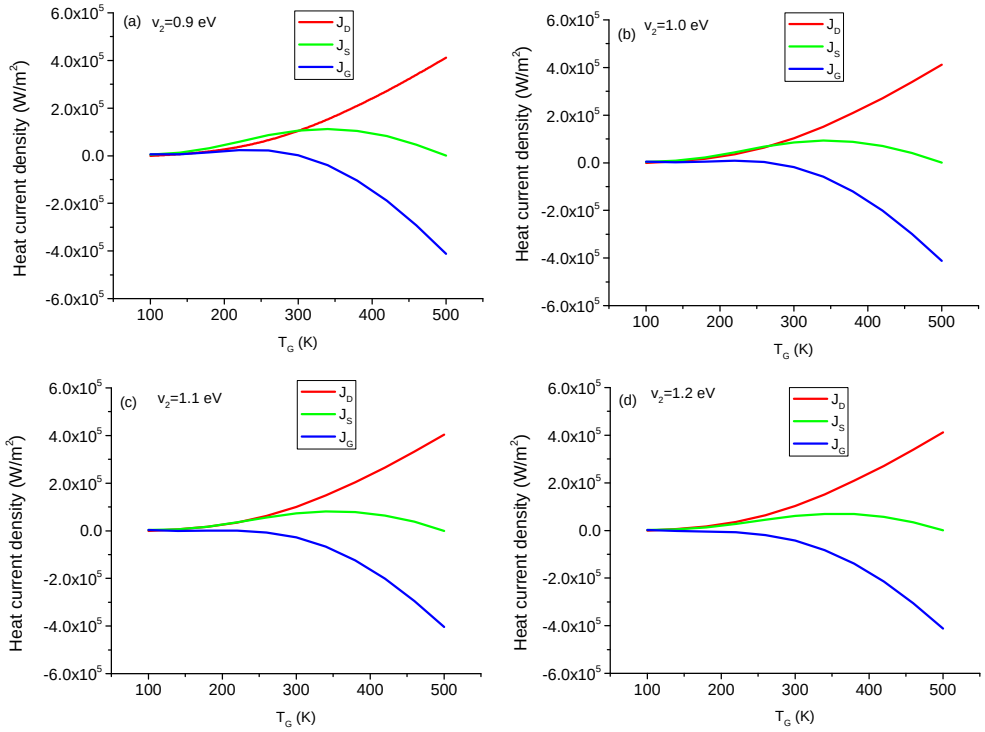

Fig. 5.10: Spectral functin analysis.(a) Spectral functin of source with different gate temperature. (b) Spectral functin of drain with different gate temperature. $T_S = 500$ K and $T_D = 100$ K.

In above calculation, to find the thermal transistor effects, we set site energy of dot2 v_2 equals to 0.11 eV, which is closed to the energy difference between ground state and excite state of TSS. In our parameter setup, a suitable value of v_2 is needed. In figure (5.10), the effects of v_2 is tested with different value. We find that when the value of v_2 is increasing, the total heat current density of source J_S will decrease when T_G change from 100 K to 500 K. Such effects can be understood through the RHT between two dots. When v_2 is large, the system is far away from the resonant cases $v_1 = v_2$. However, except the site energy has effects on the heat current density, the self-energy of bath also makes some contributions. In the normal linear bath cases, when

the temperature difference between gate and source are the largest, the largest current should be discover. Due to the the energy level alignment between the excited state of TSS and dot site energy, the density of state of low frequency, which is helpful for RHT, can be increased with the gate temperature increasing in our nonlinear thermal bath. So we can achieve the negative differential thermal conductance in low temperature region. When T_G equals to T_S, the heat current equals to zero due to the thermal dynamics law. That means there is competition between energy level alignment and temperature gradient. Such effects are the core physics picture for our scalar field based quantum thermal transistor.

The more detailed information for quantum thermal transistor effects can be understood from spectral function analysis in Fig. (5.11). Fig. (5.11a) shows the spectral transfer function between drain and gate (dot0 and dot1) and the site energy of dots are set as zero. In that condition, the nonlinear bath contribution almost have no difference with normal linear bath: the heat current density increased with the temperature increasing. Fig. (5.11b) shows the spectral transfer function between source and gate (dot2 and dot3) and the site energy is closed to energy level of excited state in TSS. Due to the energy level alignment, the electron in excited state is easier to hop to the energy level of dot. But the population of excited state of TSS depends on the bath temperature. When the gate temperature increases from 100 K to 500 K, population in excited state will increase due to the thermal distribution. The density of state for RHT will increase due to such energy alignment effects. The spectral transfer function in Fig. (5.11b) shows that there is peak in 0.01 eV and provide a prove for our analysis. Besides, due to the temperature gradient become small, the net heat current also be small. So finally, when $T_G = T_S$, the heat current equals to zero due to the thermal dynamics law.

In our calculation, we use four quantum dots to achieve the radiative quantum thermal transistor i.e. two normal quantum dots for source and drain. For the gate, we combine it with the non-linear heat bath. The new problem is that how to achieve that transistor experimentally? For the source and drain, we can use the normal metal

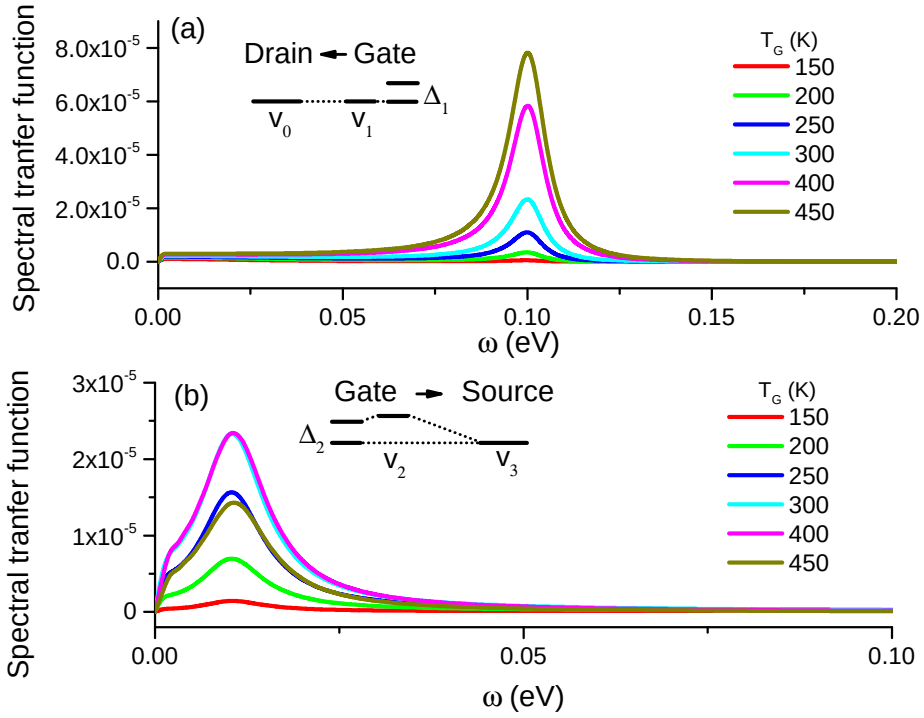

Fig. 5.11: Spectral functin analysis.(a) Spectral functin of source with different gate temperature. (b) Spectral functin of drain with different gate temperature. $T_S = 500$ K and $T_D = 100$ K.

nano-particles or graphene covered nano-particles. For the thermal gate, we can use the double quantum well and combine it with the exciton gas as Bose heat bath. All of these components are well studied experimentally. With the line configuration, our radiative quantum thermal transistor is easier for integration in the future. Due to the contribution of scalar field photon, a large magnitude of radiative heat flux can be found among the device. This process can overcome the limitation for the far-field radiative heat transfer. Besides, comparing with thermal transistor through phonon, our transistor do not be limited by the speed of heat carriers.

5.5 Summary

In this Chapter, we use the NEGF method to investigate the scalar-photon based thermal rectifiers and thermal transistors. That is the extended work for our previous Chapter. Due to the different quantum-dots-bath coupling, we find that we can achieve high

rectification effects for our two quantum dots rectifiers. Next, due to the requirement of negative differential thermal conductance and failure of linear thermal bath in that condition, we combine the novel properties of our two quantum dots calculation with the non-linear heat bath. A radiative quantum thermal transistor is constructed based on the scalar photon. The thermal switching, modulation and amplification effects are discussed through the spectral analysis. Last we also consider how to achieve such device experimentally.

Chapter 6

Conclusion and future works

"Now this is not the end.
It is not even the beginning of the end.
But it is, perhaps, the end of the beginning."
—Winston Churchill

RHT is the date between light and heat. Due to the differences between the photon and other heat carriers, the RHT provide a non-contacted channel for heat transfer. In nanoscale, the contributions of various quantum effects open a broad door for the investigation of RHT. The primary purpose of this thesis is to focus on the RHT in nanoscale and investigate the potential applications for photon-based thermal management and thermal circuit. In this chapter, we summarize the significant results presented in this thesis and show the directions for future works.

At first, we start this research area with a brief review of the historical development both theoretically and experimentally. That research area is still alive recently. Some very recently experimental measurements are also discussed. In the second part of thesis introduction, we give a short introduction to the historical development of NEGF. That is a useful method for the quantum transport calculation, and we are going to extend that method for the investigations of RHT. Besides, we present one kind of potential employments for RHT: thermal management and thermal circuit. Based on RHT, the photon-based modulation of heat with nanoscale separation can become reliable, and

it may provide a different way for thermal computing. At last, the structure of thesis arrangement is given straightforwardly through a construction figure. In this thesis, we will focus on the stories of RHT from the theoretical explanation to actual applications. The outline of our future works is also followed such schedule.

In the method part, Chapter 2, we introduce a basic theory for RHT calculation: FE, which is born in 1951 and widely used in the instigations of RHT. Through FE method, the exact formula for RHT between two semi-infinite planes is also given to draw a clear physical picture of the whole procedure of NFRHT. Next, our derivations develop a longitudinal wave method to reproduce the same results for RHT based on FE methods. Our approach keeps self-consistency with FE formalism. That calculation makes a foundation for scalar field theory in the next Chapter. Besides, we also give a brief introduction for the NEGF formalism with Keldysh contour order. With the nonequilibrium steady state assumptions, the Green's function can be much simplified in Keldysh contour order, which is convenient for quantum transport calculation. Once we know the Green's function of various quantum systems, the transport properties, such as energy current, can be calculated obviously.

One of extending example for our longitudinal wave method is to find the near-field phonon effects due to the similarity between phonon and photon. In the corresponding calculation, the near-field phonon effects can also enhance the heat flux and even exceeding the phonon blackbody limit several times. Such effect can provide a potential for the further investigation of TIM. Near-field phonon effect offers an interesting way to tune the heat transfer through evanescent phonon, which is not carefully considered in previous research for TIM. With the help of such results, a new channel for phonon heat transfer can be provided. One of our future works will focus on the near-field photon effects. In our example calculations, the near-field phonon effects are limited by phonon group velocity of the materials and such effects are only existed at low temperature. For the real systems, such effects can not be conveniently applied to enhance the heat transfer. How to control and reduce the thermal resistance in TIM though near-field phonon effects? It needs to be carefully considered shortly.

Next,we discuss the connection between RHT and 2-d materials. Recently, the wafer-scale growth of monolayer MoS_2 films with spatial homogeneity is realized on SiO_2 substrate. Together with the latest reported high mobility, MoS_2 based integrated electronic devices are expected to be fabricated in the near future. Owing to the low lattice thermal conductivity in monolayer MoS_2, and the increased transistor density accompanied with the increased power density, heat dissipation will become a crucial issue for these integrated devices. In Chapter 3, using the formalism of fluctuation electrodynamics, we explored the NFRHT from a monolayer MoS_2 to graphene. We demonstrate that in resonance, the maximum heat transfer via near-field radiation between MoS_2 and graphene can be ten times higher than the in-plane lattice thermal conduction for the MoS_2 sheet. Therefore a new thermal management strategy for the MoS_2 integrated device is proposed: graphene sheet is brought into proximity, 10-20 nm from the MoS_2 device; heat energy transfer from MoS_2 to graphene via near-field radiation; this amount of heat energy then be conducted to contact due to ultra-high lattice thermal conductivity of graphene. Our work sheds light for developing a new cooling strategy for nanodevices constructing with low thermal conductivity materials.

The key findings in Chapter 3 construct a connection between NFRHT and 2-d materials. Due to the novel properties and broad application prospects, the 2-d material is an ideal platform for the further investigations of RHT in nanoscale. In Chapter 3, the intra-band optical conductivity of MoS_2 plays the dominated role for the near-field cooling strategy. However, due to the spin-orbit coupling, MoS_2 can obtain the novel inter-band optical conductivity. Trion, a localized excitation which consists of three charged quasiparticles, is found in MoS_2 and can be optically created with valley and spin polarized holes[160]. The trion in MoS_2 also has a large binding energy (20 meV) which can be existed even in room temperature. One of the interesting questions is how to combine trion effects with NFRHT. One of the creative ideas is that we can active thermal extraction through NFRHT based on trion effects of MoS_2. Based on such mechanism, we can develop a different cooling strategy for MoS_2 device and also promote the extension of radiative thermal management in nanoscale.

In Chapter 4, using NEGF, we consider a one-dimensional model of RHT for which the contribution of the electromagnetic field is only from the scalar potential and the effect of the vector potential is ignoring. It is a valid hypothesis when the distances between objects are very close, i.e., on the order of nanometers. Based on the Lorenz gauge, the scalar field can be quantized with the standard canonical quantization, i.e., the scalar photons. In the limit as the speed of light approaches infinity, the theory can reduce to a pure Coulomb interaction which is well studied in condensed matter physics. The model can describe the properties of parallel plate capacitor physics, where a new length scale related to its capacitance emerges. Smaller than this length scale, we find larger RHT through charge fluctuations. That differs markedly from the general Rytov's fluctuation electrodynamics theory in which the enhancement of RHT is due to evanescent modes. Our theory may explain recent experimental measurements[9] where charge fluctuations may play a crucial role in RHT.

An important aspect for NEGF formalism makes a foundation for the quantum control of RHT in nanoscale. In principle, various quantum effects, such as Berry phase, quantum phase transition and so on, can be included in the calculation without computing the dielectric constant. We realize that amount of interesting phenomena can be found once the quantum effects can be carefully obtained. To combine RHT with novel quantum effects, a quantum field based method for RHT is needed. However, our NEGF methods for RHT are only valid in nonequilibrium steady state. How to extend our method to the driving system? This is a difficult but important question for the further investigation of RHT. Another limitation of our NEGF method is that it only works well for nano-system. For a macroscopic system, the computation complexity will increase exponentially due to numerous degrees of freedom. In that case, the self-consistency procedure will become very difficult to achieve. In the future, once this obstacle is solved, I think this research field can be tremendous influenced.

In Chapter 5, using NEGF method, we investigate the quantum thermal rectifiers and thermal transistor based on the scalar-field photon. The tight-binding models for the electrons are coupled to the electromagnetic field continuum through a scalar potential.

Using properties of the quantum capacitor physics, we observe and report the thermal rectification effects in double quantum dots model due to the asymmetric electron-bath couplings. With the help of non-linear thermal gate, a radiative quantum thermal transistor is also achieved by the combination of four quantum dots. We numerically demonstrate that the thermal switching, thermal modulation, and thermal amplification can be obtained in the radiative quantum thermal transistor. Our approaches and results provide a potential application for thermal management and thermal circuits in the quantum region.

The calculations in Chapter 5 are based on a toy model. To go from theoretical calculations to the actual applications, one of the questions we need carefully think about is how to achieve those devices experimentally. For radiative thermal rectifier, we can achieve it with graphene lying on the different substrates. Due to the different sample-substrate interactions, the thermal rectification effects can be found with such symmetry breaking. For the radiative quantum thermal transistor, one of the challenges is how to find an appropriate thermal gate. The results in Chapter 3 give one potential way to make it realizable: making use of the trion effects. Trion, in another word, is always existed in the exciton gas and the boson bath is already existed in such system. Another challenge is the realization of TSS. In the model calculation, we assume the double quantum well. But we think we can find a wiser way to achieve it. MoS_2, which is well studied in Chapter 3, has a split band gap with about 30-50 meV due to the spin-orbit coupling. It can be a natural TSS. The next question is how to construct a radiative quantum thermal transistor through the special properties of 2-d materials. It can be an interesting but challengeable question in the future.

For RHT, here, I provide some personal brainstorms for the future works: "smart heat" i.e. thermal machine learning, nanoscale passive cooling and so on. The next question is the question which I always raise a question to myself when I started my Ph.D life: what I can do to make a difference in my research area? In fact, I think I need use the whole research life to answer that question: you never know what you will find tomorrow. In the end, I would like to use a sketch to finish my thesis. Figure (6.1)

Fig. 6.1: Sketch for the future works.

shows what I will do in the future, i.e., make a seed for my research life grow into a colorful tree. Now, it is, perhaps, the end of the beginning.

Bibliography

[1] M. Planck, *Theorie der Wärmestrahlung* (J. A. Barth, Leipzig, 1906) translated into English by Morton Masius in M. Planck, *The Theory of Heat Radiation*, (Dover, New York, 1991).

[2] A. Narayanaswamy, S. Shen, and G. Chen, Physical Review B **78**, 115303 (2008).

[3] A. W. Rodriguez, M. T. H. Reid, J. Varela, J. D. Joannopoulos, F. Capasso, and S. G. Johnson, Physical Review Letters **110**, 014301 (2013).

[4] Y. Yang and L. Wang, Physical Review Letters **117**, 044301 (2016).

[5] K. Chen, P. Santhanam, S. Sandhu, L. Zhu, and S. Fan, Physical Review B **91**, 134301 (2015).

[6] O. Ilic, M. Jablan, J. D. Joannopoulos, I. Celanovic, H. Buljan, and M. Soljačić, Physical review B **85**, 155422 (2012).

[7] R. St-Gelais, L. Zhu, S. Fan, and M. Lipson, Nature Nanotechnology **11**, 515 (2016).

[8] O. Ilic, M. Jablan, J. D. Joannopoulos, I. Celanovic, and M. Soljačić, Optics express **20**, A366 (2012).

[9] K. Kloppstech, N. Könne, S.-A. Biehs, A. W. Rodriguez, L. Worbes, D. Hellmann, and A. Kittel, Nature Communications **8** (2017).

[10] L. Cui, W. Jeong, V. Fernández-Hurtado, J. Feist, F. J. García-Vidal, J. C. Cuevas, E. Meyhofer, and P. Reddy, Nature Communications **8** (2017).

[11] P. Ben-Abdallah and S.-A. Biehs, Applied Physics Letters **103**, 191907 (2013).

[12] C. Chang, D. Okawa, A. Majumdar, and A. Zettl, Science **314**, 1121 (2006).

[13] P. Ben-Abdallah and S.-A. Biehs, Physical Review Letters **112**, 044301 (2014).

[14] K. Joulain, J. Drevillon, Y. Ezzahri, and J. Ordonez-Miranda, Physical Review Letters **116**, 200601 (2016).

[15] V. Kubytskyi, S.-A. Biehs, and P. Ben-Abdallah, Physical Review Letters **113**, 074301 (2014).

[16] B. Song, A. Fiorino, E. Meyhofer, and P. Reddy, Aip Advances **5**, 053503 (2015).

[17] W. Herschel, Philosophical Transactions of the Royal Society of London , 284 (1800).

[18] W. Herschel, Philosophical Transactions of the Royal Society of London **90**, 293 (1800).

[19] W. Herschel, Philosophical Transactions of the Royal Society of London **90**, 437 (1800).

[20] H. B. Callen and T. A. Welton, Physical Review **83**, 34 (1951).

[21] L. D. Landau and E. M. Lifshitz, *Course of theoretical physics* (Elsevier, 2013).

[22] R. Kubo, Reports on progress in physics **29**, 255 (1966).

[23] W. Eckhardt, Physical Review A **29**, 1991 (1984).

[24] S. M. Rytov, "Theory of electric fluctuations and thermal radiation," Tech. Rep. (AIR FORCE CAMBRIDGE RESEARCH LABS HANSCOM AFB MA, 1959).

[25] S. Rytov, Y. A. Kravtsov, and V. Tatarskii, Priniciples of statistical radiophysics. 3. Elements of random fields., by Rytov, SM; Kravtsov, YA; Tatarskii, VI. Springer, Berlin (Germany, FR), 1989, 249 p., ISBN 3-540-17829-5, (1989).

[26] A. Emslie, GEOPHYSICS (1962).

[27] G. Domoto, R. Boehm, and C. L. Tien, Journal of Heat Transfer **92**, 412 (1970).

[28] D. Polder and M. Van Hove, Physical Review B **4**, 3303 (1971).

[29] J. Pendry, Journal of Physics: Condensed Matter **11**, 6621 (1999).

[30] A. Volokitin and B. N. Persson, Reviews of Modern Physics **79**, 1291 (2007).

[31] S. Kutateladze, N. Rubtsov, and Y. A. Bal'Tsevich, in *Soviet Physics Doklady*, Vol. 23 (1978) p. 577.

[32] C. Hargreaves, Physics Letters A **30**, 491 (1969).

[33] L. Hu, A. Narayanaswamy, X. Chen, and G. Chen, Applied Physics Letters **92**, 133106 (2008).

[34] R. Ottens, V. Quetschke, S. Wise, A. Alemi, R. Lundock, G. Mueller, D. H. Reitze, D. B. Tanner, and B. F. Whiting, Physical Review Letters **107**, 014301 (2011).

[35] T. Kralik, P. Hanzelka, M. Zobac, V. Musilova, T. Fort, and M. Horak, Physical Review Letters **109**, 224302 (2012).

[36] C. Williams and H. Wickramasinghe, Microelectronic Engineering **5**, 509 (1986).

[37] W. Müller-Hirsch, A. Kraft, M. Hirsch, J. Parisi, and A. Kittel, Journal of Vacuum Science & Technology A: Vacuum, Surfaces, and Films **17**, 1205 (1999).

[38] J.-B. Xu, K. Läuger, R. Möller, K. Dransfeld, and I. Wilson, Journal of Applied Physics **76**, 7209 (1994).

[39] A. Kittel, W. Müller-Hirsch, J. Parisi, S.-A. Biehs, D. Reddig, and M. Holthaus, Physical Review Letters **95**, 224301 (2005).

[40] K. Kim, B. Song, V. Fernández-Hurtado, W. Lee, W. Jeong, L. Cui, D. Thompson, J. Feist, M. H. Reid, F. J. García-Vidal, *et al.*, Nature **528**, 387 (2015).

[41] H. Haug and A.-P. Jauho, *Quantum kinetics in transport and optics of semiconductors* (Springer, Berlin New York, 2008).

[42] G. D. Mahan, *Many-Particle Physics*, 3rd ed. (Kluwer Academic, 2000).

[43] J. Schwinger, Journal of Mathematical Physics **2**, 407 (1961).

[44] L. V. Keldysh *et al.*, Soviet Physics - Journal of Experimental and Theoretical Physics **20**, 1018 (1965).

[45] C. Caroli, R. Combescot, P. Nozieres, and D. Saint-James, Journal of Physics C: Solid State Physics **4**, 916 (1971).

[46] L. P. Kadanoff and G. A. Baym, *Quantum statistical mechanics: Green's function methods in equilibrium and nonequilibirum problems* (Benjamin, 1962).

[47] X. Liu, L. Wang, and Z. M. Zhang, Nanoscale and Microscale Thermophysical Engineering **19**, 98 (2015).

[48] A. Volokitin and B. Persson, Physical Review B **78**, 155437 (2008).

[49] G. Dedkov and A. Kyasov, Surface Science **604**, 562 (2010).

[50] J. Pendry, Journal of Physics: Condensed Matter **9**, 10301 (1997).

[51] L. Cui, Y. Huang, J. Wang, and K.-Y. Zhu, Applied Physics Letters **102**, 053106 (2013).

[52] A. Volokitin and B. Persson, Physical Review B **83**, 241407 (2011).

[53] M. Terraneo, M. Peyrard, and G. Casati, Physical Review Letters **88**, 094302 (2002).

[54] P. Van Zwol, K. Joulain, P. B. Abdallah, J.-J. Greffet, and J. Chevrier, Physical Review B **83**, 201404 (2011).

[55] N. Li, J. Ren, L. Wang, G. Zhang, P. Hänggi, and B. Li, Reviews of Modern Physics **84**, 1045 (2012).

[56] F. London, Zeitschrift für Physik A Hadrons and Nuclei **63**, 245 (1930).

[57] H. Casimir and D. Polder, Physical Review **73**, 360 (1948).

[58] E. Lifshitz, Soviet Physics **2**, 73 (1956).

[59] J. D. Jackson and R. F. Fox, American Journal of Physics **67**, 841 (1999).

[60] J. A. Kong, Wiley-Interscience , 348 (1975).

[61] C.-T. Tai, *Dyadic Green functions in electromagnetic theory* (Institute of Electrical & Electronics Engineers (IEEE), 1994).

[62] J. E. Sipe, Journal of the Optical Society of America B **4**, 481 (1987).

[63] S.-A. Biehs, E. Rousseau, and J.-J. Greffet, Physical Review Letters **105**, 234301 (2010).

[64] J.-S. Wang, J. Wang, and J. T. Lü, The European Physical Journal B **62**, 381 (2008).

[65] J. Schleeh, J. Mateos, I. Íñiguez-de-la Torre, N. Wadefalk, P.-A. Nilsson, J. Grahn, and A. Minnich, Nature Materials **14**, 187 (2015).

[66] E. T. Swartz and R. O. Pohl, Reviews of Modern Physics **61**, 605 (1989).

[67] W. Little, Canadian Journal of Physics **37**, 334 (1959).

[68] A. Abrikosov, *Methods of quantum field theory in statistical physics*.

[69] A. Prociuk, H. Phillips, and B. Dunietz, in *Journal of Physics: Conference Series*, Vol. 220 (IOP Publishing, 2010) p. 012008.

[70] N. A. Zimbovskaya and M. R. Pederson, Physics Reports **509**, 1 (2011).

[71] J.-S. Wang, B. K. Agarwalla, H. Li, and J. Thingna, Frontiers of Physics **9**, 673 (2014).

[72] Y. Meir and N. S. Wingreen, Physical Review Letters **68**, 2512 (1992).

[73] G. Fiori, F. Bonaccorso, G. Iannaccone, T. Palacios, D. Neumaier, A. Seabaugh, S. K. Banerjee, and L. Colombo, Nature Nanotechnology **9**, 768 (2014).

[74] A. Geim and I. Grigorieva, Nature **499**, 419 (2013).

[75] B. W. Baugher, H. O. Churchill, Y. Yang, and P. Jarillo-Herrero, Nano Letters **13**, 4212 (2013).

[76] H. Liu, A. T. Neal, and P. D. Ye, ACS nano **6**, 8563 (2012).

[77] H. Liu, M. Si, S. Najmaei, A. T. Neal, Y. Du, P. M. Ajayan, J. Lou, and P. D. Ye, Nano Letters **13**, 2640 (2013).

[78] B. Radisavljevic and A. Kis, Nature Materials **12**, 815 (2013).

[79] H. Schmidt, S. Wang, L. Chu, M. Toh, R. Kumar, W. Zhao, A. H. Castro Neto, J. Martin, S. Adam, and B. Ãůzyilmaz, Nano Letters **14**, 1909 (2014).

[80] R. Cheng, S. Jiang, Y. Chen, Y. Liu, N. Weiss, H.-C. Cheng, H. Wu, Y. Huang, and X. Duan, Nature Communications **5**, 5143 (2014).

[81] Y. Liu, H. Wu, H. C. Cheng, S. Yang, E. Zhu, Q. He, M. Ding, D. Li, J. Guo, N. Weiss, Y. Huang, and X. Duan, Nano Letters **15**, 3030 (2015).

[82] S. Najmaei, Z. Liu, W. Zhou, X. Zou, G. Shi, S. Lei, B. I. Yakobson, J.-C. Idrobo, P. M. Ajayan, and J. Lou, Nature Materials **12**, 754 (2013).

[83] H. Qiu, L. Pan, Z. Yao, J. Li, Y. Shi, and X. Wang, Applied Physics Letters **100**, 123104 (2012).

[84] H. Qiu, T. Xu, Z. Wang, W. Ren, H. Nan, Z. Ni, Q. Chen, S. Yuan, F. Miao, F. Song, G. Long, Y. Shi, L. Sun, J. Wang, and X. Wang, Nature Communications **4**, 2642 (2013).

[85] Z. Yu, Y. Pan, Y. Shen, Z. Wang, Z.-Y. Ong, T. Xu, R. Xin, L. Pan, B. Wang, L. Sun, J. Wang, G. Zhang, Y. W. Zhang, Y. Shi, and X. Wang, Nature Communications **5**, 5290 (2014).

[86] Y. Cai, G. Zhang, and Y.-W. Zhang, Journal of the American Chemical Society **136**, 6269 (2014).

[87] K. Kaasbjerg, K. S. Thygesen, and K. W. Jacobsen, Physical Review B **85**, 115317 (2012).

[88] X. Cui, G.-H. Lee, Y. D. Kim, G. Arefe, P. Y. Huang, C.-H. Lee, D. A. Chenet, X. Zhang, L. Wang, F. Ye, F. Pizzocchero, B. S. Jessen, K. Watanabe, T. Taniguchi, D. A. Muller, T. Low, P. Kim, and J. Hone, Nature Nanotechnology **10**, 534 (2015).

[89] K. Kang, S. Xie, L. Huang, Y. Han, P. Y. Huang, K. F. Mak, C.-J. Kim, D. Muller, and J. Park, Nature **520**, 656 (2015).

[90] A. A. Balandin, Nature Materials **10**, 569 (2011).

[91] A. M. Marconnet, M. A. Panzer, and K. E. Goodson, Reviews of Modern Physics **85**, 1295 (2013).

[92] M. M. Sadeghi, M. T. Pettes, and L. Shi, Solid State Communications **152**, 1321 (2012).

[93] N. Yang, X. Xu, G. Zhang, and B. Li, AIP Advances **2**, 041410 (2012).

[94] S. Sahoo, A. P. Gaur, M. Ahmadi, M. J.-F. Guinel, and R. S. Katiyar, The Journal of Physical Chemistry C **117**, 9042 (2013).

[95] A. Taube, J. Judek, A. ŁapinÌĄska, and M. Zdrojek, ACS applied materials & interfaces **7**, 5061 (2015).

[96] R. Yan, J. R. Simpson, S. Bertolazzi, J. Brivio, M. Watson, X. Wu, A. Kis, T. Luo, A. R. Hight Walker, and H. G. Xing, ACS nano **8**, 986 (2014).

[97] Y. Cai, J. Lan, G. Zhang, and Y.-W. Zhang, Physical Review B **89**, 035438 (2014).

[98] J.-W. Jiang, H. S. Park, and T. Rabczuk, Journal of Applied Physics **114**, 064307 (2013).

[99] W. Li, J. Carrete, and N. Mingo, Applied Physics Letters **103**, 253103 (2013).

[100] X. Liu, G. Zhang, Q.-X. Pei, and Y.-W. Zhang, Applied Physics Letters **103**, 133113 (2013).

[101] X. Wei, Y. Wang, Y. Shen, G. Xie, H. Xiao, J. Zhong, and G. Zhang, Applied Physics Letters **105**, 103902 (2014).

[102] Z. Yu, N. P. Sergeant, T. Skauli, G. Zhang, H. Wang, and S. Fan, Nature Communications **4**, 1730 (2013).

[103] E. Rousseau, A. Siria, G. Jourdan, S. Volz, F. Comin, J. Chevrier, and J.-J. Greffet, Nature Photonics **3**, 514 (2009).

[104] S. Shen, A. Narayanaswamy, and G. Chen, Nano Letters **9**, 2909 (2009).

[105] C. R. Otey, W. T. Lau, S. Fan, *et al.*, Physical Review Letters **104**, 154301 (2010).

[106] B. Guha, C. Otey, C. B. Poitras, S. Fan, and M. Lipson, Nano Letters **12**, 4546 (2012).

[107] H. H. Yap and J.-S. Wang, Physical Review E **95**, 012126 (2017).

[108] S. V. Boriskina, H. Ghasemi, and G. Chen, Materials Today **16**, 375 (2013).

[109] V. Chiloyan, J. Garg, K. Esfarjani, and G. Chen, Nature Communications **6**, 6755 (2015).

[110] Y. H. HOE, *NEAR-FIELD RADIATIVE HEAT TRANSFER IN PRESENCE OF SURFACE CHARGE*, Ph.D. thesis (2016).

[111] L. Falkovsky and A. Varlamov, The European Physical Journal B-Condensed Matter and Complex Systems **56**, 281 (2007).

[112] L. Falkovsky, in *Journal of Physics: Conference Series*, Vol. 129 (IOP Publishing, 2008) p. 012004.

[113] H. Rostami, A. G. Moghaddam, and R. Asgari, Physical Review B **88**, 085440 (2013).

[114] H. Rostami and R. Asgari, Physical Review B **89**, 115413 (2014).

[115] J. R. Howell, M. P. Mengüç, and R. Siegel, *Thermal Radiation Heat Transfer, 6th Edition* (CRC Press, 2015).

[116] S. M. Rytov, *Theory of Electric Fluctuations and Thermal Radiation* (Air Force Cambridge Research Center, Bedford, MA, 1953).

[117] C. M. Hargreaves, *Philips Research Reports* (NV Philips' Gloeilampenfabrieken, 1973).

[118] S. V. Boriskina, J. K. Tong, W.-C. Hsu, B. Liao, Y. Huang, V. Chiloyan, and G. Chen, Nanophotonics **5**, 134 (2016).

[119] W.-C. Hsu, J. K. Tong, B. Liao, Y. Huang, S. V. Boriskina, and G. Chen, Scientific Reports **6** (2016).

[120] P. Rodriguez-López, W.-K. Tse, and D. A. Dalvit, Journal of Physics: Condensed Matter **27**, 214019 (2015).

[121] J. Peng, G. Zhang, and B. Li, Applied Physical Letter **107**, 133108 (2015).

[122] B. Song, D. Thompson, A. Fiorino, Y. Ganjeh, P. Reddy, and E. Meyhofer, Nature Nanotechnology **11**, 509 (2016).

[123] G. D. Mahan, Applied Physical Letter **98**, 132106 (2011).

[124] G. Domingues, S. Volz, K. Joulain, and J.-J. Greffet, Physical Review Letters **94**, 085901 (2005).

[125] R. Yu, A. Manjavacas, and F. J. Garcia de Abajo, Nature Communications **8**, 2 (2017).

[126] S. Xiong, K. Yang, Y. A. Kosevich, Y. Chalopin, R. D' Agosta, P. Cortona, and S. Volz, Physical Review Letters **112**, 114301 (2014).

[127] K. Joulain, J.-P. Mulet, F. Marquier, R. Carminati, and J.-J. Greffet, Surface Science Reports **57**, 59 (2005).

[128] J.-S. Wang and J. Peng, Europhysics Letters **118**, 24001 (2017).

[129] G. Mahan, Physical Review B **95**, 115427 (2017).

[130] J.-T. Lü and J.-S. Wang, Physical review B **76**, 165418 (2007).

[131] J.-S. Wang, N. Zeng, J. Wang, and C.-K. Gan, Physical Review E **75**, 061128 (2007).

[132] L. Zhang, J.-T. Lü, and J.-S. Wang, Journal of Physics: Condensed Matter **25**, 445801 (2013).

[133] C. Tannoudji, J. Dupont-Roc, and G. Grynberg, *Photons and atoms : introduction to quantum electrodynamics* (Wiley, New York, 1989).

[134] O. Keller, *Quantum theory of near-field electrodynamics* (Springer, Berlin New York, 2011).

[135] S. Weinberg, *The quantum theory of fields* (Cambridge University Press, Cambridge, 1995).

[136] R. J. Glauber, Annals of the New York Academy of Sciences **480**, 336 (1986).

[137] S. Datta, *Electronic transport in mesoscopic systems* (Cambridge University Press, Cambridge, 1997).

[138] N. F. Ramsey, Physical Review **103**, 20 (1956).

[139] R. H. Swendsen and J.-S. Wang, Physica A: Statistical Mechanics and its Applications **453**, 24 (2016).

[140] L. Hedin, Physical Review **139**, A796 (1965).

[141] G. Stefanucci and R. van Leeuwen, *Nonequilibrium many-body theory of quantum systems : a modern introduction* (Cambridge University Press, Cambridge, 2013).

[142] A. Fetter and J. D. Walecka, *Quantum theory of many-particle systems* (Dover Publications, Mineola, N.Y, 2003).

[143] A. Altland and B. Simons, *Condensed Matter Field Theory* (Cambridge University Press, Leiden, 2010).

[144] S. Datta, Superlattices Microstruct **28**, 253 (2000).

[145] P. Ben-Abdallah and K. Joulain, Phys. Rev. B **82**, 121419 (2010).

[146] D. Neamen, *Semiconductor physics and devices* (McGraw-Hill, Inc., 2002).

[147] C. R. Otey, W. T. Lau, and S. Fan, Physical Review Letters **104**, 154301 (2010).

[148] W. Chung Lo, L. Wang, and B. Li, Journal of the Physical Society of Japan **77**, 054402 (2008).

[149] L. Zhang, J.-S. Wang, and B. Li, Physical review B **81**, 100301 (2010).

[150] N. Yang, G. Zhang, and B. Li, Applied Physical Letter **95**, 033107 (2009).

[151] D. F. Walls and G. J. Milburn, *Quantum optics* (Springer Science & Business Media, 2007).

[152] A. Montina and F. Arecchi, Physical Review Letters **100**, 120401 (2008).

[153] U. Weiss, *Quantum dissipative systems*, Vol. 13 (World scientific, 2012).

[154] D. Segal and A. Nitzan, Physical Review Letters **94**, 034301 (2005).

[155] A. J. Leggett, S. Chakravarty, A. Dorsey, M. P. Fisher, A. Garg, and W. Zwerger, Reviews of Modern Physics **59**, 1 (1987).

[156] Y. Makhlin, G. Schön, and A. Shnirman, Reviews of Modern Physics **73**, 357 (2001).

[157] P. Cedraschi, V. V. Ponomarenko, and M. Büttiker, Physical Review Letters **84**, 346 (2000).

[158] P. Cedraschi and M. Büttiker, Annals of Physics **289**, 1 (2001).

[159] K. Le Hur and M.-R. Li, Physical Review B **72**, 073305 (2005).

[160] K. F. Mak, K. He, C. Lee, G. H. Lee, J. Hone, T. F. Heinz, and J. Shan, Nature materials **12**, 207 (2013).